Numerical investigation of the refractive properties of near-horizontal shore platforms and their effects on harmonic and stationary wave patterns

Raphael Krier-Mariani[1], Stephenson Wayne[1], Sarah Wakes[2], and Mark E. Dickson[3]

[1]University of Otago
[2]Department of Mathematics and Statistics, University of Otago
[3]University of Auckland

October 5, 2023

Abstract

Near-horizontal shore platforms display highly irregular plan shapes, but little is known about the way in which these irregularities influence the significant wave height (Hs) on the platforms and the frequency components of the nearshore wave field. We use a nonlinear Boussinesq wave model to conduct harmonic and bispectral mode decomposition analyses, studying the control of concave and convex platform edges over wind (WW: 0.125 - 0.33 Hz), swell (SW: 0.05 - 0.125 Hz) and infragravity (IG: 0.008 - 0.05 Hz) frequencies. For breaking and non-breaking waves, increasing the platform edge concavity intensified wave divergence and subsequent attenuation of SW and IG across the outer platforms, reducing by up to 25%. Increasing the platform edge convexity intensified focusing and amplification of SW and WW over the outer platforms, increasing by up to 18% and 55% for breaking and non-breaking waves. In the presence of breaking, IG amplification depended on the generation of wave divergence across the inner platform, a condition determined by a critical convex curvature threshold (K=1.8) balancing wave focusing from refraction and defocusing from breaking. We find that convex curvature can determine the relative dominance of WW, SW and IG across platforms. Alongshore, coherent wave interactions governed IG stationary patterns defined by a node near the platform centreline and two antinodes on either side of concave edges. A node was generated at the platform centreline, and two antinodes were observed on either side of the convex edges for K>1.8, with the opposite pattern observed for K<1.8.

Posted on 5 Oct 2023 — The copyright holder is the author/funder. All rights reserved. No reuse without permission. — https://doi.org/10.22541/essoar.169651343.36190544/v1 — This a preprint and has not been peer reviewed. Data may be preliminary.

Numerical investigation of the refractive properties of near-horizontal shore platforms and their effects on harmonic and stationary wave patterns

R. Krier-Mariani[1], W. Stephenson[1], S. Wakes[2], M. Dickson[3]

[1] School of Geography, University of Otago, New Zealand

[2] Department of Mathematics and Statistics, University of Otago, New Zealand

[3] School of Environment, University of Auckland, New Zealand

Corresponding author: Raphael, Krier-Mariani (raphael.m.krier@gmail.com; raphael.krier@postgrad.otago.ac.nz)

Key Points:

- Through refraction, concave and convex near-horizontal shore platforms can separate the frequency components of the wavefield.
- Refraction patterns controlled by platform edge convexity affect the dominance of wind, swell and infragravity waves across platforms.
- Coherent amplification from the intersection of refracted infragravity waves controls the nodal state of alongshore stationary waves.

Abstract

Near-horizontal shore platforms display highly irregular plan shapes, but little is known about the way in which these irregularities influence the significant wave height ($\widehat{H_s}$) on the platforms and the frequency components of the nearshore wavefield. We use a non-linear Boussinesq wave model to conduct harmonic and bispectral mode decomposition analyses, studying the control of concave and convex platform edges over wind (WW: 0.125 - 0.33 Hz), swell (SW: 0.05 - 0.125 Hz) and infragravity (IG: 0.008 - 0.05 Hz) frequencies. For breaking and non-breaking waves, increasing the platform edge concavity intensified wave divergence and subsequent attenuation of SW and IG across the outer platforms, reducing $\widehat{H_s}$ by up to 25%. Increasing the platform edge convexity intensified focusing and amplification of SW and WW over the outer platforms, increasing $\widehat{H_s}$ by up to 18% and 55% for breaking and non-breaking waves. In the presence of breaking, IG amplification depended on the generation of wave divergence across the inner platform, a condition determined by a critical convex curvature threshold ($|\mathcal{K}|$=1.8) balancing wave focusing from refraction and defocusing from breaking. We find that convex curvature can determine the relative dominance of WW, SW and IG across platforms. Alongshore, coherent wave interactions governed IG stationary patterns defined by a node near the platform centreline and two antinodes on either side of concave edges. A node was generated at the platform centreline, and two antinodes were observed on either side of the convex edges for $|\mathcal{K}|$>1.8, with the opposite pattern observed for $|\mathcal{K}|$<1.8.

Plain Language Summary

Near-horizontal shore platforms fronting coastal cliffs act as wave energy buffers, regulating wave-induced erosion in rock coast environments. Genuine research endeavours have permitted establishing the link between near-horizontal platform morphology and wave transformation across-shore. However, the effects of alongshore variations in near-horizontal platform morphology on the properties of nearshore wavefields remain sparsely documented. As ocean waves share akin refractive properties to light rays, it can be assumed that, similarly to optical lenses, shore platforms can separate waves according to their frequency depending on their geometry. Subsequently, the convergence and divergence of refracted wave trains of similar phases and frequencies could affect the properties of the nearshore wavefield. The present research investigates this phenomenon over concave and convex edge platforms and its impact on the nearshore wavefield characteristics. Our results show that wave refraction over near-horizontal platforms with concave and convex edges affects the relative dominance of short, medium and long-period waves across shore and results in alongshore stationary wave patterns near the shoreline with nodal states varying in relation to platform edge geometry. Such patterns likely result in alongshore variations in wave erosion and the generation of wave-generated currents shaping rock coasts in the planform.

1 Introduction

Near-horizontal shore platforms, defined by a low gradient ($tan\beta < 0.0175$) and a steep seaward edge, are prevailing coastal landforms in rock coast environments (Sunamura, 1992; Trenhaile, 1999). These landforms have an essential role in wave transformation processes, regulating wave erosive forces at the shoreline (Stephenson and Kirk, 2000; Matsumoto et al., 2016a,b). Thus, an accurate description of the geomorphic control exerted by shore platforms on nearshore wave transformation patterns is necessary for improving rock coast geomorphological models.

Studies have investigated the control of near-horizontal shore platform morphology on the cross-shore evolution of the wavefield (e.g. Beetham and Kench, 2011; Marshall and Stephenson, 2011; Ogawa et al., 2016). Wave breaking induced by the sharp depth transition at the seaward edge of a platform results in the dissipation of incident swell waves (SW: 0.05 Hz < f < 0.125 Hz) and the generation of low-frequency infragravity waves (IG: f < 0.05 Hz) over the platform (Poate et al., 2020). Across the platform surface, IG gradually amplify due to shoaling and energy is transferred from high to lower frequencies, becoming the dominant frequency component over the inner platform (Beetham and Kench, 2011; Marshall and Stephenson, 2011; Ogawa et al., 2011). Wind waves (WW: 0.125 < f < 0.33 Hz) can propagate onto platforms from offshore and, in some cases, be locally generated over the outer platform to become the dominant frequency component in this area (Marshall and Stephenson, 2011; Ogawa et al., 2011). These observations were summarised in the conceptual model of Ogawa et al. (2011), indicating that it is common for the outer platform, platform centre, and inner platform to be dominated by WW, SW and IG, respectively. Ogawa et al. (2011) suggested that these zones shift across-shore with tidal elevation and showed that the relative submergence of shore platforms (depth at the seaward edge/incident wave height) is a critical factor controlling the relative dominance of SW and IG. Collectively, understanding the behaviour of each frequency band of the wavefield helps to depict the variation of significant wave height (H_s) across platforms affecting erosion of the platform and cliff (Trenhaile, 2000). However, the impact of shore platform morphology on two-dimensional wave transformation processes and effect on the frequency bands composing the wavefield have been overlooked.

Few field studies have considered the impact of the planform morphology of near-horizontal platforms on two-dimensional wave transformation patterns (Krier-Mariani et al. 2022, 2023). Krier-Mariani et al. (2023) showed that directional patterns controlled by irregularities in planform morphology generated localised areas of wave ray convergence and divergence as well as alongshore variations in standing IG patterns, influencing the wave energy distribution over the platform surfaces. Based on these observations, Krier-Mariani et al. (2023) introduced a conceptual model in which concave and convex platform edge geometries would control wave ray convergence and divergence patterns over the platform surface, subsequently affecting the IG energy levels and SW decay rates. However, the influence of platform edge geometry on two-dimensional wave patterns could not be clearly isolated from field observations.

In the absence of detailed field studies on the effects of platform edge geometry on wave transformation characteristics, the literature on morphologically analogous submerged flat structures is useful. Depending on their geometry, submerged flats can separate the frequency components of the wavefield, refracting and reorganising the wave crests of incident waves according to their frequency (Jarry et al., 2011; Griffiths and Porter, 2012; Li et al., 2020). This phenomenon can result in complex refraction patterns specific to each frequency component of the wavefield, leading to the generation of caustic rays (clusters of caustic points generated by wave ray intersection) over submerged surfaces (e.g. Mandlier and Kench, 2012). Patterns of wave ray convergence and divergence induced by refraction over submerged flat structures significantly impact the wavefield characteristics. Wave ray convergence results in a localised enhancement of wave height (e.g. Ito and Tanimoto, 1972; Berkhoff et al., 1982), skewness and kurtosis (Janssen and Herbers, 2009; Jarry et al., 2011; Lawrence et al., 2022) while wave ray divergence has the opposite effects.

Although relatively few studies have considered the impact of submerged flat geometries on the cross-shore evolution of harmonic and subharmonic components of the wavefield, harmonic components amplification has been observed in areas of wave convergence (e.g. Lynett and Liu, 2004; Gouin et al., 2017). According to Li et al. (2020), this phenomenon could be attributed to the non-linear effects of convergence on wave height amplification. As the geometry of submerged flats influences the cross-shore pattern of wave convergence (intensity and location) of each harmonic, it likely also influences the cross-shore patterns of wave harmonics amplification, intrinsically affecting the dominance of different wave frequencies across platforms. This hypothesis as yet to be verified.

It has proven difficult to establish causality between patterns of wave ray intersection, increased nonlinearity and alongshore wave height amplification for random wavefields, notably due to the limitation of wave ray tracking techniques to evaluate complex wave ray crossing patterns in dense constellations of caustics (Ito and Tanimoto, 1972). Another way of approaching this problem involves considering the impact of coherent wave interaction patterns on the amplification of dominant frequency components of the wavefield. Coherent wave interaction refers to the non-linear process occurring at the intersection of waves with similar frequency, waveform and phase. It has been identified as a fundamental non-linear wave amplification process in optics (e.g. Young, 1802), quantum mechanics (e.g., Weiland and Wihelmsson, 1977; Falk, 1979; Inouye et al., 1999; Kozuma et al., 1999) and geoscience (e.g. Harid et al., 2014). There have been few investigations of this process in coastal wave studies, but Dalrymple (1975) demonstrated that this process could result in the formation of alongshore stationary wave patterns in random wavefields and the subsequent formation of nearshore currents. More recently, Tamura et al. (2020) showed that, similar to light refraction through a prism, ocean wave refraction over a submarine canyon could separate waves of a random wavefield according to their frequency and phase, favouring coherent wave interactions. Based on this theoretical grounding, it is hypothesised that by controlling the refraction patterns of individual frequency components of the wavefield, submerged flat (e.g. shore platforms) geometry affects coherent wave amplification over submerged flat surfaces, leading to the generation of alongshore stationary wave patterns for SW and IG.

The impact of shore platform geometry on the behaviour of wave harmonics and stationary wave patterns remains to be evaluated in detail on near-horizontal platform surfaces. However, such a task was proven to be difficult during field observations due to the variable nature of nearshore wavefields and the morphological complexity of shore platforms (e.g. Krier-Mariani et al. 2022, 2023). Therefore, this study adopts a numerical modelling approach to address the question: How do mesoscale variations in platform edge geometry affect the behaviour of wave harmonics and the subsequent wave height distribution across and along platform surfaces?

2 Method

2.1 Model set up

The phase-resolving Boussinesq wave model FUNWAVE_TVD V3.6 (Shi et al., 2012) was used to investigate two-dimensional wave transformation over shore platforms. This model treats wave transformation in the time domain and provides a robust representation of non-linear processes, refraction and diffraction while retaining information on the wave phase (Sheremet et al., 2011; Buckley et al., 2015, Buckley et al., 2018; Thomas and Dwarakish, 2015).

2.1.1 Domain

Idealised three-dimensional near-horizontal platform morphologies were incorporated into a 1274 m (x-axis) to 300 m (y-axis) domain (Fig. 1a). A 0.35 m deep, 250 m wide shallow planar surface was included at the landward extremity to absorb wave energy and minimise resonance. The platforms were defined by a constant gradient of 0.35 degrees, a width of 300 m (at the centreline, y = 150 m) and a 3m high seaward cliff of 45 degrees. The nearshore bathymetry profile was composed of a 480 m subtidal ramp (at the centreline) with a gradient of 0.35 degrees followed by an 8 m deep and 635 m wide flat.

Planform geometry was represented using three generic edge geometries defined as straight, concave and convex. The degree of curvature of the concave ($\mathcal{K} < 0$) and convex ($\mathcal{K} > 0$) edge geometries was derived from the parametric ellipse equation. The semi-major axis (a, along the x-axis) was kept constant (120 m) to avoid modifying the cross-shore profile along the centreline, and various degrees of edge curvature were obtained from 2 m increments along the semi-minor axis (b, along the y-axis) between 50 to 100 m, resulting in 26 cases with edge curvatures ($|\mathcal{K}| = |a/b|$) ranging from 1.2 to 2.4 (Fig. 1b-f). The bathymetry was smooth to reduce noise generated by sharp edges and interpolated to a 2 m grid adopted to ensure model stability following a series of sensitivity analyses, providing a realistic representation of model resolution used in previous research in nearshore areas (e.g. Su et al., 2021).

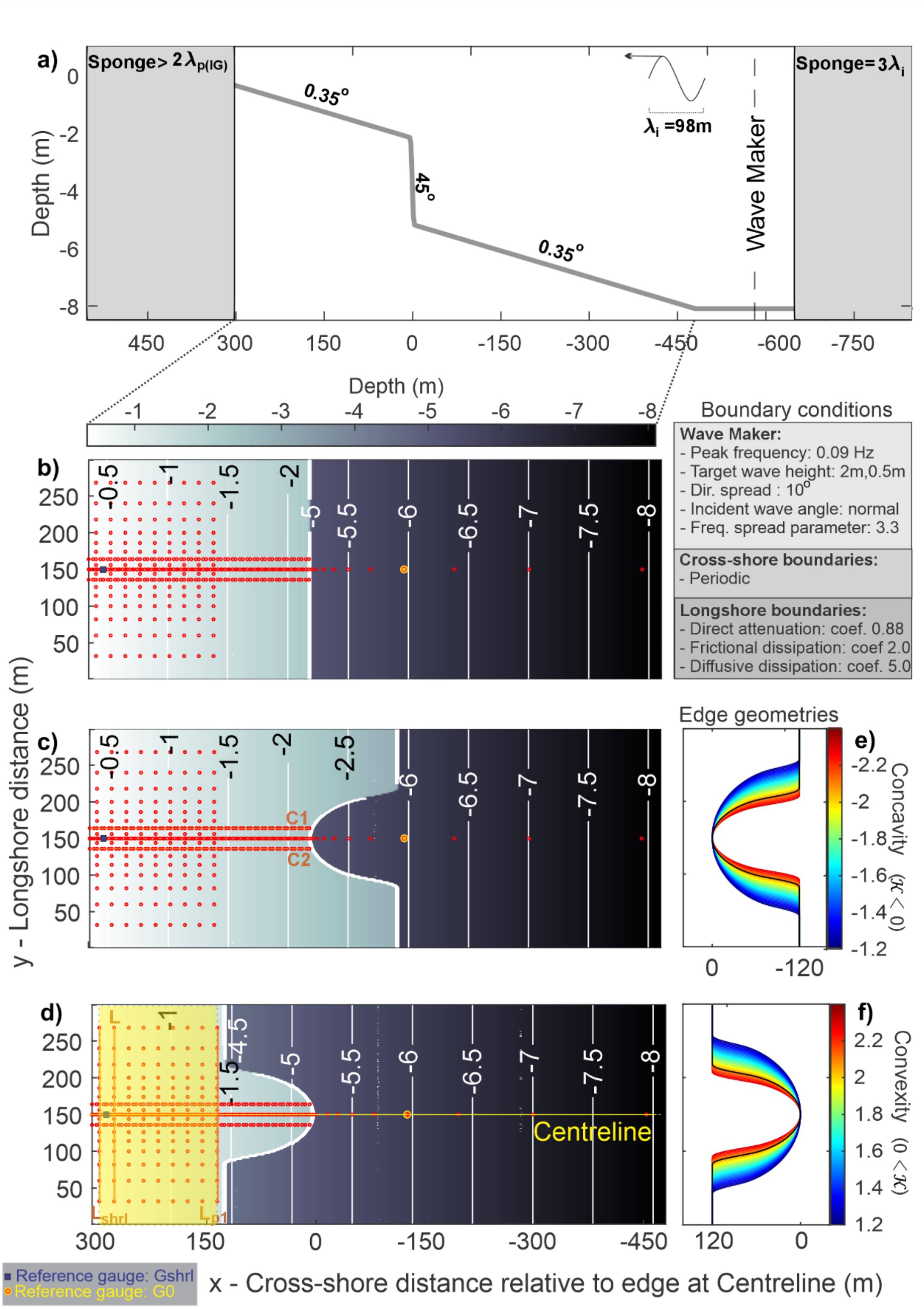

Figure 1: Boussinesq wave model configuration showing the bathymetry profile along the centreline (y = 150m) (a), the model domain for the straight, concave and convex platforms (b-d), and the range of platform edge curvatures considered (e,f). Specifications of the boundary conditions are annotated in the figure. The red dots mark the location of the virtual gauges used for analysis. The yellow shaded area (between L_p and L_{srl}) represents the inner platform section considered for alongshore analysis.

2.1.2 Wave conditions

The model was forced by irregular waves with a directional spread of 10 degrees. An internal wavemaker (Wei et al., 1999) was located on the deep flat at the bottom of the subtidal ramp, five wavelengths (λ_i) away from the platform edge to avoid distortion of the initial wave crests. Irregular waves were generated using a JONSWAP wave spectra (Hasselmann et al., 1973) with a fixed peak enhancement factor of 3.3, a peak frequency (f_p) of 0.09 Hz and direction of 0° (shore-normal) to simplify the visualisation of the refraction effects induced by different planform edge geometries.

Two sets of simulations were generated to investigate the transformation of: (1) waves propagating across the platform surface without breaking (H_s= 0.5 m), as such waves can release large amounts of erosive energy when they break against cliffs (Thompson et al., 2019; Thompson et al., 2022); and (2) wave breaking at the seaward edge (H_s= 2 m) decaying across the platform, which are typically used to define variation of wave erosive force across platforms in geomorphological models (e.g. Trenhaile, 2000; Matsumoto et al., 2016a,b). These two sets of simulations combined with the range of platform concave and convex curvatures resulted in 106 simulations (including straight edge reference cases). The default breaking index of FUNWAVE-TVD (γ_b=0.80) was used to represent wave breaking, providing a close representation of the breaking conditions for steep submerged slopes (Blenkinsopp and Chaplin, 2008). The effects of bottom friction were not considered (i.e. the frictional dissipation coefficient was set to C_d= 0.002, representing a smooth surface).

2.1.3 Boundary conditions

The domain boundary conditions were defined to minimise reflection. Periodic boundaries (Chen et al., 2003) were applied to the northern and southern extremities of the domain, allowing waves to propagate out of the domain. Following Shi et al. (2016), sponge layers employing a direct damping coefficient as well as dissipation by friction and diffusion were used to reduce noise and dampen wave energy at the eastern and western sides of the domain (Fig. 1a). The width of the sponge layer at the shallow western side of the domain was chosen to correspond to twice the peak wavelength of the IG at this location (estimated during trial runs using the virtual gauge G_{shrl} at the shoreline, Fig. 1), to avoid reflection and the subsequent generation of standing IG waves.

2.1.4 Model Validation

Due to the lack of two-dimensional field measurements in similar near-horizontal shore platform settings, no direct validation of our model simulations was carried out. However, a number of studies validated FUNWAVE-TVD against field observations over coral reefs, proving the model's ability to represent wave transformation over smooth submerged flats with sharp seaward edges (e.g. Mendonca et al., 2008; Su et al., 2015; Zhang et al., 2019). As the present study explores wave processes such as refraction and non-linear energy transfer fairly well represented by the model (Griffiths and Porter, 2012; Su et al., 2015) and does not investigate subsequent processes such as wave-driven circulation and sediment transport, it is deemed unnecessary to validate the model with experimental data at this stage (similar inference were made in da Silva et al., 2023).

2.2 Measurements and analysis

To determine the impact of planform geometries on wave transformation across the platforms, the spectral evolutions of waves propagating across concave and convex platforms (affected by two-dimensional transformation processes) were compared to the spectral evolution of waves propagating across the straight-edge platform (only affected by on-dimensional transformation processes). This approach permitted the identification of spectral anomalies representing the energy variations for specific harmonics induced by refraction. Positive and negative anomalies indicate harmonic amplifications and attenuation, respectively. Combined, the harmonic anomalies result in anomalies of significant wave height across platforms ($\Delta\widehat{H_s}$). Following Baldock et al. (2020), the cross-shore patterns of $\Delta\widehat{H_s}$ were then compared to the directional patterns along the platform centrelines to identify the effects of refraction patterns controlled by platform edge geometry on significant wave height distribution across platforms.

In the alongshore, the effects of coherent wave interaction induced by refraction over concave and concave platforms on the generation of stationary wave patterns were considered. For this purpose, the bispectrum (Hasselmann et al., 1963) provides a convenient representation of the wavefield as it holds information on the wave phase, frequency and power necessary to detect phase coupling. The bispectrum, defined from the third moment of the free surface elevation time series, also represents a measure of skewness, which increases in areas of wave ray intersection (Janssen and Herbers, 2009; Jarry et al., 2011; Lawrence et al., 2022). Following Kim and Powers (1979), who investigated the impact of coherent interactions of random electromagnetic waves on plasma density fluctuation using bispectral properties, the frequency, phase and power information yielded by the bispectrum were used to identify patterns of coherent wave interactions over the inner platforms. A modal decomposition method based on bispectral properties (Appendix 2), the Bispectral Mode Decomposition or BMD (Schmidt, 2020), was employed to identify the modal state of coherent structures for self-interacting harmonic components within the SW and IG frequency bands. The areas of coherent wave interactions were then compared to the wave height distribution of SW and IG over platforms of various geometries to identify patterns of coherent wave amplification.

2.2.1 Wave measurements

Wave records were obtained from virtual gauges recording surface elevation (η) as well as u and v velocity components at 2 Hz (Fig. 1b-d). In the cross-shore direction, the gauge spacing along the centreline increased seaward from the platform edge (increment based on geometric series starting with a spacing of 4 m with an increment factor of 1.5). On the platforms, the gauge spacing was irregular but not exceeding 6 m along the centreline, transects C_1 and C_2. The distance between the gauges composing the alongshore transects (between L_0 and L_{shrl}) increased on either side of the centreline from 6 to 30 m (with an increment factor of 1.25). Statistical analyses of the wavefield properties were based on an observation window of 2048 seconds, starting 230 seconds after the start of the simulations, marking the time at which SW reached the landward extremity of the domain and IG were generated.

2.2.2 Definition of wave height

The significant wave height (H_s) was defined from the spectra moment (e.g. Thornton and Guza, 1983):

$$H_s = 4\sqrt{\int_{fmin}^{fmax} S(f).df} \tag{1}$$

The wave spectra estimates $S(f)$ were generated using the Welch (1967) method with segment lengths of 512 samples, 50% overlap and a Hanning window resulting in 20 Degrees of Freedom (Priestley, 1981). To provide a more detailed representation of the wavefield, the gravity and infragravity waves were further divided into two frequency bands, encapsulating the dominant harmonics observed within the WW, SW, and IG (high and low) frequency ranges across the domain (Table 1). The wave height associated with each of these frequency bands was determined using:

$$H_{f_{np}} = 4\sqrt{\int_{flow}^{fhigh} S(f).df} \tag{2}$$

where n denotes the rank of the harmonic, f_{low} and f_{high} represents the lower and higher frequencies of the power spectral density peak associated with this harmonic, Table 1. The reference incident wave height (H_0) was defined from measurements taken at the gauge G_0 located at the top of the subtidal ramp (Fig. 1) and was used to normalise the wave height on the platform surface ($\widehat{H_s}(x) = H_s(x)/H_0$, $\widehat{H_{fnp}}(s) = H_{fnps}(x)/H_0$). For simplicity, normalised wave heights are hereafter referred to as wave heights.

Table 1 Frequency band analysis parameters

Conventional Frequency class	Frequency subclass	Corresponding Harmonic	Frequency (f_{np})	Frequency range ($f_{low} - f_{high}$)
Gravity waves	Wind waves (WW)	Second harmonic	f_{2p}	0.15 – 0.20 Hz
	Swell waves (SW)	Principal harmonic	f_p	0.06 – 0.12 Hz
Infragravity waves	Infragravity High (IG_H)	Second subharmonic	$f_{1/2p}$	0.04 – 0.05 Hz
	Infragravity Low* (IG_L)	Fifth subharmonic	$f_{1/5p}$	0.008 – 0.03 Hz

*Note that the typical cutoff frequency for the lower portion of the IG frequency band is 0.005 Hz (e.g. Pequignet et al., 2014; Gawehn et al., 2016). However, the chosen cutoff frequency of 0.008 Hz is more appropriate to describe the low IG in the simulated wavefield as it corresponds to a trough in the power spectra estimate across the entire domain, which provides a better physical representation of the low IG.

2.2.3 Definition of peak direction

The angle α between the peak direction of waves propagating on either side of the centreline (along the cross-shore transects C1 and C2, Fig. 1) was used to investigate the evolution of wave convergence and divergence along the platform centrelines. The peak direction of waves over the platform was estimated from the directional wave spectra $S(f,\theta) = S(f)G(\theta|f)$ calculated from the free surface elevation (η) and velocity components (u and v) time series by applying the Extension of the Maximum Entropy Principle (EMEP) method (Hashimoto et al., 1994). To this effect, segments of 512 samples were used to estimate the frequency spectra ($S(f)$) and 200 iterations to define the approximation of the spreading function ($G(\theta|f)$) resulting in 76 frequency bins and directional bins of 5°.

2.2.4 Identification of coherent wave interaction patterns

The BMD was applied to the free surface elevation time series recorded by the two-dimensional virtual gauge array between L_p and L_{shrl}, marking the boundaries of the spatial domain ξ (Fig. 1). The welch periodograms employed in the BMD were computed using segments of 512 samples, 50% overlap and a Hanning window resulting in 20 Degrees of Freedom. Patterns of coherent wave interactions were identified from coherent self-interaction maps ($\psi_{k,k}$) which are defined by the product of cross-frequency fields $\phi_{k\circ k}$ and the bispectral modes ϕ_{k+k} obtained from the BMD:

$$\psi_{k,k}(\xi, f_k, f_k) = |\phi_{k\circ k} \circ \phi_{k+k}| \tag{3}$$

where the frequency k considered were f_p and $f_{1/5p}$, representing the dominant harmonics in the SW and IG frequency bands. The cross-frequency fields $\phi_{k\circ k}$ are maps of phase alignment for these frequencies, while bispectral modes ϕ_{k+k} represent the amplitude of oscillations of the sea surface at frequency $2k$. Conventionally, the largest values of the normalised coherent self-interaction maps $\widehat{\psi_{k,k}}$ indicate areas where phase coupling has the strongest effect on wave amplitude for the sum frequency $2k$. The interaction maps for straight wave crests with parallel wave rays are expected to be homogeneous alongshore. In contrast, for cases where wave crests are bent and wave rays intersect, interaction maps will be non-homogenous alongshore and display maxima in areas of wave ray intersection. In the presence of coherent wave amplification, maxima in coherent self-interaction maps correspond to areas of wave height amplification at frequency k.

3 Results

3.1 Impact of planform geometry on across-shore wave transformation

3.1.1 Non-breaking waves (H_0 = 0.5 m)

The spatial evolution of the spectral properties of non-breaking waves propagating across the domain was examined for the three types of platform geometries (Fig. 2), for which the power spectra density was concentrated around four distinctive frequency components (Fig. 2a): the second and the principal harmonics (f_{2p} and f_p) within the WW and SW frequency bands; and the second and fifth subharmonics ($f_{1/2p}$ and $f_{1/5p}$) within the IG_H and IG_L frequency bands.

The spectral anomalies observed over the concave platforms indicated an attenuation of the principal harmonic (Fig. 2b-e). This phenomenon intensified with increasing degrees of curvature (with minimum spectral anomalies at peak frequency reducing from -0.09 m^2 Hz^{-1}

at $|\mathcal{K}|$= 1.2 to -0.41m^2 Hz^{-1} at $|\mathcal{K}|$= 2.4). In contrast, an amplification of the second and principal harmonics was observed across convex platforms (Fig. 2g-j), intensifying with increasing edge curvature (with maximum spectral anomalies at peak frequency increasing from 0.52 m^2 Hz^{-1} at $\mathcal{K}$= 1.2 to 1.37 m^2 Hz^{-1} at $\mathcal{K}$= 2.4).

The variation of spectral characteristics of each harmonic over the concave and convex platforms can be expressed in terms of mean wave height anomalies ($\overline{\Delta H_{fnp}}$). The most significant impacts of platform curvature on mean wave height anomalies were observed within the WW and SW frequency bands. The mean wave height anomalies associated with the second and the principal harmonics displayed a very strong linear dependency ($R^2 > 0.9$) to the degree of platform edge curvature (Fig. 2f,k). The increase of curvature form $|\mathcal{K}|$= 1.2 to 2.4 promoted the attenuation of harmonics within the WW and SW frequency bands across concave platforms and the amplification of these waves across convex platforms. The attenuation of the second and principal harmonics across concave platforms of high curvature $|\mathcal{K}|$= 2.4 corresponded to 9% and 15% of H_0. Across convex platforms of high curvature, $|\mathcal{K}|$= 2.4, the amplification of the second and principal harmonics reached up to 11% and 29% of H_0. The mean wave height anomalies for the subharmonic in the IG_H and IG_L frequency bands were negligible for nonbreaking waves.

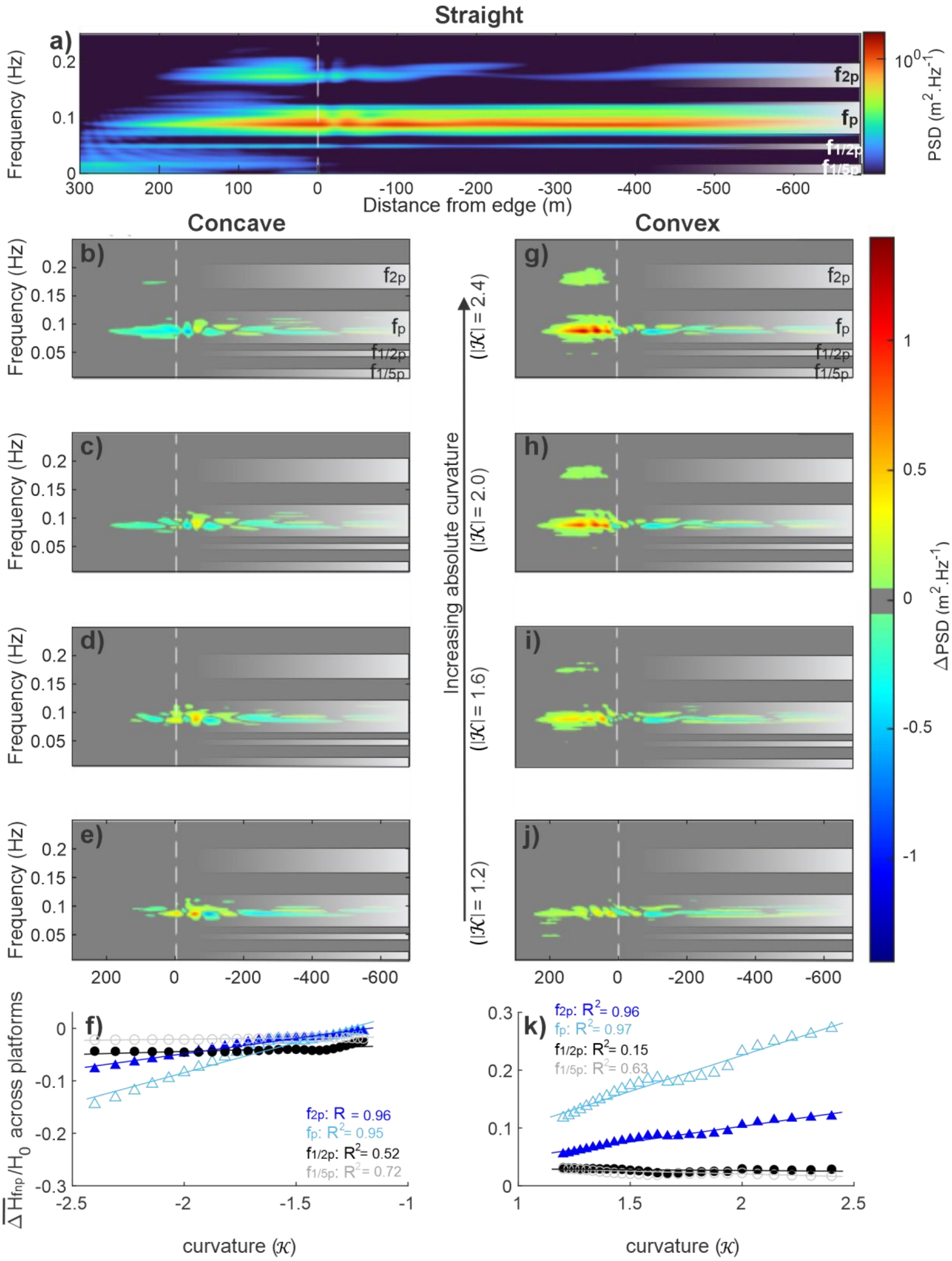

Figure 2: Impact of platform edge curvature on the harmonic components of the wavefield for non-breaking waves showing: the spectral anomalies in relation to the straight edge platform (a) for concave platform geometries (b-e) and convex platform geometries (g-j); and the impact of curvature on the mean wave height of each harmonic across the concave (f) and convex (k) platforms.

$\Delta\widehat{H_s}$ across the platform can be assumed to be impacted by refraction patterns controlled by platform geometry. To explore this process, directional patterns and $\Delta\widehat{H_s}$ across the centrelines of each platform were compared for various edge curvatures. The cross-shore patterns of $\Delta\widehat{H_s}$ presented in Fig. 3a,b were modulated by the platform edge curvature, with magnitude increasing with curvature for both types of platform geometries. As a result, for high degrees of curvature ($|\mathcal{K}|$ = 2.4), the negative anomalies across the concave platforms indicated a maximum of 25% attenuation in significant wave height (Fig. 3a), while the positive anomalies across the convex platforms (Fig. 3b) indicated a 55% amplification of significant wave height. The location of the largest $\Delta\widehat{H_s}$ shifted across platforms in relation to curvature. For concave platforms, the largest negative $\Delta\widehat{H_s}$ over the outer platform shifted landward with decreasing curvature from $|\mathcal{K}|$ = 2.4 to 1.9. Similarly, the largest positive $\Delta\widehat{H_s}$ across the convex platforms shifted landward, reaching the inner platform for $|\mathcal{K}|$ < 1.6. For low degrees of concave curvatures ($|\mathcal{K}|$ < 1.9), corresponding to curvatures for which amplification of wave energy seaward of the platform edge was observed (Fig. 2b-e), wave transformation patterns across the platform centreline were affected by the preconditioning of incident waves occurring off the platform edge. Therefore, the description of the following results focuses on concave edge curvatures, $|\mathcal{K}| >$1.9.

Similarly to the cross-shore evolution of $\Delta\widehat{H_s}$, the peak magnitude of wave ray divergence observed across concave platforms and convergence across the convex platforms decreased and shifted landward from the mid-platform ($x \approx 150\ m$) to the outer platform with decreasing curvature (Fig. 3c,d). A Spearman rank correlation (Fig. 3e,f) revealed that the dependency of cross-shore $\Delta\widehat{H_s}$ on the directional patterns observed over the concave platforms was only relevant (moderate to strong, ρ_S > 0.4) for platform edge curvatures exceeding 1.9. In contrast, a strong relationship (ρ_S > 0.6) as observed between wave height anomaly and directional patterns over convex platforms for the majority of platform edge curvatures, indicating that $\Delta\widehat{H_s}$ across the convex platforms were predominantly controlled by the wave convergence and divergence across the centreline.

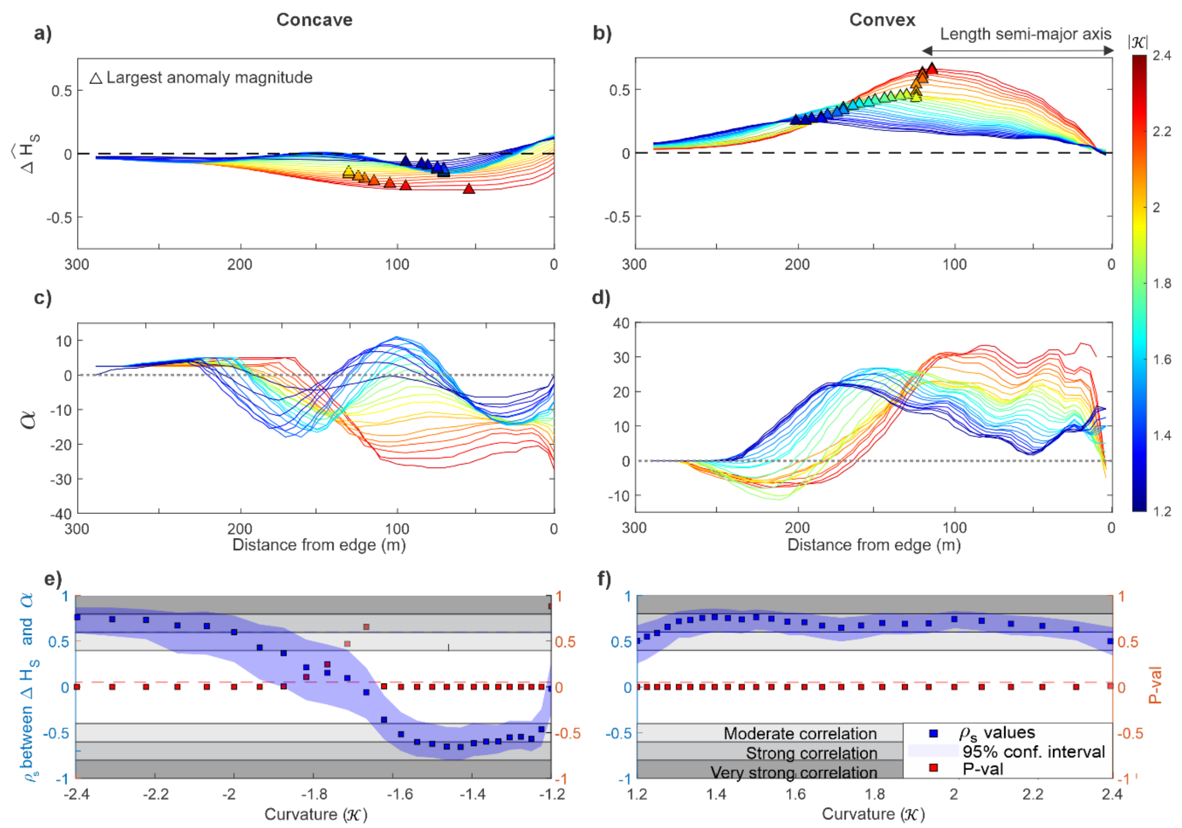

Figure 3: Relationship between directional patterns and significant wave height anomalies of non-breaking waves across concave (left) and convex platforms (right) at the centreline (y =150 m) for different degrees of curvature showing: the significant wave height anomalies (a,b) and the cross-shore directional patterns (c,d). The impact of directional pattern on wave anomaly pattern was assessed using a spearman correlation between the two parameters (e,f).

3.1.2 Broken waves (H_0 = 2.0 m)

The spectral evolution of broken waves across concave platforms displayed a complex pattern of spectral anomalies (Fig. 4b-e), with a clear amplification of the principal harmonic corresponding to SW over the outer platform for degrees of curvature below 1.9 (at f_p, positive anomalies reached 1.5 m^2 Hz^{-1} at $\mathcal{K}$= 2.0 and 2.4, 0 to 150 m from the edge) and a clear attenuation of this harmonic for degrees of curvature exceeding 1.9 (at f_p, negative spectral anomaly reached -1.2 m^2 Hz^{-1} at $\mathcal{K}$= 1.2 and 1.6, 0 to 150 m from the edge). These differences were related to the amplification of the principal harmonic for edge curvatures below 1.9, displaying anomalies reaching up to ~12 m^2 Hz^{-1} in the vicinity of the concave edge sections (0 to -120 m from the edge) before reaching the platform surface (Fig. 4d,e). Over convex platforms, the principal harmonic presented the largest amplification (Fig. 4g-j), which intensified over the outer platform with increasing curvature (positive anomaly at f_p reached 2.1 m^2 Hz^{-1} at $\mathcal{K}$= 1.2 and 4.1 m^2 Hz^{-1} at $\mathcal{K}$= 2.4, 0 to 150 m from edge). In contrast, the amplification of subharmonics within the IG$_H$ and IG$_L$ frequency bands toward the shoreline observed along the platform centreline was stronger for low convex edge curvatures than for high convex edge curvatures (positive anomaly at $f_{1/5p}$ reached 0.7 m^2 Hz^{-1} at $\mathcal{K}$= 1.2 and 0.5 m^2 Hz^{-1} at $\mathcal{K}$= 2.4, 150 to 300 m from edge).

Relationships between edge curvature and mean wave height anomalies across both platform types were observed (Fig. 4f,k). For anomalies in the WW and SW frequencies, the mean wave height anomalies of the second and the principal harmonics presented a strong linear dependence on the degree of edge curvature of concave and convex edges (R^2 > 0.90). In the IG$_H$ frequency band, mean wave height anomalies associated with the second subharmonic were linearly dependent on the curvature across concave platforms (R^2 = 0.67). The mean wave height anomalies associated with the fifth subharmonic in the IG$_L$ frequency band decreased linearly (R^2 = 0.94) with curvature over the convex platforms.

Variations in edge curvature affected the relative importance of WW, SW, IG$_H$ and IG$_L$ anomalies across the platforms. For concave platforms, the increase of concave edge curvature promoted attenuation of all frequency bands, but particularly for WW and SW. For the harmonic components within the WW and SW frequency bands, the mean wave height attenuation across concave platforms was negligible for low curvature ($\overline{\Delta H_{f_{2p}}}$ and $\overline{\Delta H_{f_p}}$ and representing less than 1% of H_0 at $|\mathcal{K}|$=1.2) but intensified for high degrees of curvature ($\overline{\Delta H_{f_{2p}}}$ and $\overline{\Delta H_{f_p}}$ representing less than 3% and 6% of H_0 at $|\mathcal{K}|$=2.4). Across the convex platforms of low curvature (1.2 < $|\mathcal{K}|$ < 1.75), the largest amplification of mean wave height was observed for the principal harmonic ($\overline{\Delta H_{f_p}}$ representing 4% to 7% of H_0), followed by the fifth subharmonic ($\overline{\Delta H_{f1/5_p}}$ representing 3% to 3.5% of H_0). The amplification of the fifth subharmonic became less important with increasing curvature, while the mean wave height of the second harmonic was amplified. For convex curvatures exceeding 1.75, the principal harmonic displayed the largest amplification ($\overline{\Delta H_{f_p}}$ representing 7% to 10% of H_0), followed by the second harmonic ($\overline{\Delta H_{f_{2p}}}$ representing 3% to 4% of H_0). Thus, the reduction of convex edge curvature promoted the amplification of IG$_L$, while the increase of convex edge curvature promoted the amplification of WW and SW.

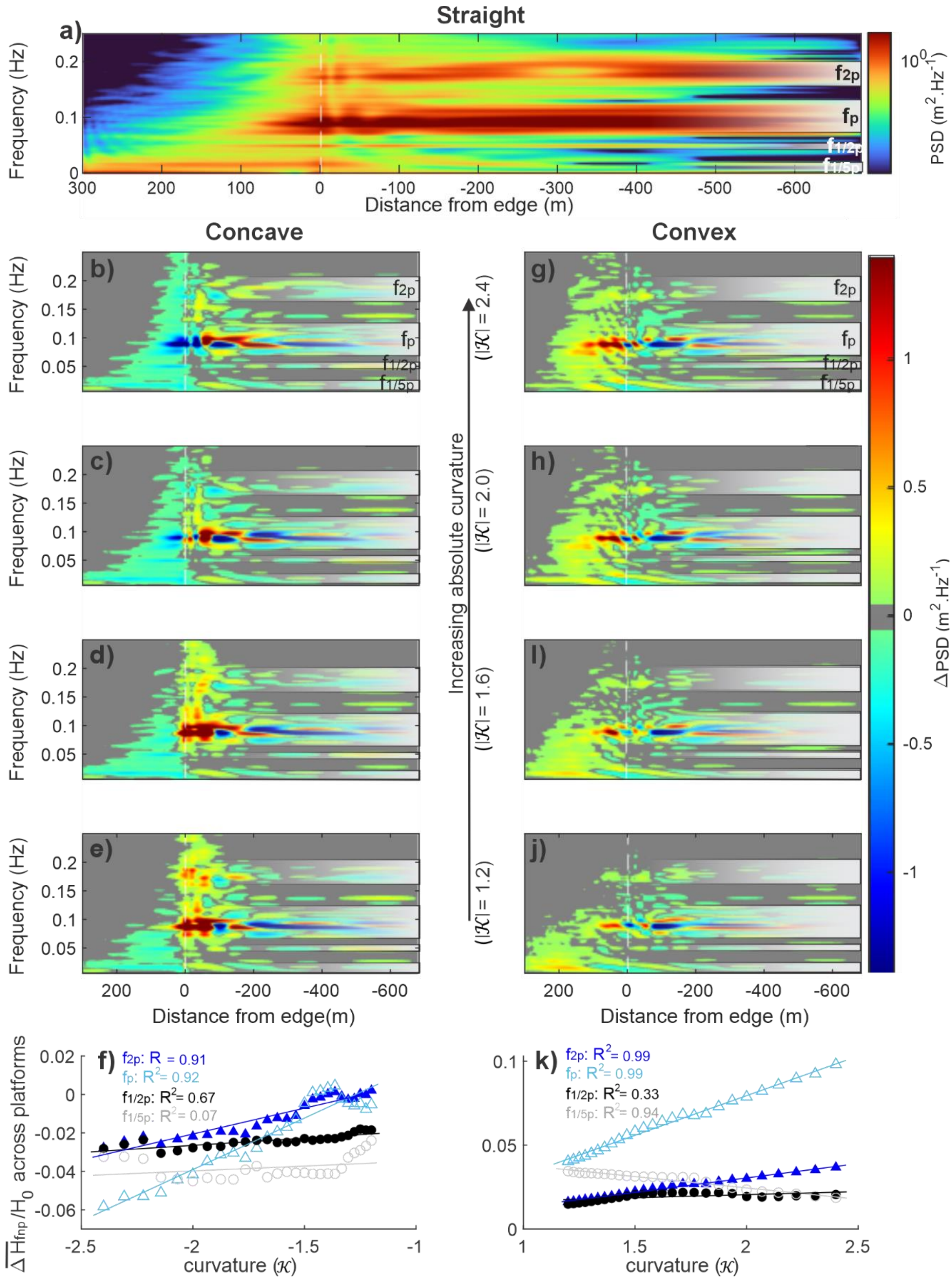

Figure 4: Impact of platform edge curvature on the harmonic components of the wavefield for broken waves showing: the spectral anomalies in relation to the straight edge platform (a) for concave platform geometries (b-e) and convex platform geometries (g-j); and the impact of curvature on the mean wave height of each harmonic across the concave (f) and convex (k) platforms.

The relationship between $\Delta\widehat{H_s}$ (Fig. 5a,b) and directional patterns (Fig. 5c,d) observed across the concave and convex platform centrelines was more complex for broken than non-breaking waves. The main difference with the non-breaking waves resided in the seaward shift of the maximum divergence (Fig. 5c) and convergence (Fig.5d) locations over the outer concave and convex platforms, respectively. This shift was particularly pronounced for convex shore platforms with low degrees of curvature ($|\mathcal{K}| < 1.8$), for which the peaks of convergence observed mid-platform ($x \approx 175$ m, Fig. 3d) were attenuated.

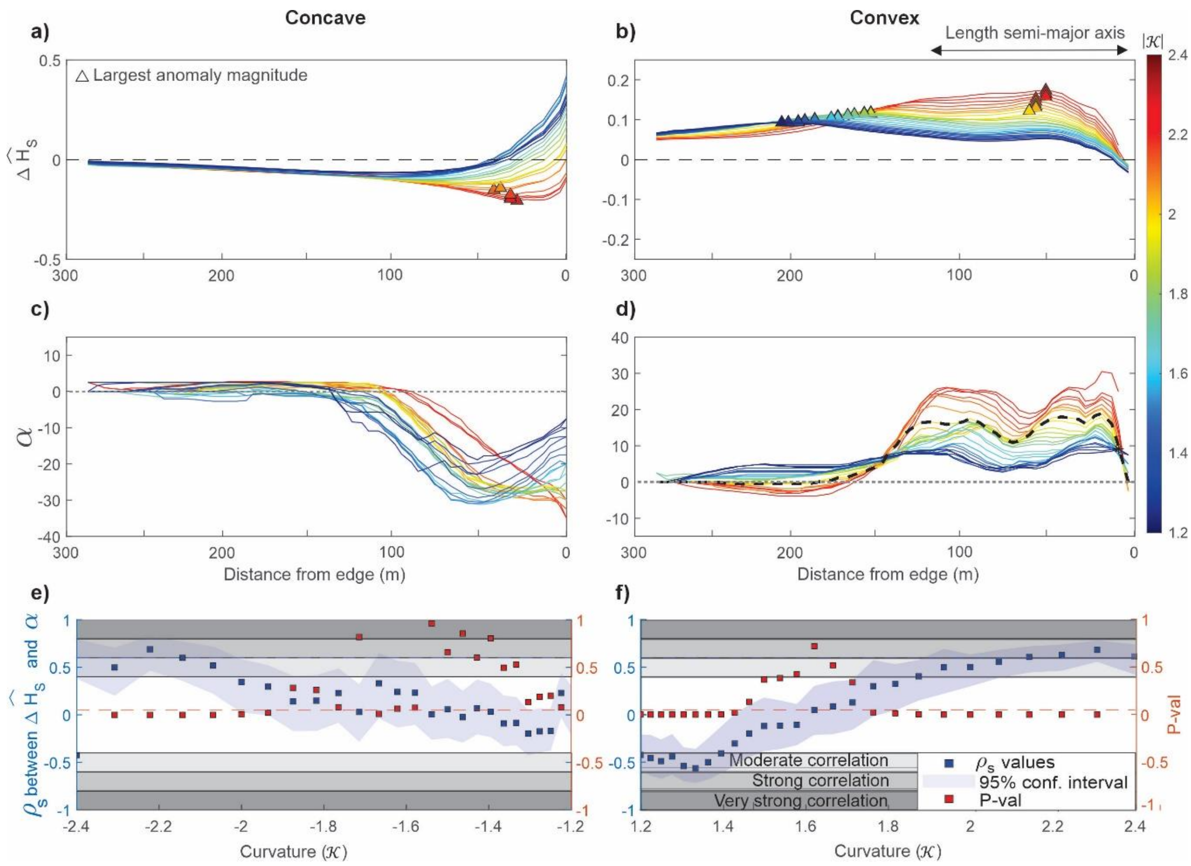

Figure 5: Relationship between directional patterns and significant wave height anomalies of broken waves across concave (left) and convex platforms (right) at the centreline (y = 150 m) showing: the significant wave height anomalies (a,b), the cross-shore directional patterns (c,d) and spearman correlation between these two parameters (e,f).

For concave platforms, the seaward shift of maximum divergence zones coincided with a seaward shift of the location of the largest negative anomalies (representing a 25% attenuation in $\widehat{H_s}$, Fig. 5a). As a result, the relationship between $\Delta\widehat{H_s}$ and directional patterns of broken waves remained moderate to strong ($0.4 < \rho_s < 0.6$) for concave edge curvatures exceeding 1.9 (Fig. 5e), indicating that for large degrees of edge curvature, the $\Delta\widehat{H_s}$ observed across the concave platform depended on the directional patterns along the centreline. For convex platforms, the seaward shift of the maximum convergence locations (Fig. 5d) coincided with a seaward shift of the largest positive anomalies for curvatures over 1.8 (representing an 18% amplification in $\widehat{H_s}$, Fig. 5b). However, for curvatures lower than 1.8, the maximum anomalies shifted landward. Thus, the correlations between $\Delta\widehat{H_s}$ and directional patterns across the centreline were moderate to strong ($0.4 < \rho_s < 0.6$) for convex edge curvatures exceeding 1.8, and weak ($\rho_s < 0.4$) for curvatures dropping below 1.8 (Fig. 5f). This phenomenon can be explained by analysing the relative influence of each harmonic component on $\Delta\widehat{H_s}$ observed across the platforms (Fig. 6).

For convex curvatures exceeding 1.8, the decrease of wave convergence over the outer platform and wave ray divergence over the inner platforms (Fig. 5c) coincided with a reduction of wave height anomalies for all harmonic components over the inner platform (Fig. 6). This reduction was particularly important for the fifth subharmonic, $\Delta\widehat{H_{f_{1/5p}}}$, representing 5% of the observed amplification of significant wave height at $x = 190$ m against 10% at $x = 130$ m for $|\mathcal{K}|$=2.4. In contrast, convex edge curvature below 1.8 inhibited the formation of a divergence zone, ensuring the sustainability of wave ray convergence across the entire platform. Under these conditions, the wave height anomalies within the WW and SW frequency bands were sustained across the entire platform, and anomalies within the IG_L frequency band were amplified over the inner platform ($\Delta\widehat{H_{f_{1/5p}}}$ representing 15% of the observed amplification of normalised significant wave height at $x = 190$ m for $|\mathcal{K}|$=1.2) to become the dominant type of anomaly at this location. Thus, $\Delta\widehat{H_s}$ became predominantly controlled by the behaviour of IG_L as curvature decreased ($1.4 < \mathcal{K} < 1.8$). For very low degrees of curvature ($\mathcal{K} < 1.4$), the amplification of IG_L was of such importance that $\Delta\widehat{H_s}$ were amplified over the inner platform despite the decrease in wave convergence, resulting in a negative correlation (- 0.6 < ρ_s< - 0.4) between $\Delta\widehat{H_s}$ and directional patterns (Fig. 5c).

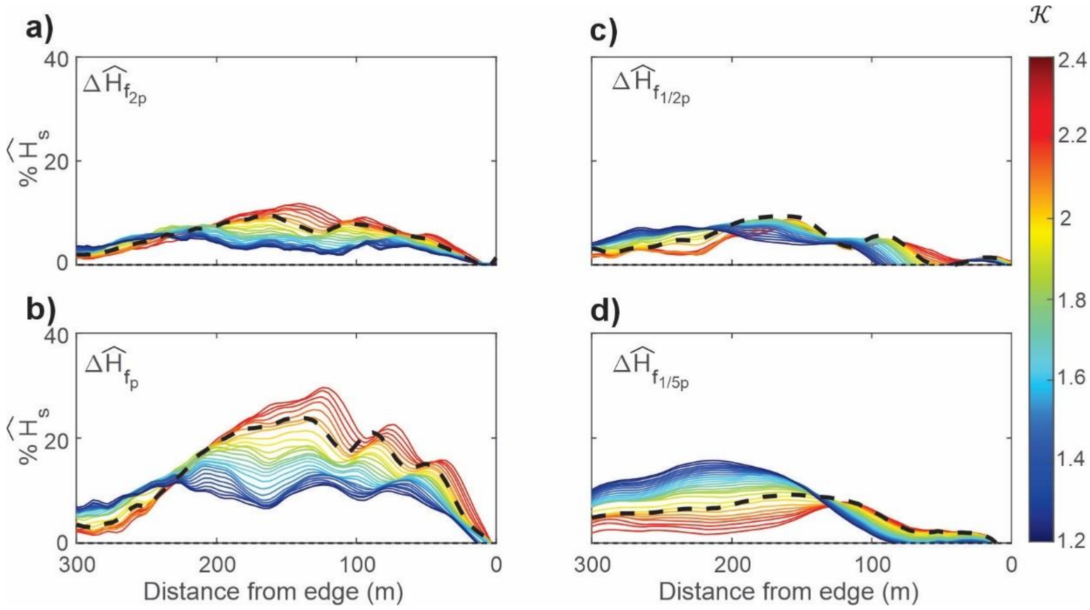

Figure 6: Percentage of significant wave height variations across the centreline (y = 150 m) convex platforms associated with anomalies of the second higher harmonics (a), the principal harmonic (b), the second subharmonic (c) and the fifth subharmonic (d) components (H_s=$H_{s_{Straight}} + \Delta H_s$). The dashed line represents a curvature of 1.8, marking the threshold for the formation of a divergence zone over the inner platforms.

3.2 Effects of platform edge geometry on alongshore wave height patterns

3.2.1 Non-breaking waves

Coherent self-interaction maps were plotted to investigate the impact of platform edge geometry on alongshore wave height variation over the inner platform for non-breaking waves (Fig. 7). Maxima in these maps ($\hat{\psi} \approx 1$) correspond to areas of strongest coherent interaction for the dominant frequency components within the SW and IG_L frequency bands (f_p and $f_{1/5p}$). Over the concave platforms, zones of coherent self-interaction for the principal harmonic (f_p) shifted alongshore from the platform centrelines to become concentrated near the northern and southern extremities of the platform as the edge curvature increased (Fig. 7a-d). These alongshore variations were predominantly observed between x = 130 and 175 m, where divergence along the centreline was the strongest (Fig. 3c). In contrast, coherent self-interaction maps for the fifth subharmonic ($f_{1/5p}$) were more homogenous alongshore (Fig. 7e-h), except near the shoreline, where coherent self-interactions were predominantly observed at the platform centreline. Over the convex platform, coherent self-interactions of the principal harmonic (Fig. 7i-l) were concentrated toward the platform centreline for edge curvatures between $|\mathcal{K}|$=1.2 to 1.6 (Fig. 7k,l), but as edge curvature increased, coherent wave interaction for this harmonic predominantly occurred at the northern and southern extremities of the platforms (Fig. 7i,j). For the fifth subharmonic, coherent self-interactions were focussed near the platform centreline for low edge curvature and spread alongshore toward the shoreline $|\mathcal{K}|$=1.2 (Fig. 7p). As curvature increased, the areas of fifth subharmonic coherent self-interactions near the shoreline split into two peaks on either side of the platform centreline (Fig. 7m,n). This phenomenon was observed at curvatures for which a mild divergence was observed over the inner platform (Fig. 3d).

The wave height distribution over the inner sections of concave and convex platforms is shown in Fig. 8 and 9. The spatial distribution of the significant wave height $(\widehat{H_s})$ presented the strongest similitudes (R^2 > 0.9) with the wave height patterns of the principal harmonic $(\widehat{H_{f_p}})$ regardless of the platform geometry and curvature. This Indicates a strong control of SW on the patterns of significant wave height variations over the inner platform. In contrast, the correlation between the wave height patterns of the fifth subharmonic and the significant wave height patterns over the inner platforms of concave and convex geometries was weak (R^2 < 0.4), indicating that IG_L had little impact on the variations of significant wave height at this location.

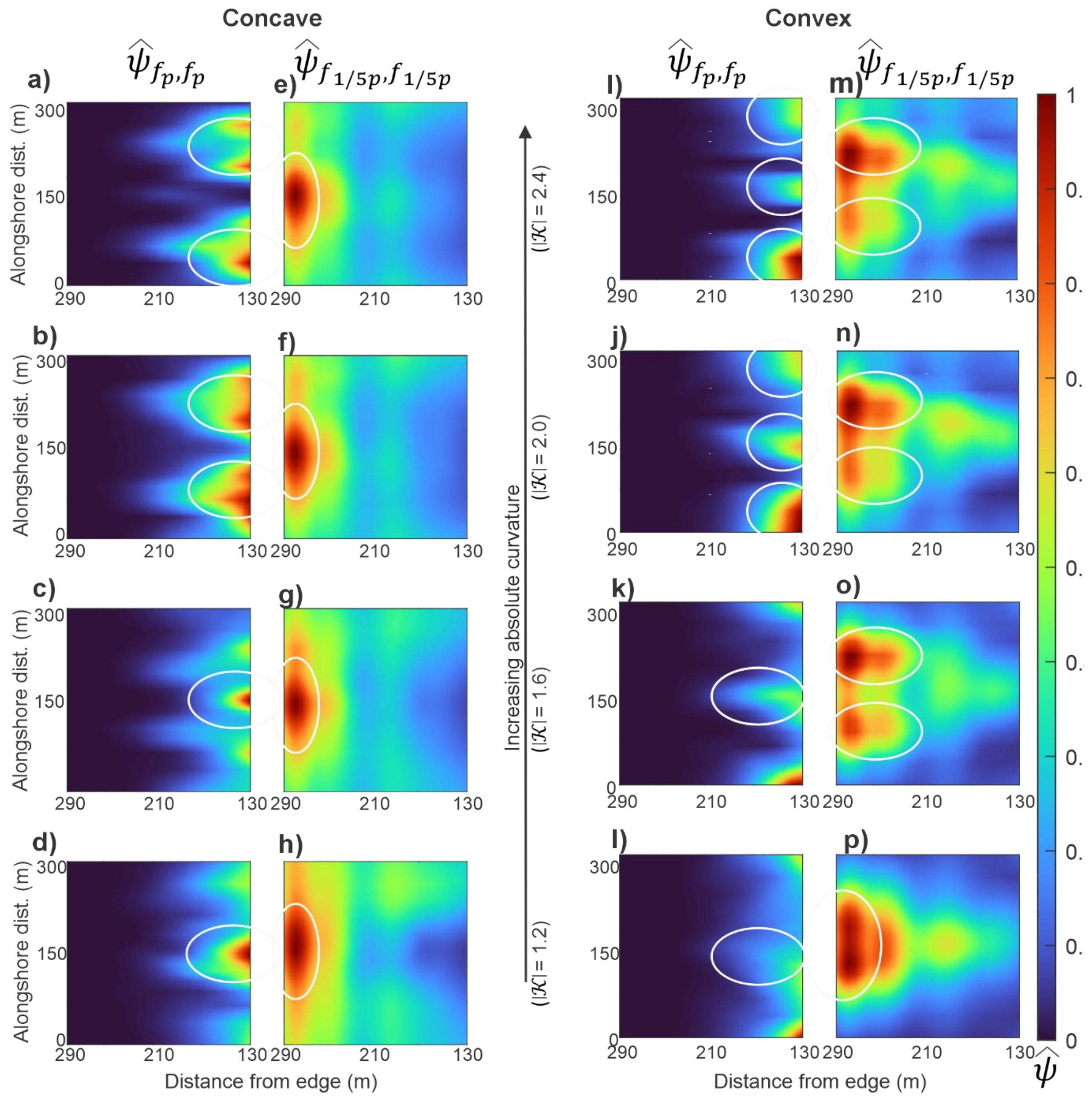

Figure 7: Coherent self-interaction maps defined from the bispectral modal state of self-interacting components for the principal harmonic (f_p) and the fifth subharmonic ($f_{1/5p}$) of non-breaking waves over the inner platform (Fig. 1) at different concave (a-h) and convex (i-p) edge curvatures. The centreline is located at y =150 m. Values of $\widehat{\psi}$ of 1 indicate areas of the largest coherent wave interactions. The white ellipses highlight the zones of strong coherent wave interactions.

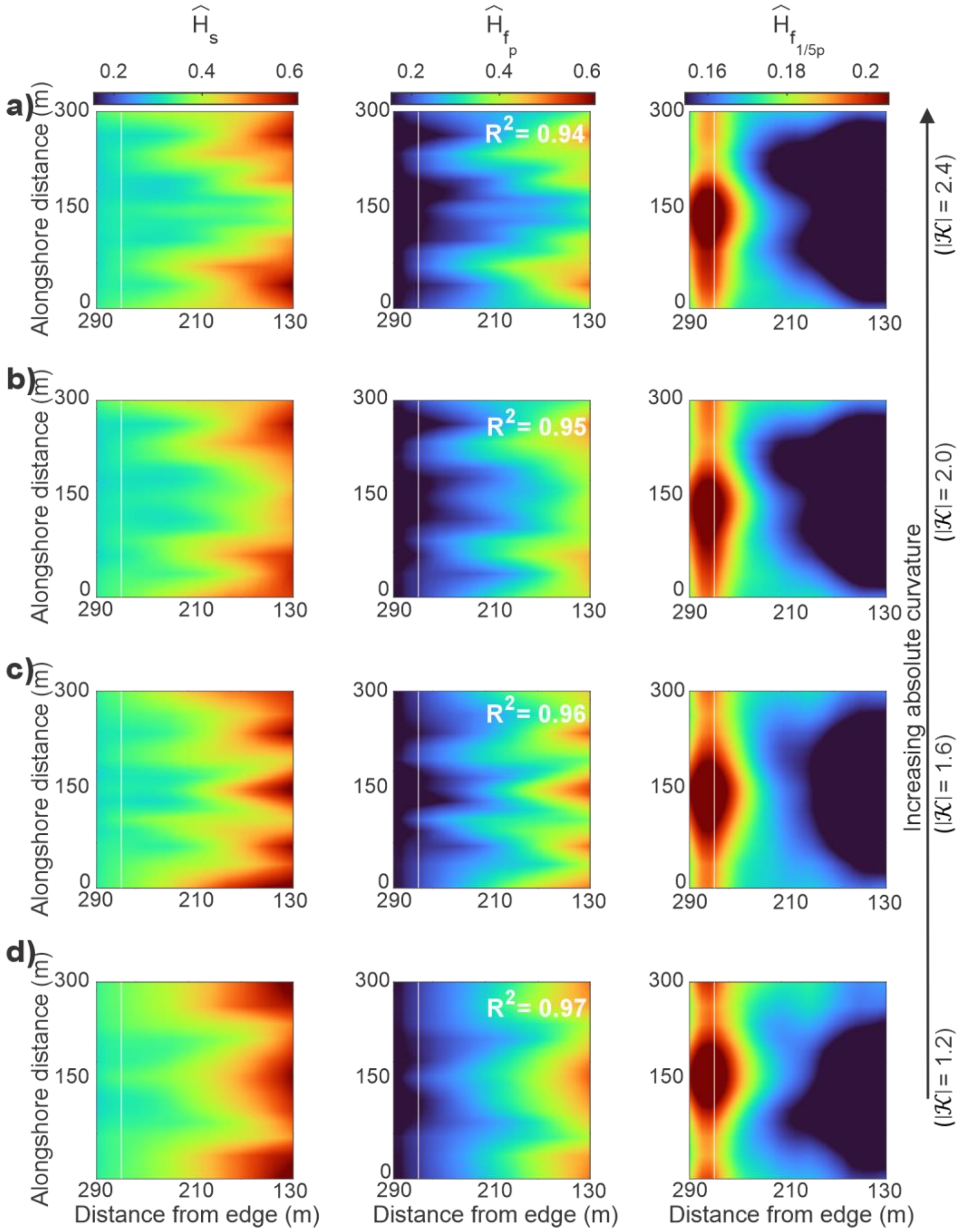

Figure 8: Wave height distribution for the entire frequency range $(\widehat{H_s})$, the principal harmonic $(\widehat{H_{f_p}})$ and the fifth subharmonic $(\widehat{H_{f_{1/5p}}})$ of non-breaking waves over the inner platform (Fig. 1) for various concave (a-d) edge curvatures. The white line represents the alongshore transect L, 20 m from the shoreline (Fig. 1). The centreline is located at $y = 150$ m. The R^2 values indicate the correlation between wave height patterns of the principal harmonic and fifth subharmonic with the significant wave height pattern for the same degree of curvature (only $R^2 \geq 0.4$ is shown, representing moderate to very strong correlations)

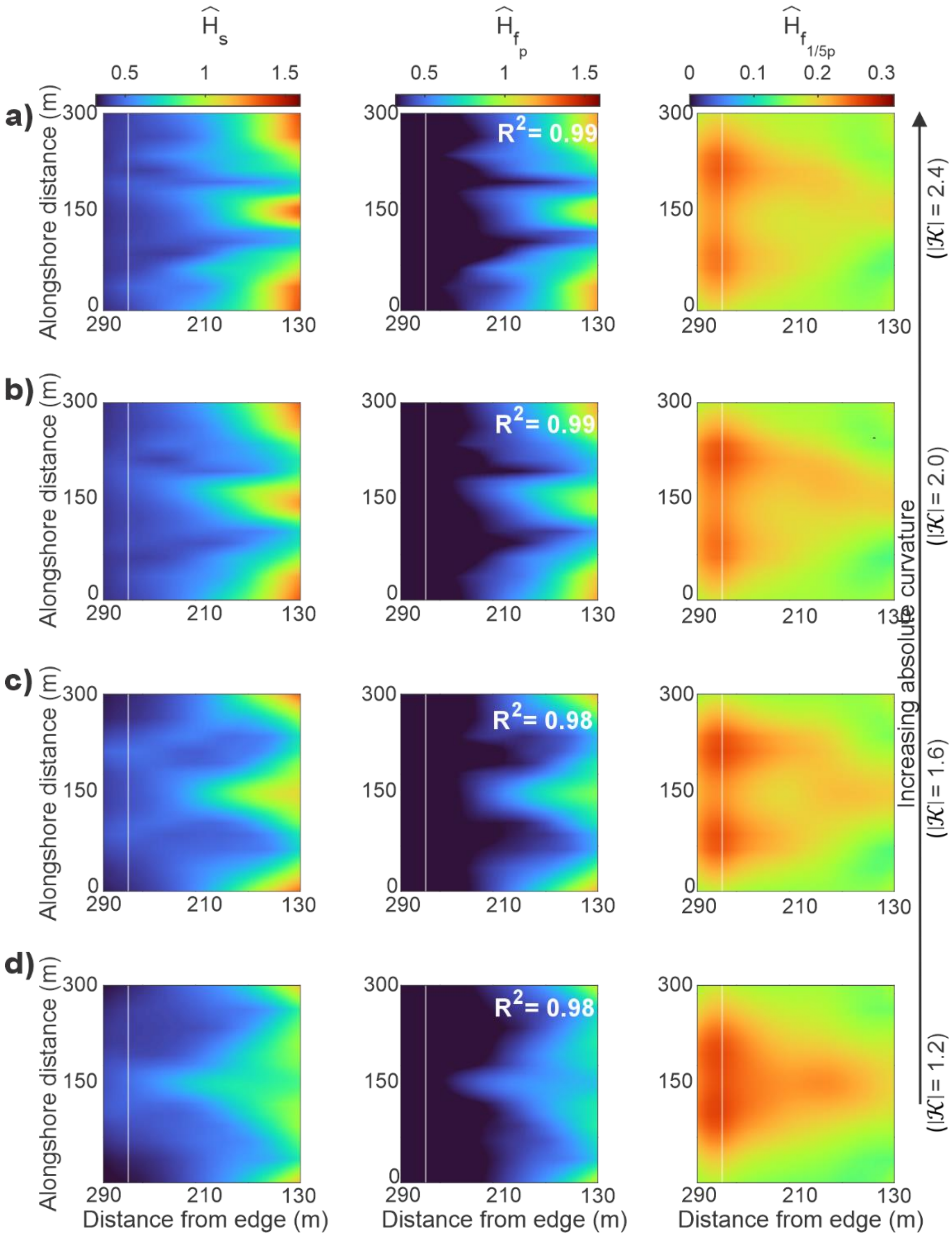

Figure 9: Wave height distribution for the entire frequency range ($\widehat{H_s}$), the principal harmonic ($\widehat{H_{f_p}}$) and the fifth subharmonic ($\widehat{H_{f_{1/5p}}}$) of non-breaking waves over the inner platform (Fig. 1) for various convex (a-d) edge curvatures. The white line represents the alongshore transect L, 20 m from the shoreline (Fig. 1). The centreline is located at $y = 150$ m. The R^2 values indicate the correlation between wave height patterns of the principal harmonic and fifth subharmonic with the significant wave height pattern for the same degree of curvature (only $R^2 \geq 0.4$ is shown, representing moderate to very strong correlations)

A strong relationship, $R^2 > 0.8$, was observed between modal coherent self-interaction patterns and wave height patterns of the principal harmonic and fifth subharmonics over the inner sections of concave (Fig. 10a) and convex platforms (Fig. 10b). This observation indicates that the alongshore variations of the principal harmonic (SW) were predominantly controlled by coherent wave interaction, which in turn drove the alongshore variations in significant wave height over the inner section of both concave and convex platforms. The resulting stationary patterns in significant wave height along the shoreline were characterised by a decrease of significant wave height toward the centreline of concave platforms (Fig. 11a), which became more pronounced with increasing curvature (maximum alongshore difference in $\widehat{H_s}$=0.05 at $|\mathcal{K}|$=1.2, increasing to 0.06 at $|\mathcal{K}|$=2.4, Fig. 10a). Over convex platforms, stationary patterns for normalised significant wave height were characterised by an increase of significant wave height toward the platform centreline at low degrees of curvature (Fig. 11b), resulting in an alongshore difference in $\widehat{H_s}$ ≈0.15 for $|\mathcal{K}|$<1.8 near the shoreline. A progressive amplification of the lobes on either side of the centreline was observed as curvature increased, resulting in a more homogenous alongshore distribution of significant wave height for high degrees of curvature ($\widehat{H_s}$ ≈0.06 for $|\mathcal{K}|$>2, Fig. 11b).

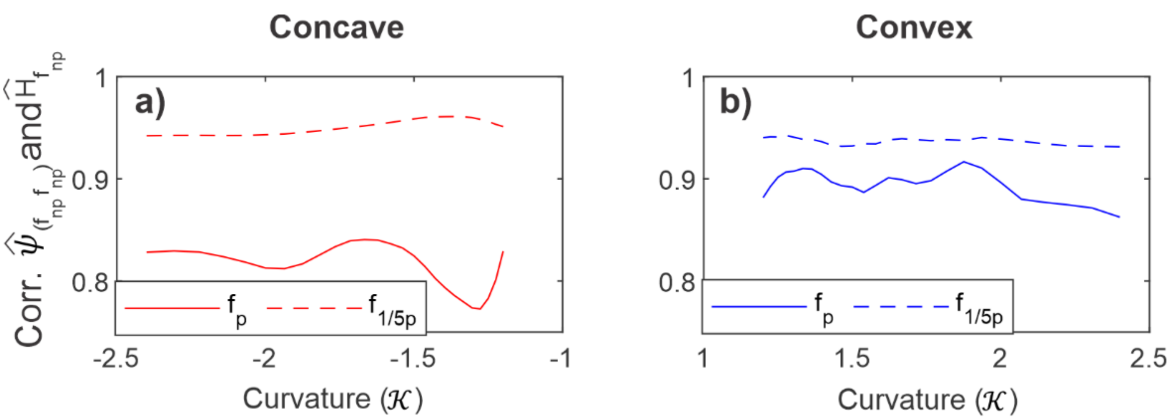

Figure 10: Correlation between interaction maps (Fig. 7) and wave height patterns (Fig. 8, 9) for the principal harmonic (f_p) and the fifth subharmonic ($f_{1/5p}$) of non-breaking waves over the inner platform of concave (a) and convex (b) edges.

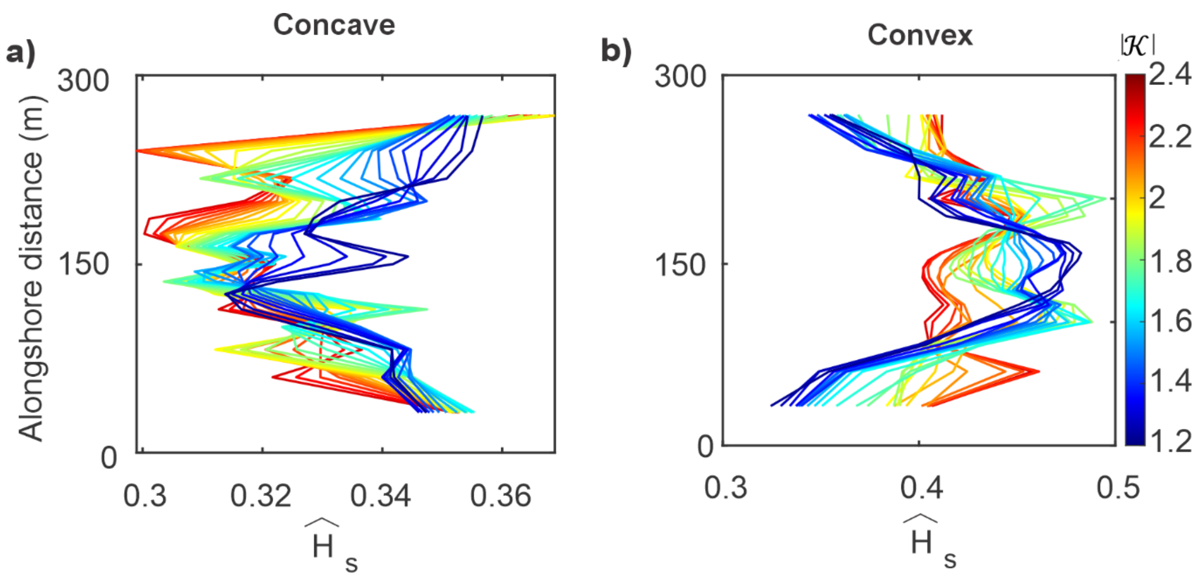

Figure 11: Alongshore variations in significant wave height patterns 20 m from the shoreline for non-breaking waves (transect L, Fig. 1) in relation to concave (a) and convex (d) edge curvatures

3.2.2 Broken waves

Coherent self-interaction patterns of the principal harmonic and fifth subharmonic of broken waves displayed alongshore variabilities over both concave and convex platforms (Fig. 12). Over the concave platforms, the coherent self-interaction zone of the principal harmonic was concentrated toward the centreline for low degrees of curvature ($|\mathcal{K}|$=1.2), spreading alongshore as the degree of curvature increased (Fig. 12a-d). Zones of coherent self-interactions for the fifth subharmonic were predominantly observed on the northern and southern extremities of the platforms and became more distinct as the edge curvature increased (Fig. 12e-h). Over the convex platforms, coherent self-interactions of the principal harmonic were the strongest on the northern and southern extremities of the platforms at $x \approx 190$ m. For the fifth subharmonic (Fig. 12m-p), areas of coherent self-interaction were concentrated along the platform centrelines for low degrees of curvature ($|\mathcal{K}|$=1.2 and 1.6), but spread either side of the platform centrelines for high degrees of curvature ($|\mathcal{K}|$=2.0 and 2.4). The differences in coherent self-interaction patterns between low and high degrees of curvature were characterised by a mild divergence over the inner section of convex platforms for curvatures greater than 1.8 (Fig. 7d).

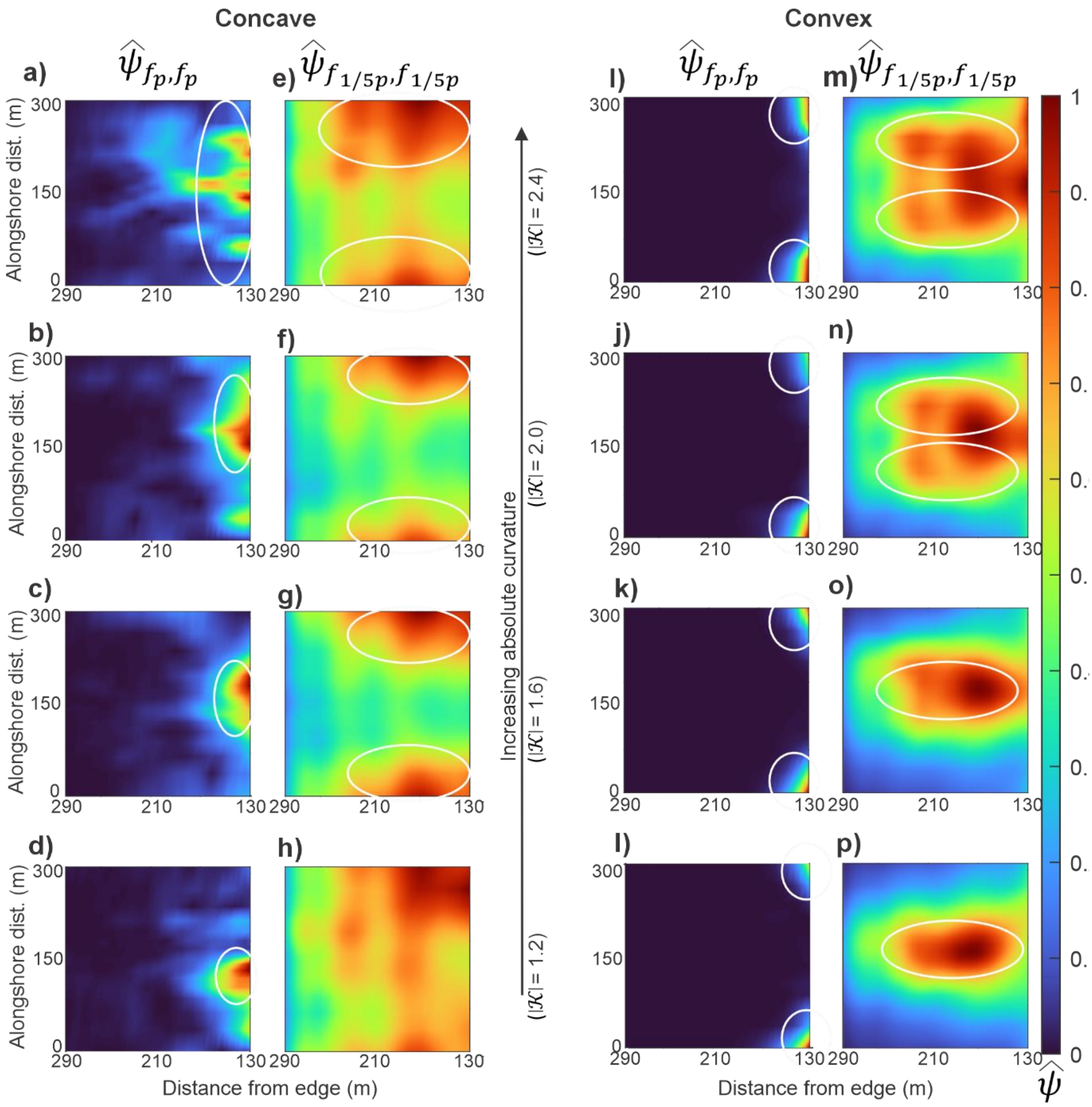

Figure 12: Coherent self-**i**nteraction maps defined from the bispectral modal state of self-interacting components for the principal harmonics (f_p) and the fifth subharmonic ($f_{1/5p}$) of broken waves over the inner platform (Fig. 1) at different concave (a-h) and convex (i-p) edge curvatures. The centreline is located at $y = 150$ m. Values of $\hat{\psi}$ of 1 indicate areas of strong coherent wave interactions. The white ellipses highlight the zones of strong coherent wave interactions.

For broken waves, the influence of IG_L on significant wave height distribution over the inner sections of concave and convex platforms was greater than for non-breaking waves (Fig. 13, Fig. 14). Over the inner section of the concave platforms (Fig. 13), the fifth subharmonic had greater wave height than the principal harmonic. Thus, the wave height patterns of the fifth subharmonic had a greater impact on the significant wave height patterns ($0.85 < R^2 < 0.91$ for $1.2< |\mathcal{K}|< 2.4$) than the principal harmonic ($0.74 < R^2 < 0.86$ for $1.2< |\mathcal{K}|< 2.4$) in this region. The wave height of the principal harmonic and fifth subharmonic decreased from the northern and southern extremities of the platforms to the platform centrelines. The combined effect of these patterns was a net alongshore decrease of significant wave height toward the platform centrelines. Over the inner section of convex platforms (Fig. 14), the principal harmonic displayed the greatest wave height (maximum $\widehat{H_{f_p}} \approx 0.5$) on the northern and southern sides of the platform between $x \approx$ 130-190 m. The wave height of the fifth subharmonic was relatively smaller, reaching a maximum at the platform centreline (maximum $\widehat{H_{f_p}} \approx$ 0.22-0.27), regardless of the curvature. As a result, the wave height distribution of the principal harmonic exerted a strong control on the significant wave height pattern over the inner platforms ($0.9 < R^2 < 0.95$) in comparison to the control exerted by the fifth subharmonic ($0.4 < R^2 < 0.58$). However, the wave height of the principal harmonic significantly decreased past $x \approx 190$ m, becoming comparable to the wave height of the fifth subharmonic. Thus, alongshore variations in significant wave height were controlled by alongshore patterns of both principal harmonic and fifth subharmonic for $x \geq 190$ m. For low degrees of edge curvature ($|\mathcal{K}|$=1.2), the maximum wave height of the fifth subharmonic was observed at the platforms' centreline and evolved with increasing curvature to form two maxima on either side of the centreline for large degrees of edge curvature ($|\mathcal{K}|$= 2.2 and 2.4). This evolution was clearly observed in the significant wave height pattern between $x =$ 190 and 300 m, underlining the influence of the fifth subharmonic (IG_L) on the alongshore variation of significant wave height at the shoreline.

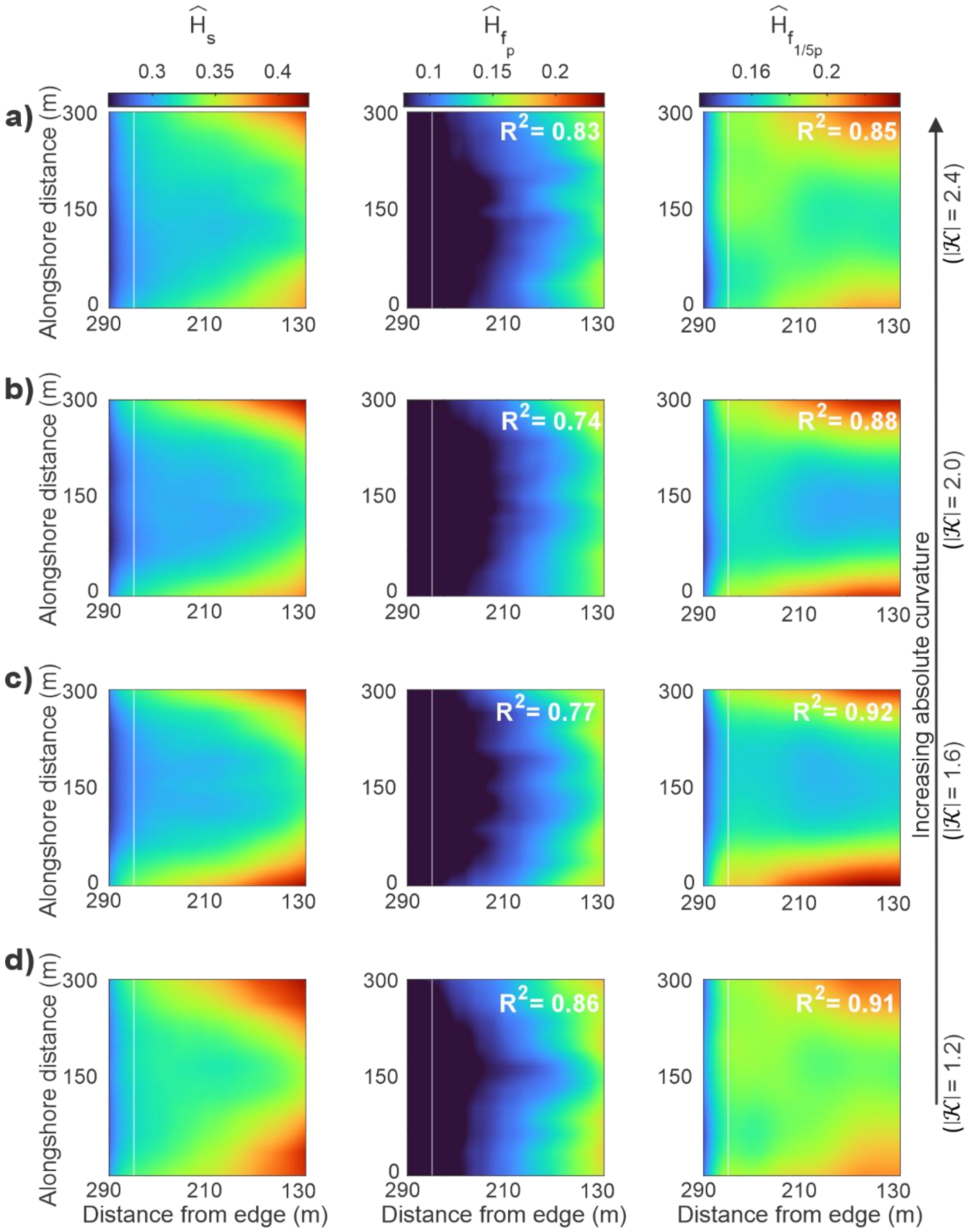

Figure 13: Wave height distribution for the entire frequency range ($\widehat{H_s}$), the principal harmonic ($\widehat{H_{f_p}}$) and the fifth subharmonic ($\widehat{H_{f_{1/5p}}}$) of broken waves over the inner platform (Fig. 1) for various concave (a-d) edge curvatures. The white line represents the alongshore transect L, 20 m from the shoreline. The centreline is located at $y = 150$ m. The R^2 values indicate the correlation between wave height patterns of the principal harmonic and fifth subharmonic with the significant wave height pattern for the same degree of curvature.

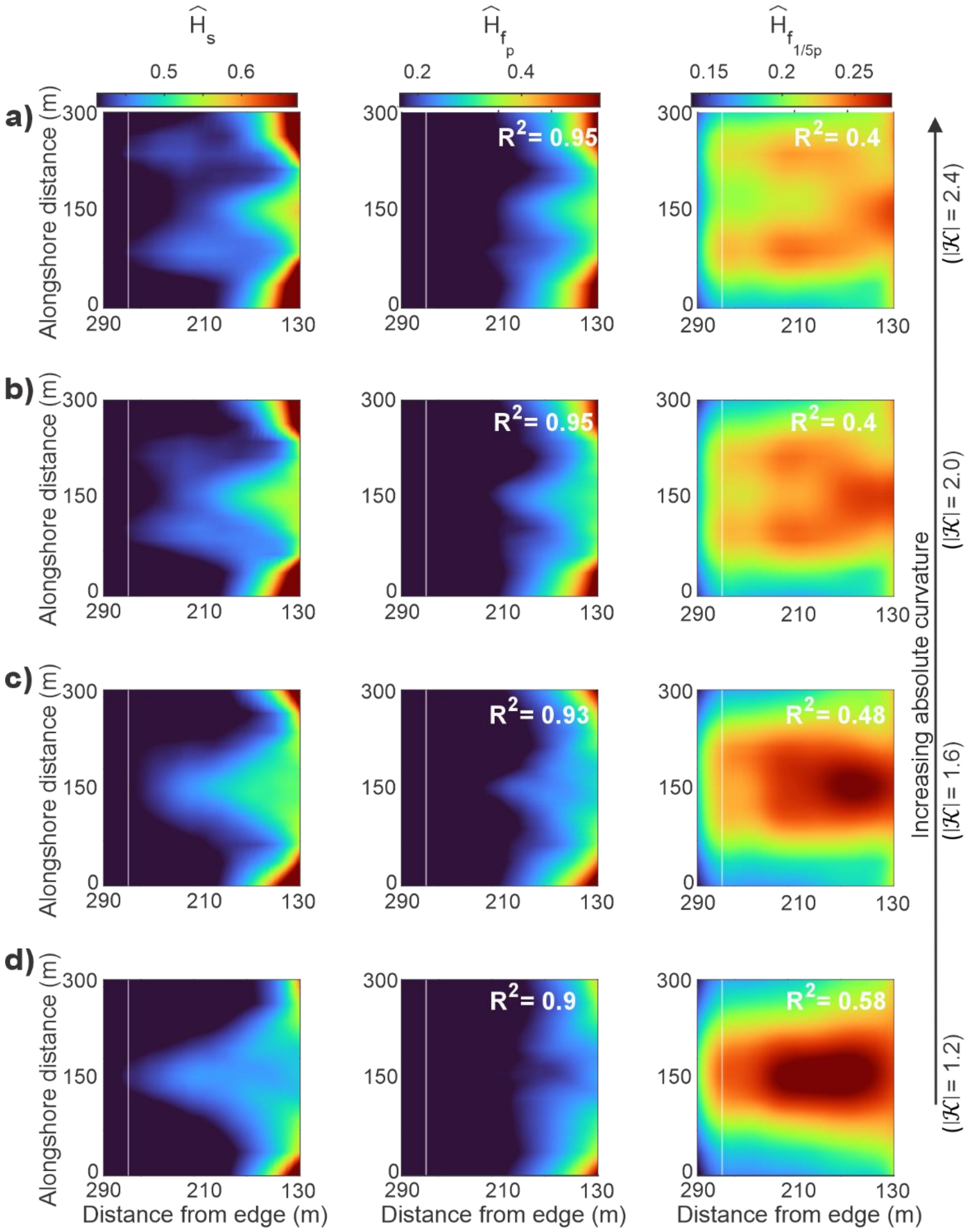

Figure 14: Wave height distribution for the entire frequency range ($\widehat{H_s}$), the principal harmonic ($\widehat{H_{f_p}}$) and the fifth subharmonic ($\widehat{H_{f_{1/5p}}}$) of broken waves over the inner platform (Fig. 1) for various convex (a-d) edge curvatures. The white line represents the alongshore transect L, 20 m from the shoreline. The centreline is located at y =150 m. The R^2 values indicate the correlation between wave height patterns of the principal harmonic and fifth subharmonic with the significant wave height pattern for the same degree of curvature.

Strong ($R^2 > 0.8$) and moderate to strong ($0.5 < R^2 < 0.7$) relationships were observed over the inner sections of concave (Fig. 15a) and convex platforms (Fig. 15b) between modal coherent self-interaction patterns and wave height patterns for the fifth subharmonics and principal harmonics, respectively. The implication is that coherent wave amplification influenced the longshore patterns of wave height for the principal harmonic and fifth subharmonic over the inner platform, although this process had a smaller impact on the principal harmonic. Thus, coherent wave amplification at IG frequencies was the principal process controlling alongshore variations of significant wave height along the shoreline. The resulting stationary patterns in significant wave height along the shoreline were marked by a decrease of significant wave height toward the centreline of concave platforms, which became more pronounced with increasing curvature (maximum alongshore difference in $\widehat{H_s}$=0.04 at $|\mathcal{K}|$=1.2, increasing to 0.02 at $|\mathcal{K}|$=2.4, Fig. 16a). For convex platforms, an increase of significant wave height toward the platform centreline was observed at low degrees of curvature, resulting in maximum alongshore variations of significant wave height $\widehat{H_s} \approx 0.08$ for $|\mathcal{K}|$<1.8. A progressive amplification of the lobes on either side of the centreline generated two wave height maxima for high degrees of curvature, for which maximum alongshore variations of significant wave height $\widehat{H_s} \approx 0.06$ for $|\mathcal{K}|$>2 (Fig. 16b).

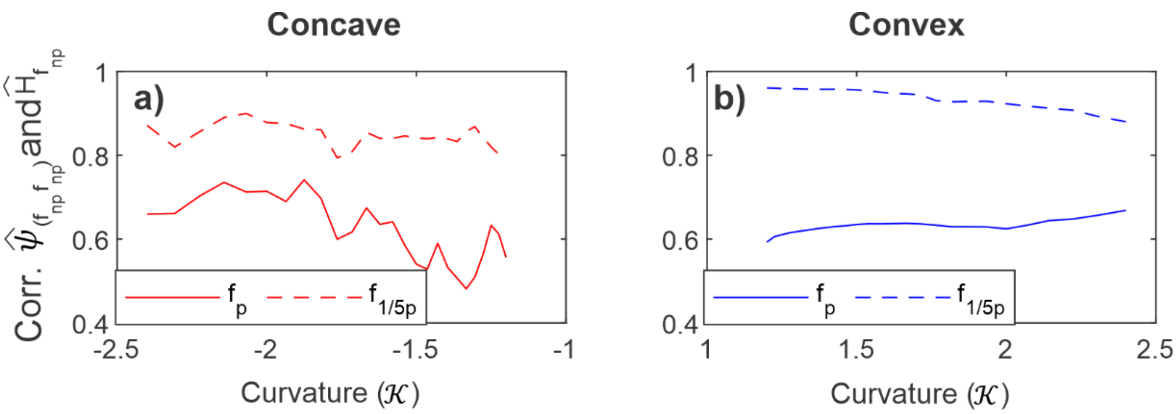

Figure 15: Correlation between interaction maps and wave height patterns for the principal harmonic (f_p) and the fifth subharmonic ($f_{1/5p}$) of broken waves over the inner platform of concave (a) and convex (b) edges.

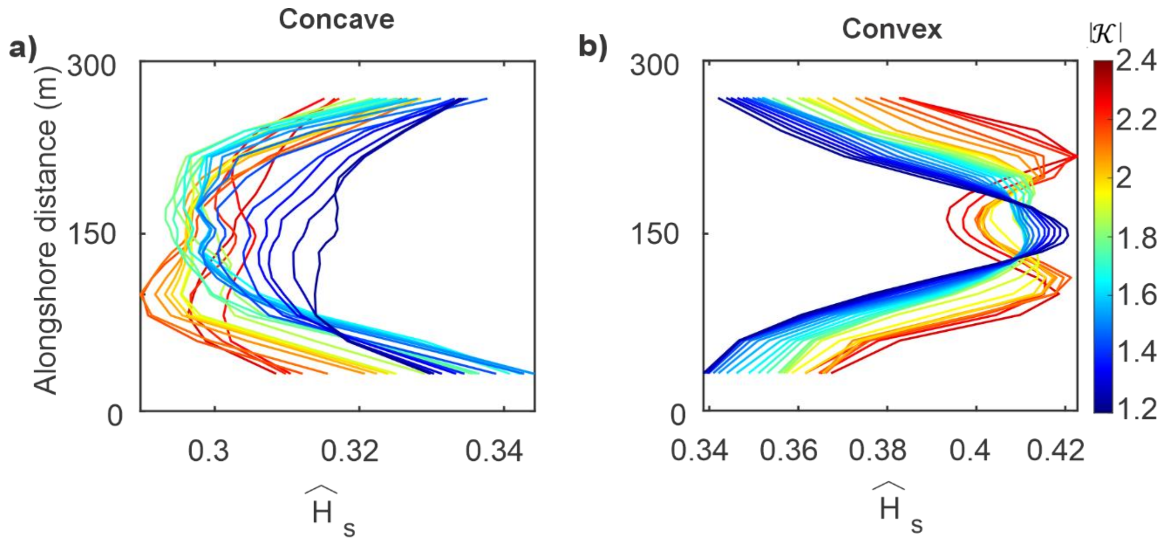

Figure 16: Alongshore variations in normalised significant wave height patterns 20 m from the shoreline (transect L) for broken waves in relation to concave (a) and convex (d) curvature.

4 Discussion

4.1 Impact of platform edge geometry on wave transformation across shore platforms

Modelling studies generally investigate the impact of refraction on wave energy distribution over a fixed curvature (e.g. Berkhoff et al., 1982; Li et al., 2020), whereas in this work, we varied the degree of edge curvature and analysed its effect on the transformation of harmonic components. Increasing concave edge curvature decreased the wave energy of harmonic components in WW, SW, IG_H and IG_L frequency bands (Fig. 2b-e, 4b-e), accounting for up to 25% reduction in $\widehat{H_S}$ (Fig. 3a, 5a). In contrast, increasing convex edge curvature amplified both the second and principal harmonics in the WW and SW frequency bands over the outer platforms, increasing $\widehat{H_S}$ by up to 55% and 18% for non-breaking and broken waves (Fig. 3b, 5b) while minimizing the amplification of the fifth subharmonic within the IG_L frequency band over the inner platforms (Fig. 2g-j, 4g-j). Thus, it is clear that morphological variability in platform edge curvature influences significant wave height on shore platforms, and this has potential implications for backwear and downwear erosion processes on rock coasts (e.g. Trenhaile, 1987, Matsumoto et al., 2016a,b).

Amplification of higher harmonics associated with wave refraction has previously been associated with wave focusing (Gouin et al., 2017), but the impact of edge curvature on amplification has not been considered. Our modelling results show that increasing convex edge curvature enhances wave focussing over the outer platform (Fig. 3, 5), promoting the generation of higher harmonic from non-linear triadic (sum) interactions (Janssen and Herbers, 2009; Jarry et al., 2011; Lawrence et al., 2022). Shore platform studies have linked the generation and dominance of high-frequency waves over the outer section of near-horizontal platforms to locally generated wind waves (e.g. Ogawa et al., 2011; 2016). Though this process cannot be ruled out, the nearshore wind speed required for locally produced WW energy is substantial (Hasselmann et al., 1973), and the generation of higher harmonics from non-linear triadic interaction caused by wave refraction appears to be a more plausible physical interpretation for high-frequency wave generation on the outer sections of shore platforms.

Research has demonstrated that wave amplification in the IG frequency band over near-horizontal platforms is influenced by the ratio of water depth at the cliff toe to the platform width, and relative submergence (Beetham and Kench, 2011; Ogawa et al., 2015). We show that edge curvature exerts an additional morphological control on IG amplification across convex platforms by affecting the balance between focusing intensity from refraction and defocusing effects from wave breaking controlled by convex edges (Fig. 4, 5). Although a decrease in convex edge curvature should theoretically result in a landward shift of the focal point over submerged flats (e.g. Mandlier and Kench, 2012), a seaward shift of the focal point was observed in this study for broken waves (Fig. 5d). This phenomenon can be attributed to the defocussing effects resulting from the enhancement of radiation stress and wave-generated current by wave breaking (Yoon et al., 2004; Choi et al., 2009). A critical curvature was found for which the intensity of wave focusing by wave refraction is not strong enough to overcome the defocusing effects of wave breaking, identified here as $|\mathcal{K}|$=1.8 (Fig. 5d). When the critical curvature is exceeded, wave rays intersect across the platform centreline, in which cases, IG amplification is minimised by wave ray divergence over the inner platform (Fig. 6d). In contrast, for convex edge curvatures lower than the critical curvature, wave rays do not intersect across the platform centreline, sustaining wave convergence across the entire platform. In this case, IG amplification is promoted over the inner platform, representing up to 15% of the increase in significant wave height at this position (Fig. 6d). Thus, the present research identifies convergence as a key mechanism acting on the growth of IG across shore platform, working in conjunction with other processes such as to breakpoint forcing (Poate et al., 2020) and energy transfer from higher frequencies and shoaling (Beetham and Kench, 2011).

In a conceptual model, Ogawa et al. (2011) described spatial zones on a shore platform that are dominated by different wave types and pointed out that the spatial characteristics change according to the tidal stage. Here, we show that shifts in dominant wave types across shore platforms are also controlled by convex edge curvature (certainly at high tide). High convex curvature amplifies harmonics within the WW and SW frequency bands over the outer platform and inhibits the amplification of IG over the inner platform (Fig. 4g). Low degrees of convex curvature have the opposite effect (Fig. 4j), resulting in the seaward shift of the zones dominated by WW and SW frequency bands. The influence of refraction patterns generated by convex edge geometries on the collective behaviour of harmonics affected the significant wave height patterns across convex platforms. Baldock et al. (2020) hypothesised that the significant wave height across convex platforms is defined by a specific balance between cross-shore energy loss from dissipation and energy gain from oblique refracted SW, resulting in a correlation between significant wave height anomalies and refraction patterns. The strong relationship ($\rho_s > 0.6$) observed between directional patterns and significant wave height anomalies of non-breaking waves (Fig. 3f) suggest that, for this wave state, energy is effectively gained across the platform from refracted SW. However, for broken waves, the correlation between directional patterns and significant wave height anomalies ($\Delta\widehat{H_s}$) decreased with curvature to become weak ($\rho_s < 0.4$) below the critical curvature threshold (Fig. 5f). These differences are attributed to the influence of IG growth on significant wave height over the inner platform due to the amplification of IG from post-breaking energy transfer from high to low frequency (Poate et al., 2020), and low sustained convergence across the platform (Fig. 5b, 6d). These results underline the importance of considering the refraction patterns of both SW and IG when investigating significant wave height patterns across convex submerged flats.

4.2 Impact of platform edge geometry on along shore wave transformation

Coherent wave amplification is identified here as a crucial process affecting SW and IG_L height distribution in the inner section of near-horizontal platforms. For non-breaking waves, the dominant frequencies within both SW and IG_L frequency bands presented strong correlations between patterns of coherent wave interaction and wave height distribution over concave and convex platforms (Fig. 10). However, this correlation decreased for the principal harmonic in the SW frequency bands in the presence of wave breaking (Fig. 15), perhaps due to the combination of defocussing (Yoon et al., 2004) and dissipation effects (Farrell et al., 2009) associated with wave breaking.

The present observations validate the hypothesis of Winter et al. (2017) on the formation of alongshore stationary IG patterns from wave refraction over convex platforms. However, our results suggest that such patterns are generated by coherent wave interaction following the generation of caustic rays in the IG_L frequency band (Fig. 7m-p, 12m-p) rather than alongshore standing waves, as Winter et al. (2017) suggested. In fact, the latter would require interacting IG to propagate alongshore in opposite directions. The directional analysis presented here precludes such a possibility ($\alpha \approx 0°$ near the shoreline, Fig. 3, 5). As the present paper demonstrates the coherent wave interaction plays crucial role in alongshore IG wave patterns, a coherent wave class should be added to the resonant, progressive-dissipative, standing and progressive-growing low-frequency wave classes previously identified over submerged flats (Gawehn et al., 2016).

The combined modes of SW and IG coherent wave amplification exerted a crucial control on the stationary patterns of significant wave heights over the inner platform. For non-breaking waves, significant wave height variations over the inner platform are predominantly controlled by coherent wave amplification of SW (Fig. 7, 8). In contrast, for breaking waves, the distribution of significant wave height over the inner platform became controlled by coherent wave amplification occurring within both SW and IG_L frequency components as IG_L became a prominent wave type in this region (Ogawa et al. 2011) (Fig. 13, 14). The present results support the conceptual model presented by Krier-Mariani et al. (2022), suggesting that patterns of wave ray intersection on either side of concave edge sections result in stationary SW and IG amplification patterns. The control exerted by the critical curvature on the alongshore distribution of SW and IG over convex platforms can be attributed to the generation of a terminal point (marking the transition from wave ray convergence to divergence) at the platform centreline for convex curvatures exceeding the critical curvature. In such cases, caustic rays are formed on either side of the centreline (Mandlier and Kench, 2012), promoting coherent wave interactions in these regions (Fig. 12a, 14a).

It follows that the control exerted by platform curvature on coherent wave amplification plays an essential role in the nodal state of significant wave height along the shoreline (Fig. 11, 16). For concave platforms, a node near the centreline and antinodes on the northern and southern extremities of the platform were observed. For convex edge curvature under the critical curvature threshold, an antinode was observed along the platform centreline where waves converged, while for curvature exceeding the critical curvature threshold, two antinodes were observed on either side of the platform centreline. While such patterns could wrongly be associated with edge waves, the present results support the observations of Dalrymple (1975), who first associated nodal and anti-nodal points in alongshore wave height patterns with coherent wave interaction.

It has previously been established that by controlling the nodal state of significant wave height along the shoreline of open coasts, coherent wave amplification could lead to the formation of rip currents (Dalrymple, 1975; Wei and Dalrymple, 2017). This mechanism is expected to impact circulation patterns over near-horizontal platforms equally. da Silva et al. (2023) identified alongshore pressure gradient as the dominant driver of circulation patterns in the lee of submerged flats, resulting in two or four-cell circulation systems. A two-cell system is typically characterised by an alongshore diverging flow from the lee of the submerged flat edge to the shoreline, while a four-cell system is characterised by an alongshore diverging flow at the lee of the submerged flat and a converging flow at the shoreline. Considering the present results, it can be hypothesised that stationary wave patterns and the subsequent alongshore pressure gradient generated by coherent wave amplification drive the formation of circulation cells over convex platforms. Theoretically, the formation of two antinodes over the inner platform would result in a four-cell circulation system (Fig. 14a,b, Fig. 16b), while an antinode across the entire platform would result in a two-cell circulation system (Fig. 14c,d, Fig.16b). These differences depend on whether or not the submerged flat geometry allows for the formation of a terminal point. Previous studies established that this condition was predominantly controlled by the distance between the seaward edge of submerged flats and the shoreline (da Silva et al., 2022, 2023; Ranasinghe et al., 2006, 2010), while we show that the degree of edge curvature is equally important (Fig. 11, 16).

5 Conclusions

This study employed an exploratory numerical modelling approach to investigate the impact of concave and convex platform edge geometries on the behaviour of wave harmonics and the subsequent wave height distribution patterns over near-horizontal shore platforms. Harmonic analyses show that refraction patterns controlled by concave and convex platform edge curvatures result in wave height variation for the principal and second higher harmonics over the outer platform, and for the subharmonics over the inner platform. Wave divergence across concave edge platforms decreased the height of harmonics within both SW and IG frequency bands, resulting in the attenuation of significant wave height for high degrees of curvature. Over the outer section of convex platforms, increasing curvature intensified wave focusing and amplified the principal and second harmonics within the SW frequency band. A critical curvature value of 1.8 demarcates the formation of a wave ray divergence zone over the inner platform, conditioned by the balance between wave focusing from wave refraction and wave defocusing from wave breaking. Below this threshold, wave convergence amplified IG over the inner platform, but over this threshold, wave divergence reduced the amplification of IG over the inner platform. Through these mechanisms, it is apparent that edge curvature can influence both the relative dominance of SW and IG frequencies, and the pattern of significant wave height transformation across near-horizontal platforms. Using a high-order spectral decomposition method, this study further demonstrated that coherent wave amplification influences stationary IG and SW patterns over the inner platform, affecting the alongshore distribution of significant wave height. We found that platform geometry controls the nodal state of the stationary patterns along the shoreline, possibly resulting in alongshore variation of wave erosive force and the generation of wave-generated currents shaping rock coasts.

Acknowledgements

. RKM is supported by a University of Otago PhD Scholarship and a New Zealand Coastal Society Student Research Scholarship. Mark Dickson and Wayne Stephenson are supported by a Royal Society Te Apārangi, Marsden Fund Grant Number UOO1828. We are grateful for the assistance and support provided by Callum Walley and the rest of the team from NeSi for allowing us to set up and run our models on their supercomputer facilities.

Open research

The numerical model input files and post processed data for the model simulations (Using FUNWAVE 3.6) over idealised shore platform geometries are available at *Public release planned after review*.

References

Baldock, T.E., Shabani, B., Callaghan, D.P., Hu, Z., Mumby, P.J., 2020. Two-dimensional modelling of wave dynamics and wave forces on fringing coral reefs. Coast. Eng. 155, 103594. https://doi.org/10.1016/j.coastaleng.2019.103594

Beetham, E.P., Kench, P.S., 2011. Field observations of infragravity waves and their behaviour on rock shore platforms. Earth Surf. Process. Landforms 36, 1872–1888. https://doi.org/10.1002/esp.2208

Berkhoff, J.C.W., Booy, N., Radder, A.C., 1982. Verification of numerical wave propagation models for simple harmonic linear water waves. Coast. Eng. 6, 255–279. https://doi.org/10.1016/0378-3839(82)90022-9

Blenkinsopp, C.E., Chaplin, J.R., 2008. The effect of relative crest submergence on wave breaking over submerged slopes. Coast. Eng. 55, 967–974. https://doi.org/10.1016/j.coastaleng.2008.03.004

Buckley, M.L., Lowe, R.J., Hansen, J.E., Van Dongeren, A.R., 2015. Dynamics of wave setup over a steeply sloping fringing reef. J. Phys. Oceanogr. 45, 3005–3023. https://doi.org/10.1175/JPO-D-15-0067.1

Buckley, M.L., Lowe, R.J., Hansen, J.E., Van Dongeren, A.R., Storlazzi, C.D., 2018. Mechanisms of wave-driven water level variability on reef-fringed coastlines. J. Geophys. Res. Ocean. 123, 3811–3831. https://doi.org/10.1029/2018JC013933

Chen, Q., Dalrymple, R.A., Kirby, J.T., Kennedy, A.B., Haller, M.C., 1999. Boussinesq modeling of a rip current system. J. Geophys. Res. Ocean. 104, 20617–20637. https://doi.org/10.1029/1999jc900154

Chen, Q., Kirby, J.T., Dalrymple, R.A., Shi, F., Thornton, E.B., 2003. Boussinesq modeling of longshore currents. J. Geophys. Res. 108, 1–18. https://doi.org/10.1029/2002JC001308

Choi, J., Lim, C.H., Lee, J.I., Yoon, S.B., 2009. Evolution of waves and currents over a submerged laboratory shoal. Coast. Eng. 56, 297–312. https://doi.org/10.1016/j.coastaleng.2008.09.002

Dalrymple, R.A., 1975. A mechanism for Rip Current Generation on an open Coast. J. Geophys. Res. 80, 3485–3487.

da Silva, R. F., Hansen, J. E., Lowe, R. J., Rijnsdorp, D. P., & Buckley, M. L., 2023. Dynamics of the wave-driven circulation in the lee of nearshore reefs. Journal of Geophysical Research: Oceans, 128, e2022JC019013. https://doi.org/10.1029/2022JC019013

da Silva, R. F., Hansen, J. E., Rijnsdorp, D. P., Lowe, R. J., & Buckley, M. L. 2022. The influence of submerged coastal structures on nearshore flows and wave runup. Coastal Engineering, 177, 104194. https://doi.org/10.1016/j.coastaleng.2022.104194

Emery, W.J., Thomson, R.E., 2014. Time-series Analysis Methods, Data Analysis Methods in Physical Oceanography. Elsevier, Amsterdam. https://doi.org/10.1016/b978-044450756-3/50006-x

Falk, L., 1979. On The Phase Integral Of Coherent Three-wave Interaction. Phys. Lett. 71, 61–62.

Farrell, E.J., Granja, H., Cappietti, L., Ellis, J.T., Li, B., Sherman, D.J., 2009. Wave transformation across a rock platform, Belinho, Portugal. J. Coast. Res. 44–48.

Gawehn, M., Van Dongeren, A., Van Rooijen, A., Storlazzi, C.D., Cheriton, O.M., Reniers, A., 2016. Identification and classification of very low frequency waves on a coral reef flat. J. Geophys. Res. Ocean. 121, 3010–3028. https://doi.org/10.1002/2016JC011834.Received

Gouin, M., Ducrozet, G., Ferrant, P., 2017. Propagation of 3D non-linear waves over an elliptical mound with a High-Order Spectral method. Eur. J. Mech. B/Fluids 63, 9–24. https://doi.org/10.1016/j.euromechflu.2017.01.002

Gottlieb, S., Shu, C.-W., Tadmor, E., 2001. Strong stability-preserving high-order time discretization methods. SIAM Review 43, 89–112.

Griffiths, L.S., Porter, R., 2012. Focusing of surface waves by variable bathymetry. Appl. Ocean Res. 34, 150–163. https://doi.org/10.1016/j.apor.2011.08.004

Harid, V., Gołkowski, M., Bell, T., Li, J.D., Inan, U.S., 2014. Finite difference modeling of coherent wave amplification in the Earth's radiation belts. Geophys. Res. Lett. 41, 8193–8200. https://doi.org/10.1002/2014GL061787

Hashimoto, N., Nagai, T., Asai, T., 1994. Extension of the Maximum Entropy Principle Method for Directional Wave Spectrum Estimation, in: Coastal Engineering Proceedings. pp. 232–246. https://doi.org/10.1061/9780784400890.019

Hasselmann, K., Barnett, T.P., Bouws, E., Carlson, H., Cartwright, D.E., Enke, K., Ewing, J.A., Gienapp, H., Hasselmann, D.E., Kruseman, P., Meerburg, A., Muller, P., Olbers, D.J., Richter, K., Sell, W., Walden, H., 1973. Measurements of wind-wave growth and swell decay during the Joint North Sea Wave Project (JONSWAP). UDO 551.466.31; ANE German Bight, Deutsches Hydrographisches Institut Hamburg.

Hasselmann, K., Munk, W.H., MacDonald, G., 1963. Bispectra of Ocean Waves, in: Rosenblatt, M. (Ed.), Symposium on Time Series Analysis. pp. 125–139.

Inouye, S., Pfau, T., Gupta, S., Chikkatur, A.P., Görlitz, A., Pritchard, D.E., Ketterle, W., 1999. Phase-coherent amplification of atomic matter waves. Nature 402, 641–644.

https://doi.org/10.1038/45194

Ito, Y., Tanimoto, K., 1972. A Method of Numerical Analysis of Wave Propagation-Application To Wave Diffraction and Refraction. Proc. 13Th. Coast. Engng. Conf., (Vancouver, Canada) 1, 503–522. https://doi.org/10.9753/icce.v13.25

Janssen, T.T., Herbers, T.H.C., 2009. Non-linear wave statistics in a focal zone. J. Phys. Oceanogr. 39, 1948–1964. https://doi.org/10.1175/2009JPO4124.1

Jarry, N., Rey, V., Gouaud, F., Lajoie, D., 2011. Gravity wave amplification and phase crest re-organization over a shoal. Nat. Hazards Earth Syst. Sci. 11, 789–796. https://doi.org/10.5194/nhess-11-789-2011

Kennedy, A.B., Kirby, J.T., Chen, Q., Dalrymple, R.A., 2001. Boussinesq-type equations with improved non-linear performance. Wave Motion 33, 225–243. https://doi.org/10.1016/S0165-2125(00)00071-8

Kim, Y.C., Powers, E.J., 1979. Digital Bispectral Analysis and Its Applications to Non-linear Wave Interactions. IEEE Trans. Plasma Sci. 7, 120–131. https://doi.org/10.1109/TPS.1979.4317207

Kozuma, M., Suzuki, Y., Torii, Y., Sugiura, T., Kuga, T., Hagley, E., Deng, L., 1999. Phase-Coherent Amplification of Matter Waves. Science (80-.). 286, 2309–2312.

Stephenson, W.J., Kirk, R.M., 2000a. Development of shore platforms on Kaikoura Peninsula , South Island , New Zealand Part One : The role of waves. Geomorphology 32, 21–41.

Krier-Mariani, R.L., Stephenson, W.J., Wakes, S.J., Dickson, M.E., 2023. The effects of planform morphology on two-dimensional wave transformation over near-horizontal shore platforms. Geomorphology 422, 108555. https://doi.org/10.1016/j.geomorph.2022.108555

Krier-Mariani, R.L., Stephenson, W.J., Wakes, S.J., Dickson, M.E., 2022. Perspectives on wave transformation over a near-horizontal shore platform: Comparison of a two-dimensional and transect approach. Geomorphology 405, 108200. https://doi.org/10.1016/j.geomorph.2022.108200

Lawrence, C., Trulsen, K., Gramstad, O., 2022. Extreme wave statistics of surface elevation and velocity field of gravity waves over a two-dimensional bathymetry. J. Fluid Mech. 939, 1–18. https://doi.org/10.1017/jfm.2022.227

Li, C.Y., Shih, R.S., Weng, W.K., 2020. Investigation of ocean-wave-focusing characteristics induced by a submerged crescent-shaped plate for long-crested waves. Water 12, 1–17. https://doi.org/10.3390/w12020509

Lumley, J.L. 1967. The Structure of Inhomogeneous Turbulent Flows. In: Yaglom, A.M. and Tartarsky, V.I., Eds., Atmospheric Turbulence and Radio Wave Propagation, 166-177.

Lynett, P., Liu, P.L.F., 2004. A two-layer approach to wave modelling. Proc. R. Soc. A Math. Phys. Eng. Sci. 460, 2637–2669. https://doi.org/10.1098/rspa.2004.1305

Mandlier, P.G., Kench, P.S., 2012. Analytical modelling of wave refraction and convergence on coral reef platforms: Implications for island formation and stability. Geomorphology 159–160, 84–92. https://doi.org/10.1016/j.geomorph.2012.03.007

Marshall, R.J.E., Stephenson, W.J., 2011. The morphodynamics of shore platforms in a micro-tidal setting: Interactions between waves and morphology. Mar. Geol. 288, 18–31. https://doi.org/10.1016/j.margeo.2011.06.007

Matsumoto, H., Dickson, M.E., Kench, P.S., 2016a. An exploratory numerical model of rocky shore profile evolution. Geomorphology 268, 98–109. https://doi.org/10.1016/j.geomorph.2016.05.017

Matsumoto, H., Dickson, M.E., Kench, P.S., 2016b. Modelling the Development of Varied Shore Profile Geometry on Rocky Coasts Modelling the Development of Varied Shore Profile Geometry on Rocky Coasts. J. Coast. Res. 75(sp1), 597–601. https://doi.org/10.2112/SI75-120.1

Mendonca, A., Neves, M. G. and Fortes, C. J., 2008. Numerical Study of Hydrodynamics around an artificial surf reef for São Pedro do Estoril, Portugal, SI 56 (Proceedings of the 10th International Coastal Symposium), 1010 – 1014. Lisbon, Portugal, ISSN 0749-0258.

Ogawa, H., Dickson, M.E., Kench, P.S., 2016. Generalised observations of wave characteristics on near-horizontal shore platforms: Synthesis of six case studies from the North Island, New Zealand. N. Z. Geog. 72, 107–121. https://doi.org/10.1111/nzg.12121

Ogawa, H., Dickson, M.E., Kench, P.S., 2015. Hydrodynamic constraints and storm wave characteristics on a sub-horizontal shore platform. Earth Surf. Process. Landforms 40, 65–77. https://doi.org/10.1002/esp.3619

Ogawa, H., Dickson, M.E., Kench, P.S., 2011. Wave transformation on a sub-horizontal shore platform , Tatapouri , North Island , New Zealand. Cont. Shelf Res. 31, 1409–1419. https://doi.org/10.1016/j.csr.2011.05.006

Pequignet, A.-C.N., Becker, J.M.B., Merrifield, M.A.M., 2014. Energy transfer between wind waves and low-frequency oscillations on a fringing reef, Ipan, Guam Anne-Christine. J. Geophys. Res. Ocean. 3868–3882. https://doi.org/10.1002/2014JC010179.Received

Poate, T., Masselink, G., Austin, M.J., Inch, K., Dickson, M., McCall, R., 2020. Infragravity wave generation on shore platforms: Bound long wave versus breakpoint forcing. Geomorphology 350, 1–15. https://doi.org/10.1016/j.geomorph.2019.106880

Priestley, M.B. 1981: Spectral Analysis and Time Series. Academic Press, London.

Ranasinghe, R., Larson, M., & Savioli, J., 2010. Shoreline response to a single shore-parallel submerged breakwater. Coastal Engineering, 57(11–12), 1006–1017. https://doi.org/10.1016/j.coastaleng.2010.06.002

Ranasinghe, R., Turner, I. L., & Symonds, G., 2006. Shoreline response to multi-functional artificial surfing reefs: A numerical and physical modelling study. Coastal Engineering, 53(7), 589–611. https://doi.org/10.1016/j.coastaleng.2005.12.004

Schmidt, O.T., 2020. Bispectral mode decomposition of non-linear flows. Non-linear Dyn. 102, 2479–2501. https://doi.org/10.1007/s11071-020-06037-z

Sheremet, A., Kaihatu, J.M., Su, S.F., Smith, E.R., Smith, J.M., 2011. Modeling of non-linear wave propagation over fringing reefs. Coast. Eng. 58, 1125–1137. https://doi.org/10.1016/j.coastaleng.2011.06.007

Shi, F., Kirby, J.T., Harris, J.C., Geiman, J.D., Grilli, S.T., 2012. A high-order adaptive time-stepping TVD solver for Boussinesq modeling of breaking waves and coastal inundation. Ocean Model. 43–44, 36–51. https://doi.org/10.1016/j.ocemod.2011.12.004

Shi, F., Kirby, J.T., Tehranirad, B., Harris, C.H., Choi, Y., Malej, M., 2016. FUNWAVE-TVD. Fully Non-linear Boussinesq Wave Model with TVD Solver. Documentation and User 's Manual (Version 3.0). Research Report NO. CACR-11-03 CENTER, Center of Applied Coastal Research, University of Delware.

Stephenson, W.J., Kirk, R.M., 2000. Development of shore platforms on Kaikoura Peninsula , South Island , New Zealand Part One : The role of waves. Geomorphology 32, 21–41.

Su, S., Ma, G., Hsu, T., 2021. Numerical modeling of low-frequency waves on a reef island in the South China Sea during typhoon events. Coast. Eng. 169, 103979. https://doi.org/10.1016/j.coastaleng.2021.103979

Su, S. F., Ma, G., & Hsu, T. W., 2015. Boussinesq modeling of spatial variability of infragravity waves on fringing reefs. Ocean Engineering, 101, 78–92. https://doi.org/10.1016/j.oceaneng.2015.04.022

Sunamura, T., 1992. Geomorphology of Rock Coast. John Wiley & Sons, Chichester, 102, 139-183

Tamura, H., Kawaguchi, K., Fujiki, T., 2020. Phase-Coherent Amplification of Ocean Swells Over Submarine Canyons. J. Geophys. Res. Ocean. 125, 1–16. https://doi.org/10.1029/2019jc015301

Thomas, T.J., Dwarakish, G.S., 2015. Numerical Wave Modelling – A Review. Aquat. Procedia 4, 443–448. https://doi.org/10.1016/j.aqpro.2015.02.059

Thompson, C.F., Dickson, M.E., Young, A.P., 2022. Seismic signatures of individual wave impacts on a coastal cliff. Earth Surf. Process. Landforms 1–13. https://doi.org/10.1002/esp.5426

Thompson, C.F., Young, A.P., Dickson, M.E., 2019. Wave impacts on coastal cliffs: Do bigger waves drive greater ground motion? Earth Surf. Process. Landforms 44, 2849–2860. https://doi.org/10.1002/esp.4712

Thornton, E.B., Guza, R.T., 1983. Transformation of Wave Height Distribution. J. Geophys. Res. 88, 5925–5938.

Tonelli, M., Petti, M., 2009. Hybrid finite volume - finite difference scheme for 2DH improved Boussinesq equations. Coast. Eng. 56, 609–620. https://doi.org/10.1016/j.coastaleng.2009.01.001

Trenhaile, A.S., 2000. Modeling the development of wave-cut shore platforms. Mar. Geol. 166, 163–178.

Trenhaile, A.S., 1999. The width of shore platforms in Britain, Canada, and Japan. J. Coast. Res. 15, 355–364.

Trenhaile, A.S., 1987. The Geomorphology of Rock Coasts. Oxford University Press, Oxford, 25, 384.

Tsujimoto, H., 1987. Dynamic conditions for shore platform initiation, Science Report oftheInstituteofGeoscience.

Wei, Z., Dalrymple, R.A., 2017. SPH Modeling of Short-crested Waves, in: Coastal Engineering Proceedings.

Wei, G., Kirby, J.T., Sinha, A., 1999. Generation of waves in Boussinesq models using a source function method. Coast. Eng. 271–299.

Weiland, J., Wihelmsson, H., 1977. Coherent non-linear interaction of wave in plasmas, Pergamon, Oxford

Welch, P.D., 1967. The Use of Fast Fourier Transform for the Estimation of Power Spectra: A Method Based on Time Aver. aging Over Short, Modified Periodograms. IEEE Trans. Audio Electroacoust. AU-15, 70–73.

Winter, G.R.J., Lowe, G., Symonds, J.E.H., Van Dongeren, A.R., 2017. Standing infragravity waves over an alongshore irregular rocky bathymetry. J. Geophys. Res. Ocean. 122, 4868–4885. https://doi.org/10.1002/2016JC012264.Received

Yoon, S.B., Cho, Y.S., Lee, C., 2004. Effects of breaking-induced currents on refraction-diffraction of irregular waves over submerged shoal. Ocean Eng. 31, 633–652. https://doi.org/10.1016/j.oceaneng.2003.07.008

Young, T., 1802. On the Theory of Light and Colours. Philos. Trans. R. Soc. London 12–48.

Zhang, S. J., Zhu, L. S., Zou, K., 2019. A comparative study of numerical models for wave propagation and setup on steep coral reefs. China Ocean Eng., 33(4): 424–435, doi: 10.1007/s13344-019-0040-6

Numerical investigation of the refractive properties of near-horizontal shore platforms and their effects on harmonic and stationary wave patterns

R. Krier-Mariani[1], W. Stephenson[1], S. Wakes[2], M. Dickson[3]

[1] School of Geography, University of Otago, New Zealand

[2] Department of Mathematics and Statistics, University of Otago, New Zealand

[3] School of Environment, University of Auckland, New Zealand

Corresponding author: Raphael, Krier-Mariani (raphael.m.krier@gmail.com; raphael.krier@postgrad.otago.ac.nz)

Key Points:

- Through refraction, concave and convex near-horizontal shore platforms can separate the frequency components of the wavefield.
- Refraction patterns controlled by platform edge convexity affect the dominance of wind, swell and infragravity waves across platforms.
- Coherent amplification from the intersection of refracted infragravity waves controls the nodal state of alongshore stationary waves.

Abstract

Near-horizontal shore platforms display highly irregular plan shapes, but little is known about the way in which these irregularities influence the significant wave height ($\widehat{H_s}$) on the platforms and the frequency components of the nearshore wavefield. We use a non-linear Boussinesq wave model to conduct harmonic and bispectral mode decomposition analyses, studying the control of concave and convex platform edges over wind (WW: 0.125 - 0.33 Hz), swell (SW: 0.05 - 0.125 Hz) and infragravity (IG: 0.008 - 0.05 Hz) frequencies. For breaking and non-breaking waves, increasing the platform edge concavity intensified wave divergence and subsequent attenuation of SW and IG across the outer platforms, reducing $\widehat{H_s}$ by up to 25%. Increasing the platform edge convexity intensified focusing and amplification of SW and WW over the outer platforms, increasing $\widehat{H_s}$ by up to 18% and 55% for breaking and non-breaking waves. In the presence of breaking, IG amplification depended on the generation of wave divergence across the inner platform, a condition determined by a critical convex curvature threshold ($|\mathcal{K}|$=1.8) balancing wave focusing from refraction and defocusing from breaking. We find that convex curvature can determine the relative dominance of WW, SW and IG across platforms. Alongshore, coherent wave interactions governed IG stationary patterns defined by a node near the platform centreline and two antinodes on either side of concave edges. A node was generated at the platform centreline, and two antinodes were observed on either side of the convex edges for $|\mathcal{K}|$>1.8, with the opposite pattern observed for $|\mathcal{K}|$<1.8.

Plain Language Summary

Near-horizontal shore platforms fronting coastal cliffs act as wave energy buffers, regulating wave-induced erosion in rock coast environments. Genuine research endeavours have permitted establishing the link between near-horizontal platform morphology and wave transformation across-shore. However, the effects of alongshore variations in near-horizontal platform morphology on the properties of nearshore wavefields remain sparsely documented. As ocean waves share akin refractive properties to light rays, it can be assumed that, similarly to optical lenses, shore platforms can separate waves according to their frequency depending on their geometry. Subsequently, the convergence and divergence of refracted wave trains of similar phases and frequencies could affect the properties of the nearshore wavefield. The present research investigates this phenomenon over concave and convex edge platforms and its impact on the nearshore wavefield characteristics. Our results show that wave refraction over near-horizontal platforms with concave and convex edges affects the relative dominance of short, medium and long-period waves across shore and results in alongshore stationary wave patterns near the shoreline with nodal states varying in relation to platform edge geometry. Such patterns likely result in alongshore variations in wave erosion and the generation of wave-generated currents shaping rock coasts in the planform.

1 Introduction

Near-horizontal shore platforms, defined by a low gradient ($tan\beta < 0.0175$) and a steep seaward edge, are prevailing coastal landforms in rock coast environments (Sunamura, 1992; Trenhaile, 1999). These landforms have an essential role in wave transformation processes, regulating wave erosive forces at the shoreline (Stephenson and Kirk, 2000; Matsumoto et al., 2016a,b). Thus, an accurate description of the geomorphic control exerted by shore platforms on nearshore wave transformation patterns is necessary for improving rock coast geomorphological models.

Studies have investigated the control of near-horizontal shore platform morphology on the cross-shore evolution of the wavefield (e.g. Beetham and Kench, 2011; Marshall and Stephenson, 2011; Ogawa et al., 2016). Wave breaking induced by the sharp depth transition at the seaward edge of a platform results in the dissipation of incident swell waves (SW: 0.05 Hz < f < 0.125 Hz) and the generation of low-frequency infragravity waves (IG: f < 0.05 Hz) over the platform (Poate et al., 2020). Across the platform surface, IG gradually amplify due to shoaling and energy is transferred from high to lower frequencies, becoming the dominant frequency component over the inner platform (Beetham and Kench, 2011; Marshall and Stephenson, 2011; Ogawa et al., 2011). Wind waves (WW: 0.125 < f < 0.33 Hz) can propagate onto platforms from offshore and, in some cases, be locally generated over the outer platform to become the dominant frequency component in this area (Marshall and Stephenson, 2011; Ogawa et al., 2011). These observations were summarised in the conceptual model of Ogawa et al. (2011), indicating that it is common for the outer platform, platform centre, and inner platform to be dominated by WW, SW and IG, respectively. Ogawa et al. (2011) suggested that these zones shift across-shore with tidal elevation and showed that the relative submergence of shore platforms (depth at the seaward edge/incident wave height) is a critical factor controlling the relative dominance of SW and IG. Collectively, understanding the behaviour of each frequency band of the wavefield helps to depict the variation of significant wave height (H_s) across platforms affecting erosion of the platform and cliff (Trenhaile, 2000). However, the impact of shore platform morphology on two-dimensional wave transformation processes and effect on the frequency bands composing the wavefield have been overlooked.

Few field studies have considered the impact of the planform morphology of near-horizontal platforms on two-dimensional wave transformation patterns (Krier-Mariani et al. 2022, 2023). Krier-Mariani et al. (2023) showed that directional patterns controlled by irregularities in planform morphology generated localised areas of wave ray convergence and divergence as well as alongshore variations in standing IG patterns, influencing the wave energy distribution over the platform surfaces. Based on these observations, Krier-Mariani et al. (2023) introduced a conceptual model in which concave and convex platform edge geometries would control wave ray convergence and divergence patterns over the platform surface, subsequently affecting the IG energy levels and SW decay rates. However, the influence of platform edge geometry on two-dimensional wave patterns could not be clearly isolated from field observations.

In the absence of detailed field studies on the effects of platform edge geometry on wave transformation characteristics, the literature on morphologically analogous submerged flat structures is useful. Depending on their geometry, submerged flats can separate the frequency components of the wavefield, refracting and reorganising the wave crests of incident waves according to their frequency (Jarry et al., 2011; Griffiths and Porter, 2012; Li et al., 2020). This phenomenon can result in complex refraction patterns specific to each frequency component of the wavefield, leading to the generation of caustic rays (clusters of caustic points generated by wave ray intersection) over submerged surfaces (e.g. Mandlier and Kench, 2012). Patterns of wave ray convergence and divergence induced by refraction over submerged flat structures significantly impact the wavefield characteristics. Wave ray convergence results in a localised enhancement of wave height (e.g. Ito and Tanimoto, 1972; Berkhoff et al., 1982), skewness and kurtosis (Janssen and Herbers, 2009; Jarry et al., 2011; Lawrence et al., 2022) while wave ray divergence has the opposite effects.

Although relatively few studies have considered the impact of submerged flat geometries on the cross-shore evolution of harmonic and subharmonic components of the wavefield, harmonic components amplification has been observed in areas of wave convergence (e.g. Lynett and Liu, 2004; Gouin et al., 2017). According to Li et al. (2020), this phenomenon could be attributed to the non-linear effects of convergence on wave height amplification. As the geometry of submerged flats influences the cross-shore pattern of wave convergence (intensity and location) of each harmonic, it likely also influences the cross-shore patterns of wave harmonics amplification, intrinsically affecting the dominance of different wave frequencies across platforms. This hypothesis as yet to be verified.

It has proven difficult to establish causality between patterns of wave ray intersection, increased nonlinearity and alongshore wave height amplification for random wavefields, notably due to the limitation of wave ray tracking techniques to evaluate complex wave ray crossing patterns in dense constellations of caustics (Ito and Tanimoto, 1972). Another way of approaching this problem involves considering the impact of coherent wave interaction patterns on the amplification of dominant frequency components of the wavefield. Coherent wave interaction refers to the non-linear process occurring at the intersection of waves with similar frequency, waveform and phase. It has been identified as a fundamental non-linear wave amplification process in optics (e.g. Young, 1802), quantum mechanics (e.g., Weiland and Wihelmsson, 1977; Falk, 1979; Inouye et al., 1999; Kozuma et al., 1999) and geoscience (e.g. Harid et al., 2014). There have been few investigations of this process in coastal wave studies, but Dalrymple (1975) demonstrated that this process could result in the formation of alongshore stationary wave patterns in random wavefields and the subsequent formation of nearshore currents. More recently, Tamura et al. (2020) showed that, similar to light refraction through a prism, ocean wave refraction over a submarine canyon could separate waves of a random wavefield according to their frequency and phase, favouring coherent wave interactions. Based on this theoretical grounding, it is hypothesised that by controlling the refraction patterns of individual frequency components of the wavefield, submerged flat (e.g. shore platforms) geometry affects coherent wave amplification over submerged flat surfaces, leading to the generation of alongshore stationary wave patterns for SW and IG.

The impact of shore platform geometry on the behaviour of wave harmonics and stationary wave patterns remains to be evaluated in detail on near-horizontal platform surfaces. However, such a task was proven to be difficult during field observations due to the variable nature of nearshore wavefields and the morphological complexity of shore platforms (e.g. Krier-Mariani et al. 2022, 2023). Therefore, this study adopts a numerical modelling approach to address the question: How do mesoscale variations in platform edge geometry affect the behaviour of wave harmonics and the subsequent wave height distribution across and along platform surfaces?

2 Method

2.1 Model set up

The phase-resolving Boussinesq wave model FUNWAVE_TVD V3.6 (Shi et al., 2012) was used to investigate two-dimensional wave transformation over shore platforms. This model treats wave transformation in the time domain and provides a robust representation of non-linear processes, refraction and diffraction while retaining information on the wave phase (Sheremet et al., 2011; Buckley et al., 2015, Buckley et al., 2018; Thomas and Dwarakish, 2015).

2.1.1 Domain

Idealised three-dimensional near-horizontal platform morphologies were incorporated into a 1274 m (x-axis) to 300 m (y-axis) domain (Fig. 1a). A 0.35 m deep, 250 m wide shallow planar surface was included at the landward extremity to absorb wave energy and minimise resonance. The platforms were defined by a constant gradient of 0.35 degrees, a width of 300 m (at the centreline, y = 150 m) and a 3m high seaward cliff of 45 degrees. The nearshore bathymetry profile was composed of a 480 m subtidal ramp (at the centreline) with a gradient of 0.35 degrees followed by an 8 m deep and 635 m wide flat.

Planform geometry was represented using three generic edge geometries defined as straight, concave and convex. The degree of curvature of the concave ($\mathcal{K} < 0$) and convex ($\mathcal{K} > 0$) edge geometries was derived from the parametric ellipse equation. The semi-major axis (a, along the x-axis) was kept constant (120 m) to avoid modifying the cross-shore profile along the centreline, and various degrees of edge curvature were obtained from 2 m increments along the semi-minor axis (b, along the y-axis) between 50 to 100 m, resulting in 26 cases with edge curvatures ($|\mathcal{K}| = |a/b|$) ranging from 1.2 to 2.4 (Fig. 1b-f). The bathymetry was smooth to reduce noise generated by sharp edges and interpolated to a 2 m grid adopted to ensure model stability following a series of sensitivity analyses, providing a realistic representation of model resolution used in previous research in nearshore areas (e.g. Su et al., 2021).

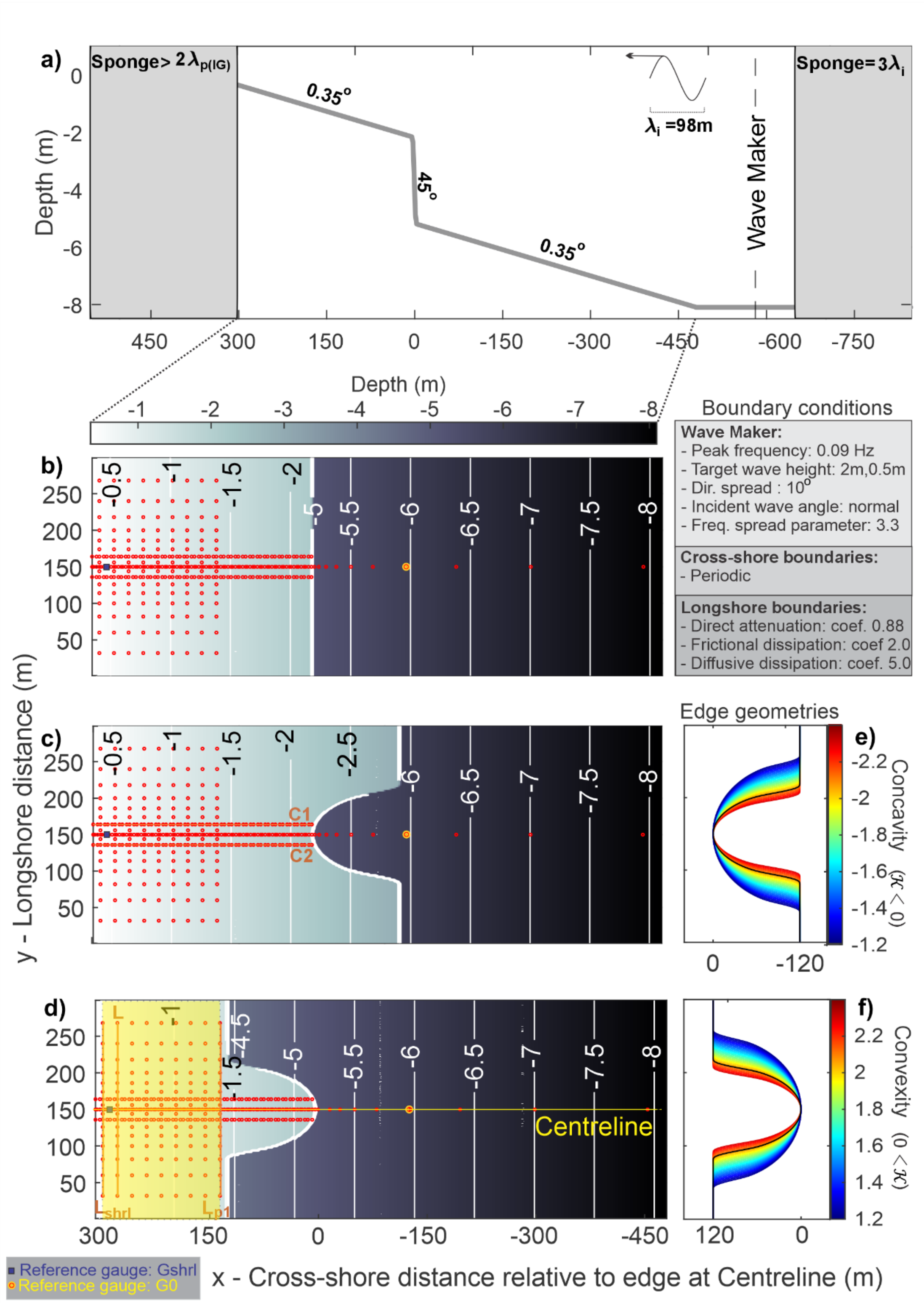

Figure 1: Boussinesq wave model configuration showing the bathymetry profile along the centreline (y = 150m) (a), the model domain for the straight, concave and convex platforms (b-d), and the range of platform edge curvatures considered (e,f). Specifications of the boundary conditions are annotated in the figure. The red dots mark the location of the virtual gauges used for analysis. The yellow shaded area (between L_p and L_{srl}) represents the inner platform section considered for alongshore analysis.

2.1.2 Wave conditions

The model was forced by irregular waves with a directional spread of 10 degrees. An internal wavemaker (Wei et al., 1999) was located on the deep flat at the bottom of the subtidal ramp, five wavelengths (λ_i) away from the platform edge to avoid distortion of the initial wave crests. Irregular waves were generated using a JONSWAP wave spectra (Hasselmann et al., 1973) with a fixed peak enhancement factor of 3.3, a peak frequency (f_p) of 0.09 Hz and direction of 0° (shore-normal) to simplify the visualisation of the refraction effects induced by different planform edge geometries.

Two sets of simulations were generated to investigate the transformation of: (1) waves propagating across the platform surface without breaking (H_s= 0.5 m), as such waves can release large amounts of erosive energy when they break against cliffs (Thompson et al., 2019; Thompson et al., 2022); and (2) wave breaking at the seaward edge (H_s= 2 m) decaying across the platform, which are typically used to define variation of wave erosive force across platforms in geomorphological models (e.g. Trenhaile, 2000; Matsumoto et al., 2016a,b). These two sets of simulations combined with the range of platform concave and convex curvatures resulted in 106 simulations (including straight edge reference cases). The default breaking index of FUNWAVE-TVD (γ_b=0.80) was used to represent wave breaking, providing a close representation of the breaking conditions for steep submerged slopes (Blenkinsopp and Chaplin, 2008). The effects of bottom friction were not considered (i.e. the frictional dissipation coefficient was set to C_d= 0.002, representing a smooth surface).

2.1.3 Boundary conditions

The domain boundary conditions were defined to minimise reflection. Periodic boundaries (Chen et al., 2003) were applied to the northern and southern extremities of the domain, allowing waves to propagate out of the domain. Following Shi et al. (2016), sponge layers employing a direct damping coefficient as well as dissipation by friction and diffusion were used to reduce noise and dampen wave energy at the eastern and western sides of the domain (Fig. 1a). The width of the sponge layer at the shallow western side of the domain was chosen to correspond to twice the peak wavelength of the IG at this location (estimated during trial runs using the virtual gauge G_{shrl} at the shoreline, Fig. 1), to avoid reflection and the subsequent generation of standing IG waves.

2.1.4 Model Validation

Due to the lack of two-dimensional field measurements in similar near-horizontal shore platform settings, no direct validation of our model simulations was carried out. However, a number of studies validated FUNWAVE-TVD against field observations over coral reefs, proving the model's ability to represent wave transformation over smooth submerged flats with sharp seaward edges (e.g. Mendonca et al., 2008; Su et al., 2015; Zhang et al., 2019). As the present study explores wave processes such as refraction and non-linear energy transfer fairly well represented by the model (Griffiths and Porter, 2012; Su et al., 2015) and does not investigate subsequent processes such as wave-driven circulation and sediment transport, it is deemed unnecessary to validate the model with experimental data at this stage (similar inference were made in da Silva et al., 2023).

2.2 Measurements and analysis

To determine the impact of planform geometries on wave transformation across the platforms, the spectral evolutions of waves propagating across concave and convex platforms (affected by two-dimensional transformation processes) were compared to the spectral evolution of waves propagating across the straight-edge platform (only affected by on-dimensional transformation processes). This approach permitted the identification of spectral anomalies representing the energy variations for specific harmonics induced by refraction. Positive and negative anomalies indicate harmonic amplifications and attenuation, respectively. Combined, the harmonic anomalies result in anomalies of significant wave height across platforms ($\Delta\widehat{H_s}$). Following Baldock et al. (2020), the cross-shore patterns of $\Delta\widehat{H_s}$ were then compared to the directional patterns along the platform centrelines to identify the effects of refraction patterns controlled by platform edge geometry on significant wave height distribution across platforms.

In the alongshore, the effects of coherent wave interaction induced by refraction over concave and concave platforms on the generation of stationary wave patterns were considered. For this purpose, the bispectrum (Hasselmann et al., 1963) provides a convenient representation of the wavefield as it holds information on the wave phase, frequency and power necessary to detect phase coupling. The bispectrum, defined from the third moment of the free surface elevation time series, also represents a measure of skewness, which increases in areas of wave ray intersection (Janssen and Herbers, 2009; Jarry et al., 2011; Lawrence et al., 2022). Following Kim and Powers (1979), who investigated the impact of coherent interactions of random electromagnetic waves on plasma density fluctuation using bispectral properties, the frequency, phase and power information yielded by the bispectrum were used to identify patterns of coherent wave interactions over the inner platforms. A modal decomposition method based on bispectral properties (Appendix 2), the Bispectral Mode Decomposition or BMD (Schmidt, 2020), was employed to identify the modal state of coherent structures for self-interacting harmonic components within the SW and IG frequency bands. The areas of coherent wave interactions were then compared to the wave height distribution of SW and IG over platforms of various geometries to identify patterns of coherent wave amplification.

2.2.1 Wave measurements

Wave records were obtained from virtual gauges recording surface elevation (η) as well as u and v velocity components at 2 Hz (Fig. 1b-d). In the cross-shore direction, the gauge spacing along the centreline increased seaward from the platform edge (increment based on geometric series starting with a spacing of 4 m with an increment factor of 1.5). On the platforms, the gauge spacing was irregular but not exceeding 6 m along the centreline, transects C_1 and C_2. The distance between the gauges composing the alongshore transects (between L_0 and L_{shrl}) increased on either side of the centreline from 6 to 30 m (with an increment factor of 1.25). Statistical analyses of the wavefield properties were based on an observation window of 2048 seconds, starting 230 seconds after the start of the simulations, marking the time at which SW reached the landward extremity of the domain and IG were generated.

2.2.2 Definition of wave height

The significant wave height (H_s) was defined from the spectra moment (e.g. Thornton and Guza, 1983):

$$H_s = 4\sqrt{\int_{fmin}^{fmax} S(f).df} \tag{1}$$

The wave spectra estimates $S(f)$ were generated using the Welch (1967) method with segment lengths of 512 samples, 50% overlap and a Hanning window resulting in 20 Degrees of Freedom (Priestley, 1981). To provide a more detailed representation of the wavefield, the gravity and infragravity waves were further divided into two frequency bands, encapsulating the dominant harmonics observed within the WW, SW, and IG (high and low) frequency ranges across the domain (Table 1). The wave height associated with each of these frequency bands was determined using:

$$H_{f_{np}} = 4\sqrt{\int_{flow}^{fhigh} S(f).df} \tag{2}$$

where n denotes the rank of the harmonic, f_{low} and f_{high} represents the lower and higher frequencies of the power spectral density peak associated with this harmonic, Table 1. The reference incident wave height (H_0) was defined from measurements taken at the gauge G_0 located at the top of the subtidal ramp (Fig. 1) and was used to normalise the wave height on the platform surface ($\widehat{H_s}(x) = H_s(x)/H_0$, $\widehat{H_{fnp}}(s) = H_{fnps}(x)/H_0$). For simplicity, normalised wave heights are hereafter referred to as wave heights.

Table 1 Frequency band analysis parameters

Conventional Frequency class	Frequency subclass	Corresponding Harmonic	Frequency (f_{np})	Frequency range ($f_{low} - f_{high}$)
Gravity waves	Wind waves (WW)	Second harmonic	f_{2p}	0.15 – 0.20 Hz
	Swell waves (SW)	Principal harmonic	f_p	0.06 – 0.12 Hz
Infragravity waves	Infragravity High (IG_H)	Second subharmonic	$f_{1/2p}$	0.04 – 0.05 Hz
	Infragravity Low* (IG_L)	Fifth subharmonic	$f_{1/5p}$	0.008 – 0.03 Hz

*Note that the typical cutoff frequency for the lower portion of the IG frequency band is 0.005 Hz (e.g. Pequignet et al., 2014; Gawehn et al., 2016). However, the chosen cutoff frequency of 0.008 Hz is more appropriate to describe the low IG in the simulated wavefield as it corresponds to a trough in the power spectra estimate across the entire domain, which provides a better physical representation of the low IG.

2.2.3 Definition of peak direction

The angle α between the peak direction of waves propagating on either side of the centreline (along the cross-shore transects C1 and C2, Fig. 1) was used to investigate the evolution of wave convergence and divergence along the platform centrelines. The peak direction of waves over the platform was estimated from the directional wave spectra $S(f,\theta) = S(f)G(\theta|f)$ calculated from the free surface elevation (η) and velocity components (u and v) time series by applying the Extension of the Maximum Entropy Principle (EMEP) method (Hashimoto et al., 1994). To this effect, segments of 512 samples were used to estimate the frequency spectra ($S(f)$) and 200 iterations to define the approximation of the spreading function ($G(\theta|f)$) resulting in 76 frequency bins and directional bins of 5°.

2.2.4 Identification of coherent wave interaction patterns

The BMD was applied to the free surface elevation time series recorded by the two-dimensional virtual gauge array between L_p and L_{shrl}, marking the boundaries of the spatial domain ξ (Fig. 1). The welch periodograms employed in the BMD were computed using segments of 512 samples, 50% overlap and a Hanning window resulting in 20 Degrees of Freedom. Patterns of coherent wave interactions were identified from coherent self-interaction maps ($\psi_{k,k}$) which are defined by the product of cross-frequency fields $\phi_{k\circ k}$ and the bispectral modes ϕ_{k+k} obtained from the BMD:

$$\psi_{k,k}(\xi, f_k, f_k) = |\phi_{k\circ k} \circ \phi_{k+k}| \quad (3)$$

where the frequency k considered were f_p and $f_{1/5p}$, representing the dominant harmonics in the SW and IG frequency bands. The cross-frequency fields $\phi_{k\circ k}$ are maps of phase alignment for these frequencies, while bispectral modes ϕ_{k+k} represent the amplitude of oscillations of the sea surface at frequency $2k$. Conventionally, the largest values of the normalised coherent self-interaction maps $\widehat{\psi_{k,k}}$ indicate areas where phase coupling has the strongest effect on wave amplitude for the sum frequency $2k$. The interaction maps for straight wave crests with parallel wave rays are expected to be homogeneous alongshore. In contrast, for cases where wave crests are bent and wave rays intersect, interaction maps will be non-homogenous alongshore and display maxima in areas of wave ray intersection. In the presence of coherent wave amplification, maxima in coherent self-interaction maps correspond to areas of wave height amplification at frequency k.

3 Results

3.1 Impact of planform geometry on across-shore wave transformation

3.1.1 Non-breaking waves (H_0 = 0.5 m)

The spatial evolution of the spectral properties of non-breaking waves propagating across the domain was examined for the three types of platform geometries (Fig. 2), for which the power spectra density was concentrated around four distinctive frequency components (Fig. 2a): the second and the principal harmonics (f_{2p} and f_p) within the WW and SW frequency bands; and the second and fifth subharmonics ($f_{1/2p}$ and $f_{1/5p}$) within the IG_H and IG_L frequency bands.

The spectral anomalies observed over the concave platforms indicated an attenuation of the principal harmonic (Fig. 2b-e). This phenomenon intensified with increasing degrees of curvature (with minimum spectral anomalies at peak frequency reducing from -0.09 m^2 Hz^{-1}

at $|\mathcal{K}|$= 1.2 to -0.41m^2 Hz^{-1} at $|\mathcal{K}|$= 2.4). In contrast, an amplification of the second and principal harmonics was observed across convex platforms (Fig. 2g-j), intensifying with increasing edge curvature (with maximum spectral anomalies at peak frequency increasing from 0.52 m^2 Hz^{-1} at $\mathcal{K}$= 1.2 to 1.37 m^2 Hz^{-1} at $\mathcal{K}$= 2.4).

The variation of spectral characteristics of each harmonic over the concave and convex platforms can be expressed in terms of mean wave height anomalies ($\overline{\Delta H_{fnp}}$). The most significant impacts of platform curvature on mean wave height anomalies were observed within the WW and SW frequency bands. The mean wave height anomalies associated with the second and the principal harmonics displayed a very strong linear dependency ($R^2 > 0.9$) to the degree of platform edge curvature (Fig. 2f,k). The increase of curvature form $|\mathcal{K}|$= 1.2 to 2.4 promoted the attenuation of harmonics within the WW and SW frequency bands across concave platforms and the amplification of these waves across convex platforms. The attenuation of the second and principal harmonics across concave platforms of high curvature $|\mathcal{K}|$= 2.4 corresponded to 9% and 15% of H_0. Across convex platforms of high curvature, $|\mathcal{K}|$= 2.4, the amplification of the second and principal harmonics reached up to 11% and 29% of H_0. The mean wave height anomalies for the subharmonic in the IG_H and IG_L frequency bands were negligible for nonbreaking waves.

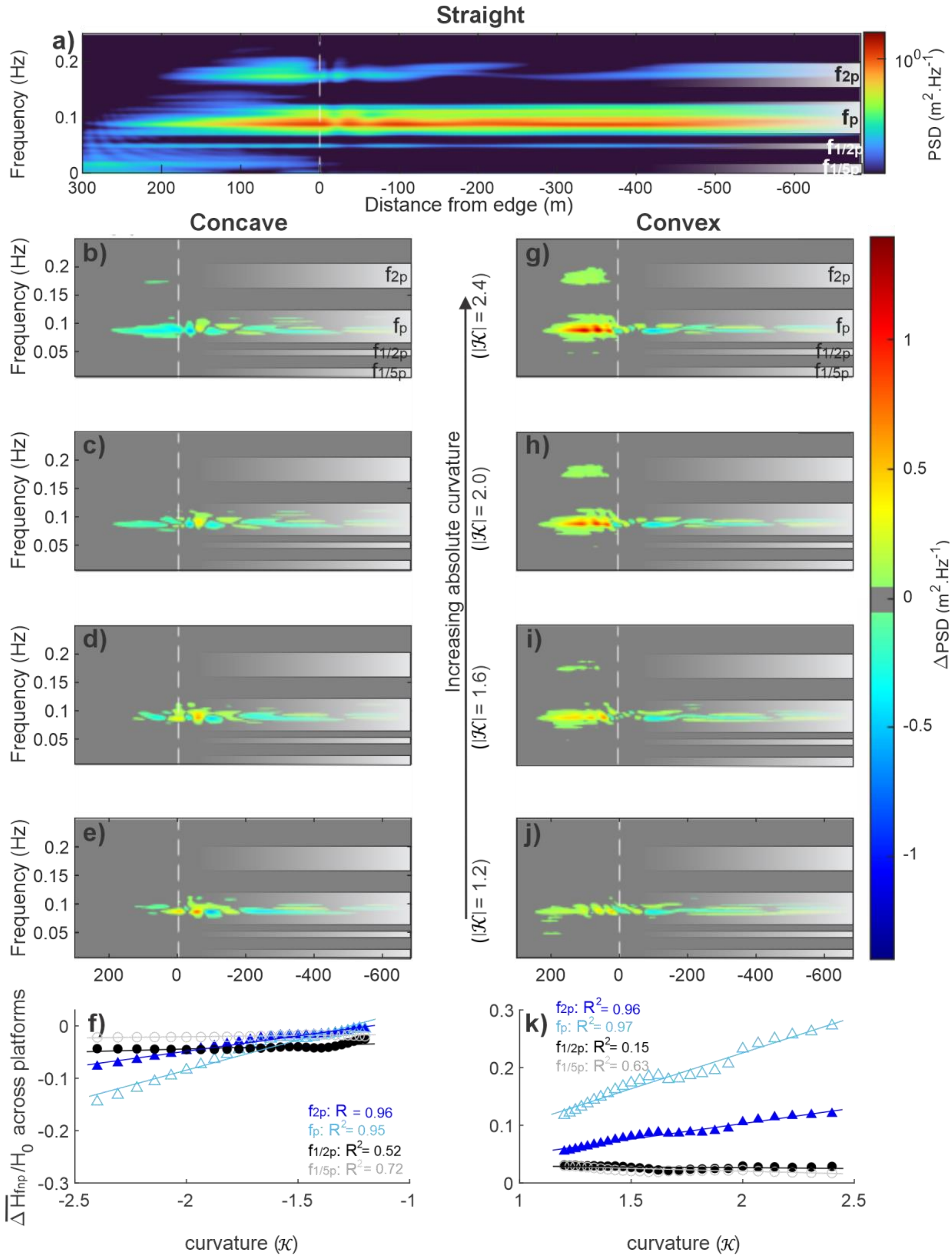

Figure 2: Impact of platform edge curvature on the harmonic components of the wavefield for non-breaking waves showing: the spectral anomalies in relation to the straight edge platform (a) for concave platform geometries (b-e) and convex platform geometries (g-j); and the impact of curvature on the mean wave height of each harmonic across the concave (f) and convex (k) platforms.

$\Delta\widehat{H_s}$ across the platform can be assumed to be impacted by refraction patterns controlled by platform geometry. To explore this process, directional patterns and $\Delta\widehat{H_s}$ across the centrelines of each platform were compared for various edge curvatures. The cross-shore patterns of $\Delta\widehat{H_s}$ presented in Fig. 3a,b were modulated by the platform edge curvature, with magnitude increasing with curvature for both types of platform geometries. As a result, for high degrees of curvature ($|\mathcal{K}|$ = 2.4), the negative anomalies across the concave platforms indicated a maximum of 25% attenuation in significant wave height (Fig. 3a), while the positive anomalies across the convex platforms (Fig. 3b) indicated a 55% amplification of significant wave height. The location of the largest $\Delta\widehat{H_s}$ shifted across platforms in relation to curvature. For concave platforms, the largest negative $\Delta\widehat{H_s}$ over the outer platform shifted landward with decreasing curvature from $|\mathcal{K}|$ = 2.4 to 1.9. Similarly, the largest positive $\Delta\widehat{H_s}$ across the convex platforms shifted landward, reaching the inner platform for $|\mathcal{K}|$ < 1.6. For low degrees of concave curvatures ($|\mathcal{K}|$ < 1.9), corresponding to curvatures for which amplification of wave energy seaward of the platform edge was observed (Fig. 2b-e), wave transformation patterns across the platform centreline were affected by the preconditioning of incident waves occurring off the platform edge. Therefore, the description of the following results focuses on concave edge curvatures, $|\mathcal{K}| >$1.9.

Similarly to the cross-shore evolution of $\Delta\widehat{H_s}$, the peak magnitude of wave ray divergence observed across concave platforms and convergence across the convex platforms decreased and shifted landward from the mid-platform ($x \approx 150\ m$) to the outer platform with decreasing curvature (Fig. 3c,d). A Spearman rank correlation (Fig. 3e,f) revealed that the dependency of cross-shore $\Delta\widehat{H_s}$ on the directional patterns observed over the concave platforms was only relevant (moderate to strong, ρ_s > 0.4) for platform edge curvatures exceeding 1.9. In contrast, a strong relationship (ρ_s > 0.6) as observed between wave height anomaly and directional patterns over convex platforms for the majority of platform edge curvatures, indicating that $\Delta\widehat{H_s}$ across the convex platforms were predominantly controlled by the wave convergence and divergence across the centreline.

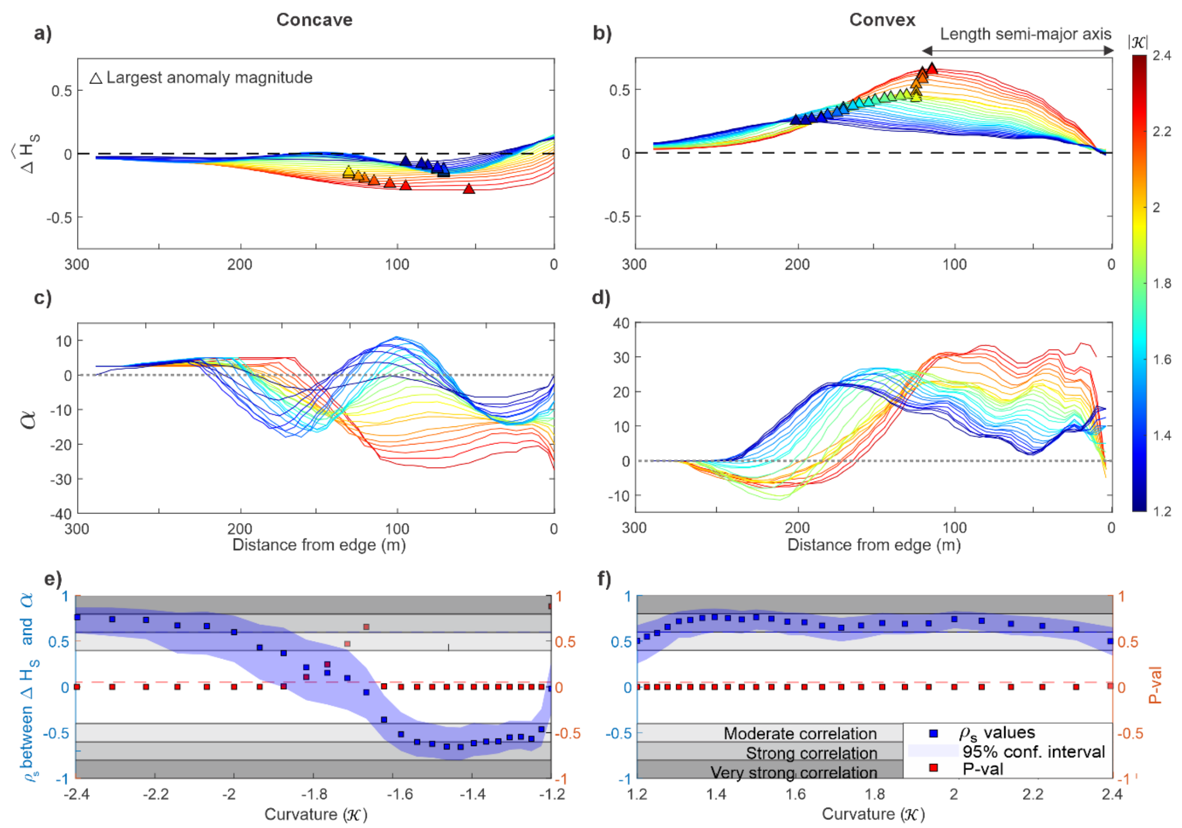

Figure 3: Relationship between directional patterns and significant wave height anomalies of non-breaking waves across concave (left) and convex platforms (right) at the centreline (y =150 m) for different degrees of curvature showing: the significant wave height anomalies (a,b) and the cross-shore directional patterns (c,d). The impact of directional pattern on wave anomaly pattern was assessed using a spearman correlation between the two parameters (e,f).

3.1.2 Broken waves (H_0 = 2.0 m)

The spectral evolution of broken waves across concave platforms displayed a complex pattern of spectral anomalies (Fig. 4b-e), with a clear amplification of the principal harmonic corresponding to SW over the outer platform for degrees of curvature below 1.9 (at f_p, positive anomalies reached 1.5 m^2 Hz^{-1} at $\mathcal{K}$= 2.0 and 2.4, 0 to 150 m from the edge) and a clear attenuation of this harmonic for degrees of curvature exceeding 1.9 (at f_p, negative spectral anomaly reached -1.2 m^2 Hz^{-1} at $\mathcal{K}$= 1.2 and 1.6, 0 to 150 m from the edge). These differences were related to the amplification of the principal harmonic for edge curvatures below 1.9, displaying anomalies reaching up to ~12 m^2 Hz^{-1} in the vicinity of the concave edge sections (0 to -120 m from the edge) before reaching the platform surface (Fig. 4d,e). Over convex platforms, the principal harmonic presented the largest amplification (Fig. 4g-j), which intensified over the outer platform with increasing curvature (positive anomaly at f_p reached 2.1 m^2 Hz^{-1} at $\mathcal{K}$= 1.2 and 4.1 m^2 Hz^{-1} at $\mathcal{K}$= 2.4, 0 to 150 m from edge). In contrast, the amplification of subharmonics within the IG_H and IG_L frequency bands toward the shoreline observed along the platform centreline was stronger for low convex edge curvatures than for high convex edge curvatures (positive anomaly at $f_{1/5p}$ reached 0.7 m^2 Hz^{-1} at $\mathcal{K}$= 1.2 and 0.5 m^2 Hz^{-1} at $\mathcal{K}$= 2.4, 150 to 300 m from edge).

Relationships between edge curvature and mean wave height anomalies across both platform types were observed (Fig. 4f,k). For anomalies in the WW and SW frequencies, the mean wave height anomalies of the second and the principal harmonics presented a strong linear dependence on the degree of edge curvature of concave and convex edges (R^2 > 0.90). In the IG_H frequency band, mean wave height anomalies associated with the second subharmonic were linearly dependent on the curvature across concave platforms (R^2 = 0.67). The mean wave height anomalies associated with the fifth subharmonic in the IG_L frequency band decreased linearly (R^2 = 0.94) with curvature over the convex platforms.

Variations in edge curvature affected the relative importance of WW, SW, IG_H and IG_L anomalies across the platforms. For concave platforms, the increase of concave edge curvature promoted attenuation of all frequency bands, but particularly for WW and SW. For the harmonic components within the WW and SW frequency bands, the mean wave height attenuation across concave platforms was negligible for low curvature ($\overline{\Delta H_{f_{2p}}}$ and $\overline{\Delta H_{f_p}}$ and representing less than 1% of H_0 at $|\mathcal{K}|$=1.2) but intensified for high degrees of curvature ($\overline{\Delta H_{f_{2p}}}$ and $\overline{\Delta H_{f_p}}$ representing less than 3% and 6% of H_0 at $|\mathcal{K}|$=2.4). Across the convex platforms of low curvature (1.2 < $|\mathcal{K}|$ < 1.75), the largest amplification of mean wave height was observed for the principal harmonic ($\overline{\Delta H_{f_p}}$ representing 4% to 7% of H_0), followed by the fifth subharmonic ($\overline{\Delta H_{f1/5_p}}$ representing 3% to 3.5% of H_0). The amplification of the fifth subharmonic became less important with increasing curvature, while the mean wave height of the second harmonic was amplified. For convex curvatures exceeding 1.75, the principal harmonic displayed the largest amplification ($\overline{\Delta H_{f_p}}$ representing 7% to 10% of H_0), followed by the second harmonic ($\overline{\Delta H_{f_{2p}}}$ representing 3% to 4% of H_0). Thus, the reduction of convex edge curvature promoted the amplification of IG_L, while the increase of convex edge curvature promoted the amplification of WW and SW.

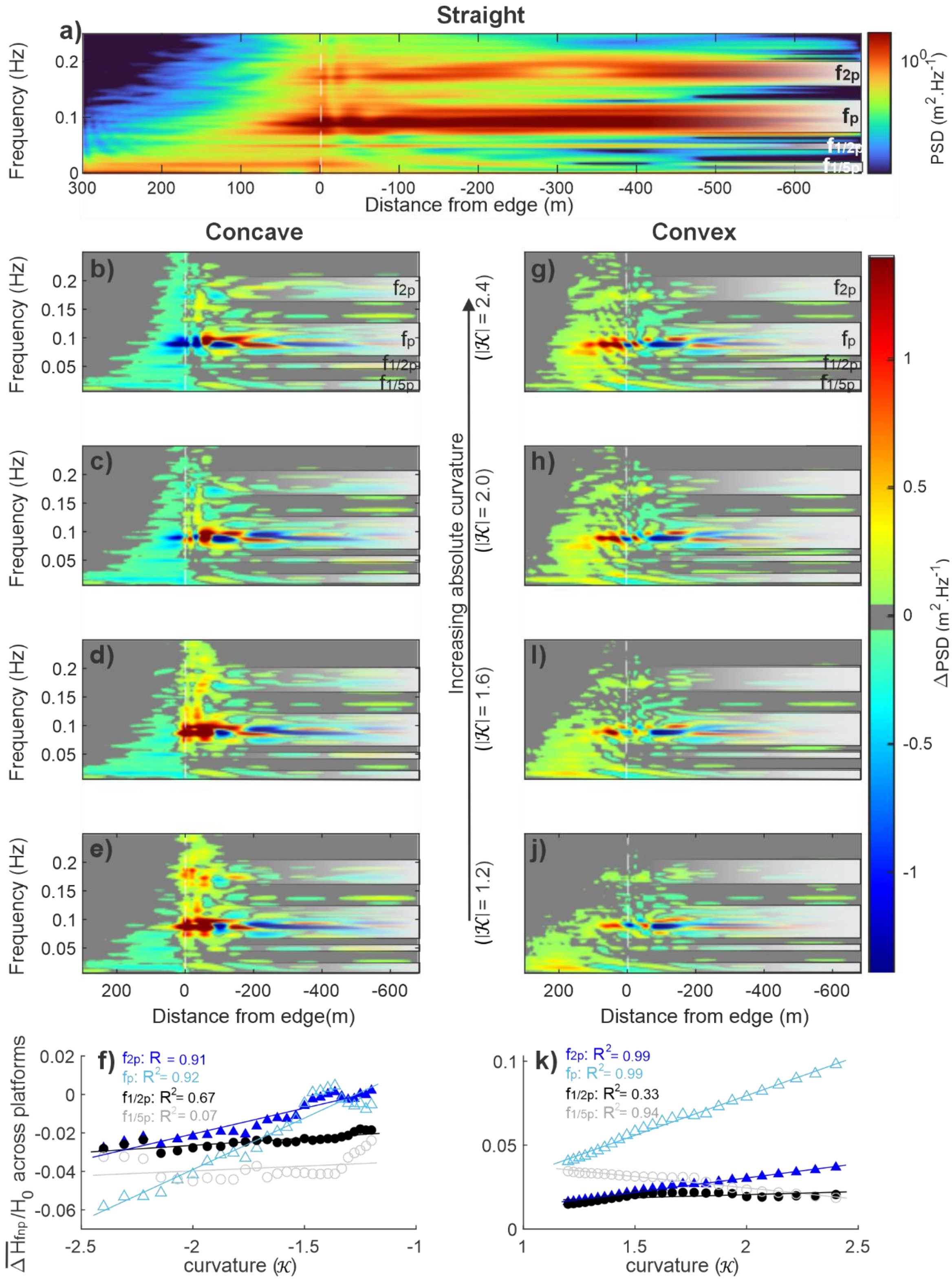

Figure 4: Impact of platform edge curvature on the harmonic components of the wavefield for broken waves showing: the spectral anomalies in relation to the straight edge platform (a) for concave platform geometries (b-e) and convex platform geometries (g-j); and the impact of curvature on the mean wave height of each harmonic across the concave (f) and convex (k) platforms.

The relationship between $\Delta\widehat{H_s}$ (Fig. 5a,b) and directional patterns (Fig. 5c,d) observed across the concave and convex platform centrelines was more complex for broken than non-breaking waves. The main difference with the non-breaking waves resided in the seaward shift of the maximum divergence (Fig. 5c) and convergence (Fig.5d) locations over the outer concave and convex platforms, respectively. This shift was particularly pronounced for convex shore platforms with low degrees of curvature ($|\mathcal{K}| < 1.8$), for which the peaks of convergence observed mid-platform ($x \approx 175$ m, Fig. 3d) were attenuated.

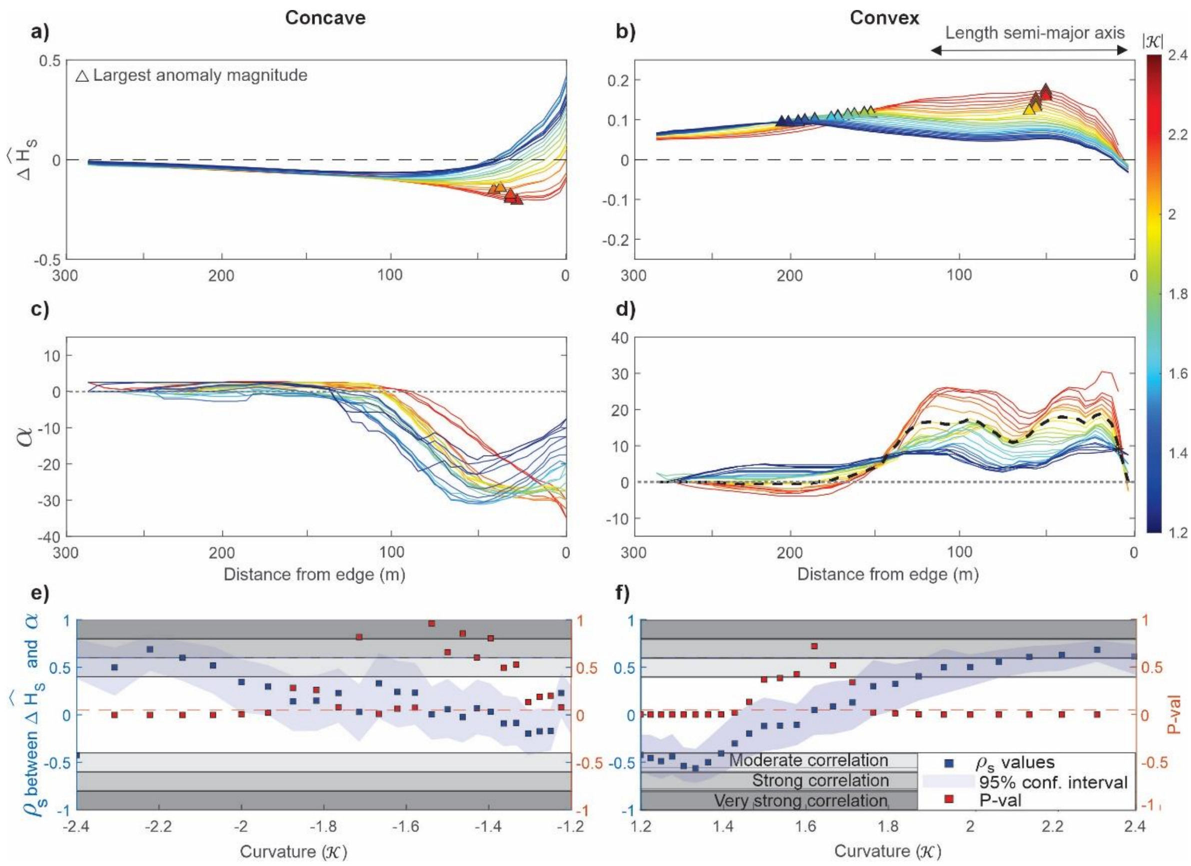

Figure 5: Relationship between directional patterns and significant wave height anomalies of broken waves across concave (left) and convex platforms (right) at the centreline (y = 150 m) showing: the significant wave height anomalies (a,b), the cross-shore directional patterns (c,d) and spearman correlation between these two parameters (e,f).

For concave platforms, the seaward shift of maximum divergence zones coincided with a seaward shift of the location of the largest negative anomalies (representing a 25% attenuation in $\widehat{H_s}$, Fig. 5a). As a result, the relationship between $\Delta\widehat{H_s}$ and directional patterns of broken waves remained moderate to strong (0.4 < ρ_s< 0.6) for concave edge curvatures exceeding 1.9 (Fig. 5e), indicating that for large degrees of edge curvature, the $\Delta\widehat{H_s}$ observed across the concave platform depended on the directional patterns along the centreline. For convex platforms, the seaward shift of the maximum convergence locations (Fig. 5d) coincided with a seaward shift of the largest positive anomalies for curvatures over 1.8 (representing an 18% amplification in $\widehat{H_s}$, Fig. 5b). However, for curvatures lower than 1.8, the maximum anomalies shifted landward. Thus, the correlations between $\Delta\widehat{H_s}$ and directional patterns across the centreline were moderate to strong (0.4 < ρ_s< 0.6) for convex edge curvatures exceeding 1.8, and weak (ρ_s < 0.4) for curvatures dropping below 1.8 (Fig. 5f). This phenomenon can be explained by analysing the relative influence of each harmonic component on $\Delta\widehat{H_s}$ observed across the platforms (Fig. 6).

For convex curvatures exceeding 1.8, the decrease of wave convergence over the outer platform and wave ray divergence over the inner platforms (Fig. 5c) coincided with a reduction of wave height anomalies for all harmonic components over the inner platform (Fig. 6). This reduction was particularly important for the fifth subharmonic, $\Delta\widehat{H_{f_{1/5p}}}$, representing 5% of the observed amplification of significant wave height at $x = 190$ m against 10% at $x = 130$ m for $|\mathcal{K}|$=2.4. In contrast, convex edge curvature below 1.8 inhibited the formation of a divergence zone, ensuring the sustainability of wave ray convergence across the entire platform. Under these conditions, the wave height anomalies within the WW and SW frequency bands were sustained across the entire platform, and anomalies within the IG_L frequency band were amplified over the inner platform ($\Delta\widehat{H_{f_{1/5p}}}$ representing 15% of the observed amplification of normalised significant wave height at $x = 190$ m for $|\mathcal{K}|$=1.2) to become the dominant type of anomaly at this location. Thus, $\Delta\widehat{H_s}$ became predominantly controlled by the behaviour of IG_L as curvature decreased (1.4 < $\mathcal{K}$ < 1.8). For very low degrees of curvature ($\mathcal{K}$ < 1.4), the amplification of IG_L was of such importance that $\Delta\widehat{H_s}$ were amplified over the inner platform despite the decrease in wave convergence, resulting in a negative correlation (- 0.6 < ρ_s< - 0.4) between $\Delta\widehat{H_s}$ and directional patterns (Fig. 5c).

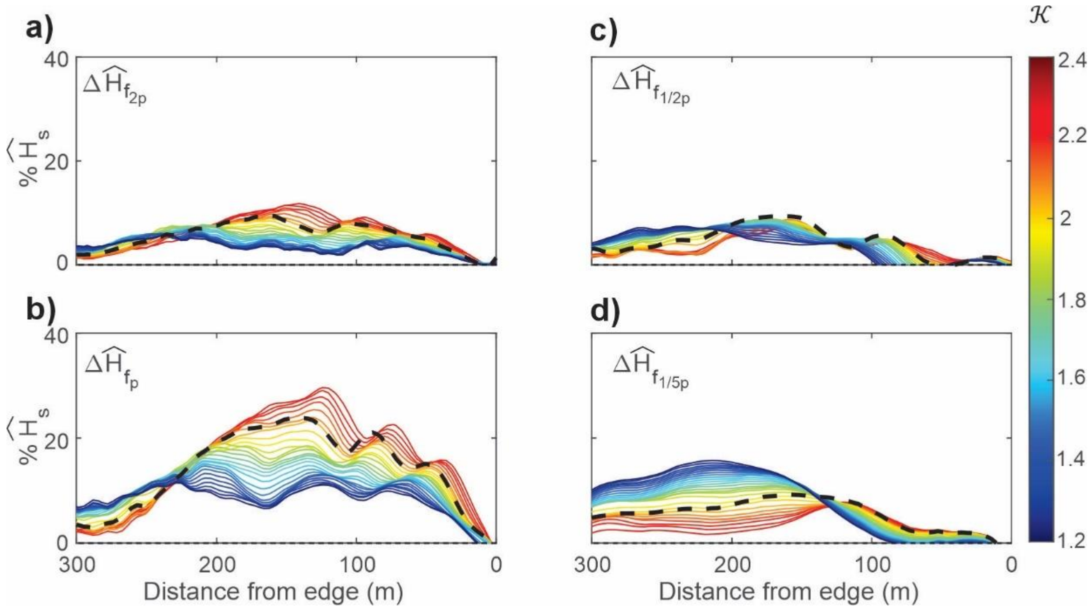

Figure 6: Percentage of significant wave height variations across the centreline (y = 150 m) convex platforms associated with anomalies of the second higher harmonics (a), the principal harmonic (b), the second subharmonic (c) and the fifth subharmonic (d) components (H_s=$H_{s_{Straight}} + \Delta H_s$). The dashed line represents a curvature of 1.8, marking the threshold for the formation of a divergence zone over the inner platforms.

3.2 Effects of platform edge geometry on alongshore wave height patterns

3.2.1 Non-breaking waves

Coherent self-interaction maps were plotted to investigate the impact of platform edge geometry on alongshore wave height variation over the inner platform for non-breaking waves (Fig. 7). Maxima in these maps ($\hat{\psi} \approx 1$) correspond to areas of strongest coherent interaction for the dominant frequency components within the SW and IG_L frequency bands (f_p and $f_{1/5p}$). Over the concave platforms, zones of coherent self-interaction for the principal harmonic (f_p) shifted alongshore from the platform centrelines to become concentrated near the northern and southern extremities of the platform as the edge curvature increased (Fig. 7a-d). These alongshore variations were predominantly observed between x = 130 and 175 m, where divergence along the centreline was the strongest (Fig. 3c). In contrast, coherent self-interaction maps for the fifth subharmonic ($f_{1/5p}$) were more homogenous alongshore (Fig. 7e-h), except near the shoreline, where coherent self-interactions were predominantly observed at the platform centreline. Over the convex platform, coherent self-interactions of the principal harmonic (Fig. 7i-l) were concentrated toward the platform centreline for edge curvatures between $|\mathcal{K}|$=1.2 to 1.6 (Fig. 7k,l), but as edge curvature increased, coherent wave interaction for this harmonic predominantly occurred at the northern and southern extremities of the platforms (Fig. 7i,j). For the fifth subharmonic, coherent self-interactions were focussed near the platform centreline for low edge curvature and spread alongshore toward the shoreline $|\mathcal{K}|$=1.2 (Fig. 7p). As curvature increased, the areas of fifth subharmonic coherent self-interactions near the shoreline split into two peaks on either side of the platform centreline (Fig. 7m,n). This phenomenon was observed at curvatures for which a mild divergence was observed over the inner platform (Fig. 3d).

The wave height distribution over the inner sections of concave and convex platforms is shown in Fig. 8 and 9. The spatial distribution of the significant wave height ($\widehat{H_s}$) presented the strongest similitudes ($R^2 > 0.9$) with the wave height patterns of the principal harmonic ($\widehat{H_{f_p}}$) regardless of the platform geometry and curvature. This Indicates a strong control of SW on the patterns of significant wave height variations over the inner platform. In contrast, the correlation between the wave height patterns of the fifth subharmonic and the significant wave height patterns over the inner platforms of concave and convex geometries was weak ($R^2 < 0.4$), indicating that IG_L had little impact on the variations of significant wave height at this location.

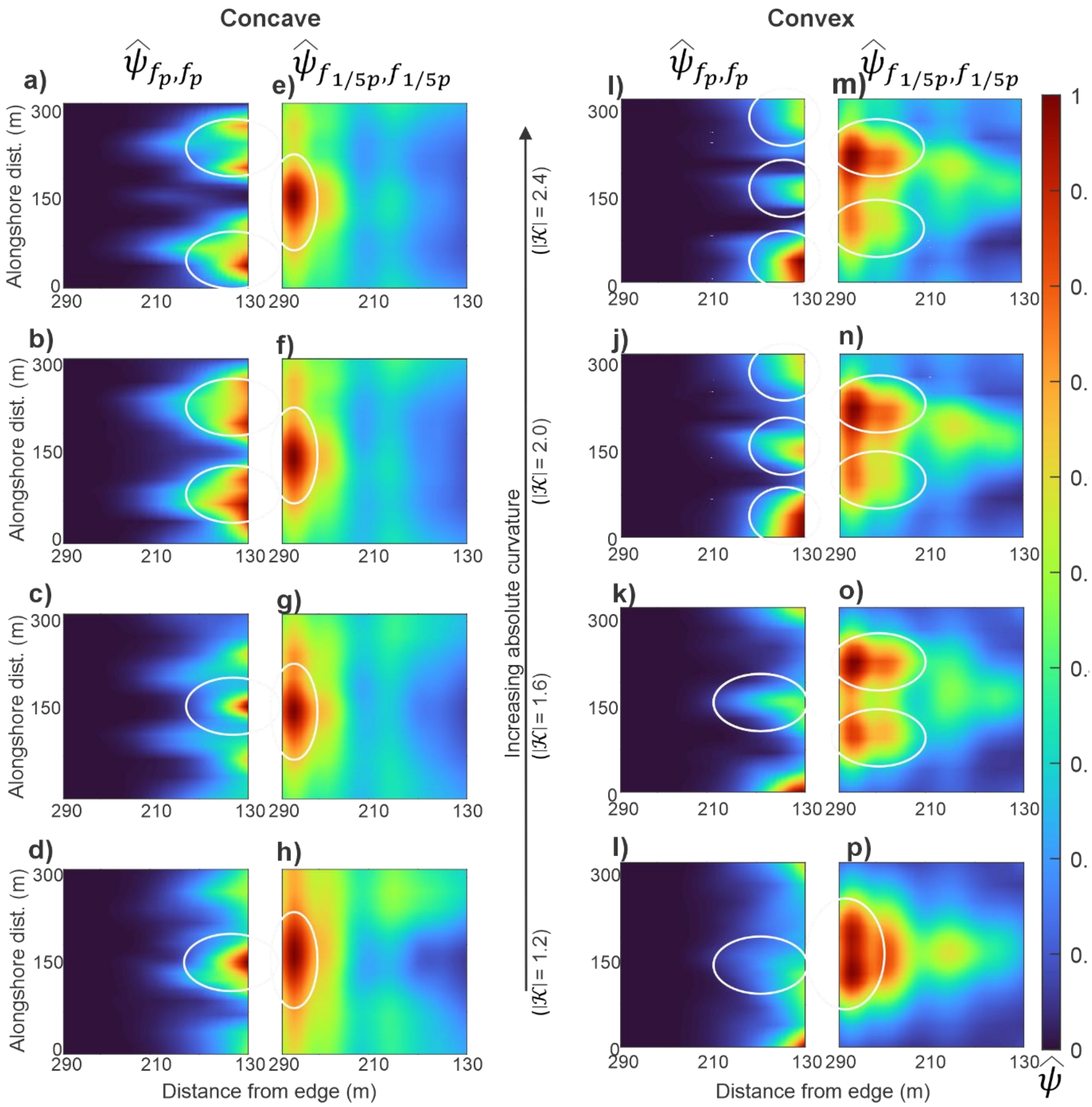

Figure 7: Coherent self-interaction maps defined from the bispectral modal state of self-interacting components for the principal harmonic (f_p) and the fifth subharmonic ($f_{1/5p}$) of non-breaking waves over the inner platform (Fig. 1) at different concave (a-h) and convex (i-p) edge curvatures. The centreline is located at y =150 m. Values of $\widehat{\psi}$ of 1 indicate areas of the largest coherent wave interactions. The white ellipses highlight the zones of strong coherent wave interactions.

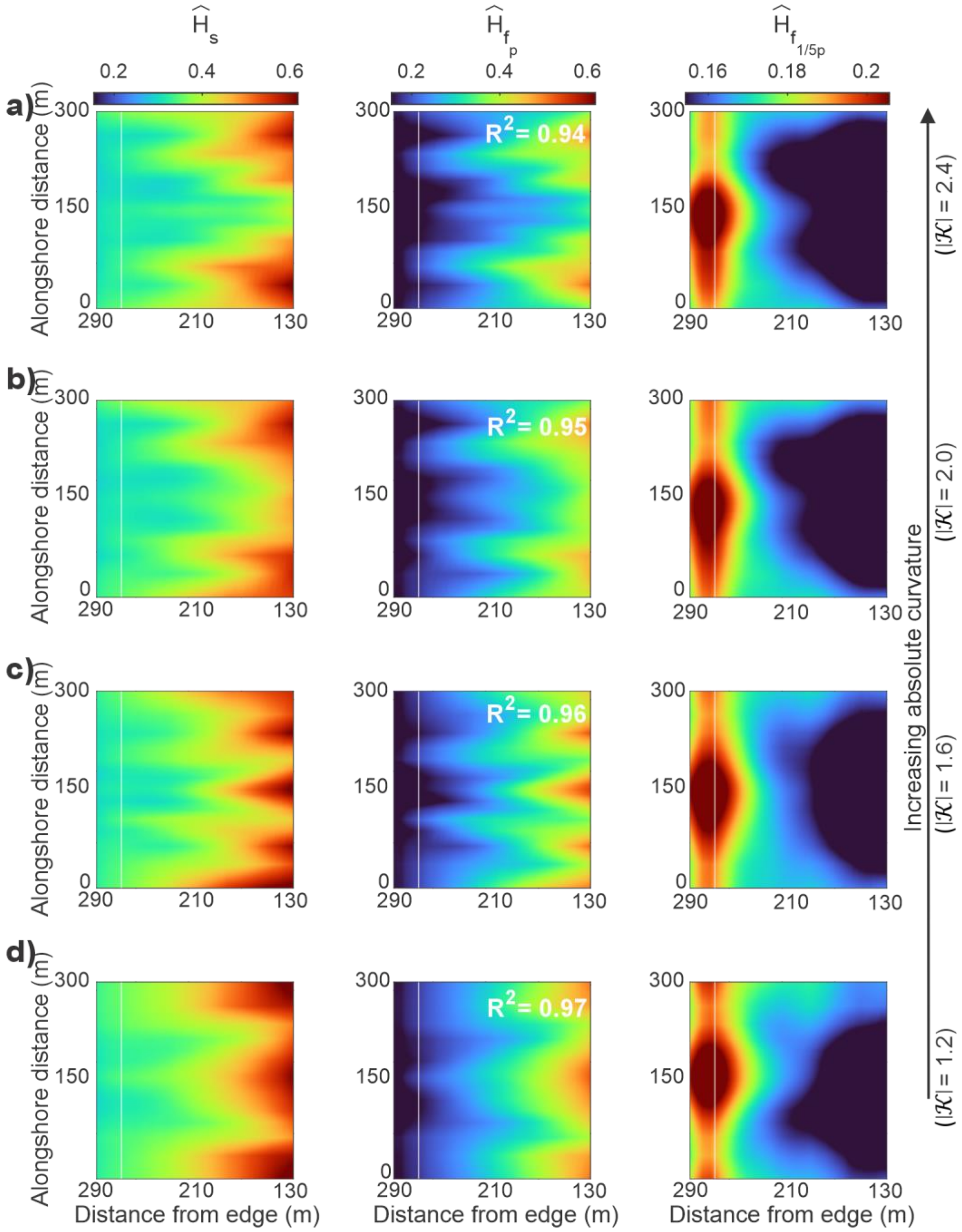

Figure 8: Wave height distribution for the entire frequency range $(\widehat{H_s})$, the principal harmonic $(\widehat{H_{f_p}})$ and the fifth subharmonic $(\widehat{H_{f_{1/5p}}})$ of non-breaking waves over the inner platform (Fig. 1) for various concave (a-d) edge curvatures. The white line represents the alongshore transect L, 20 m from the shoreline (Fig. 1). The centreline is located at $y = 150\ \mathrm{m}$. The R^2 values indicate the correlation between wave height patterns of the principal harmonic and fifth subharmonic with the significant wave height pattern for the same degree of curvature (only $R^2 \geq 0.4$ is shown, representing moderate to very strong correlations)

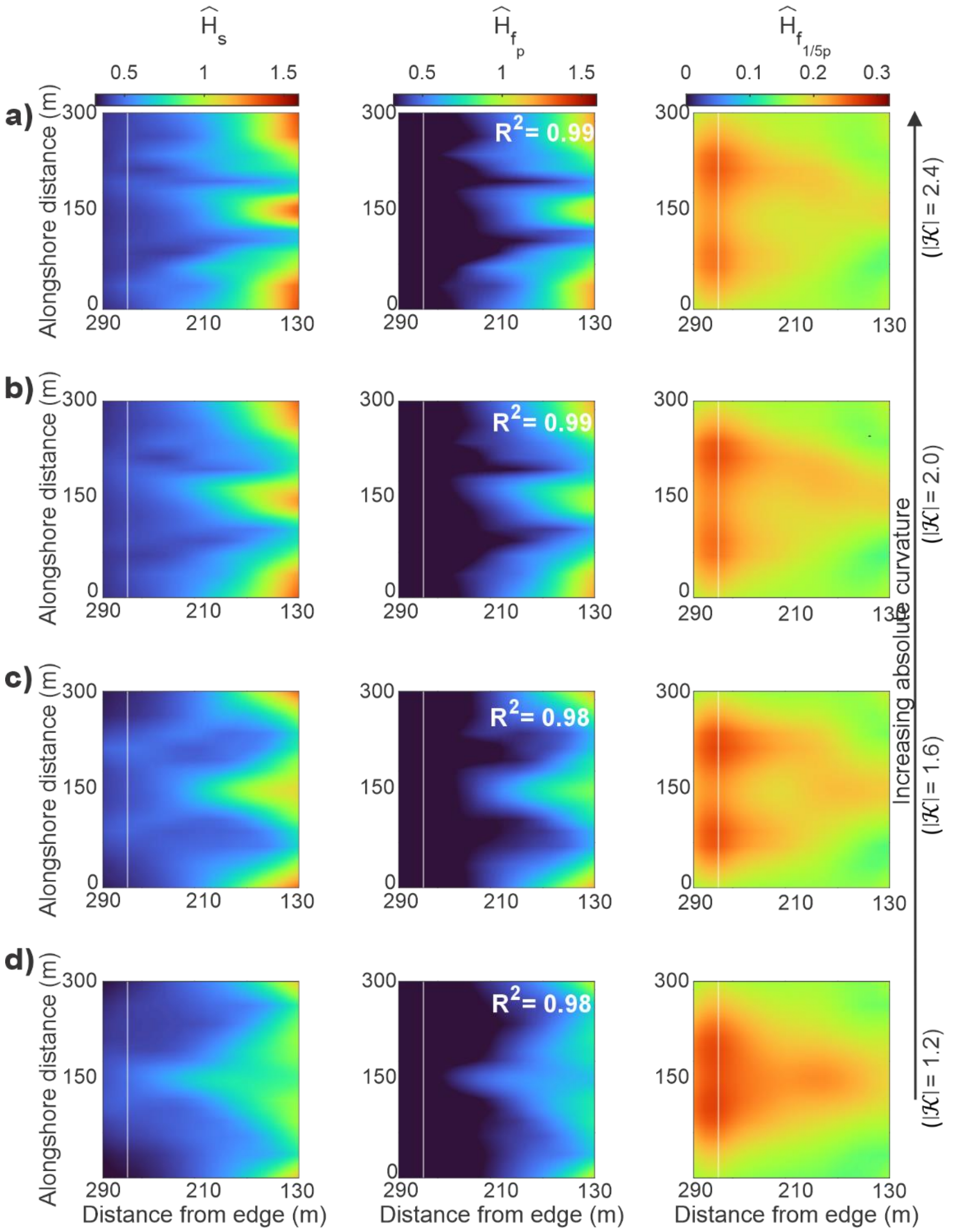

Figure 9: Wave height distribution for the entire frequency range ($\widehat{H_s}$), the principal harmonic ($\widehat{H_{f_p}}$) and the fifth subharmonic ($\widehat{H_{f_{1/5p}}}$) of non-breaking waves over the inner platform (Fig. 1) for various convex (a-d) edge curvatures. The white line represents the alongshore transect L, 20 m from the shoreline (Fig. 1). The centreline is located at $y = 150\,\mathrm{m}$. The R^2 values indicate the correlation between wave height patterns of the principal harmonic and fifth subharmonic with the significant wave height pattern for the same degree of curvature (only $R^2 \geq 0.4$ is shown, representing moderate to very strong correlations)

A strong relationship, $R^2 > 0.8$, was observed between modal coherent self-interaction patterns and wave height patterns of the principal harmonic and fifth subharmonics over the inner sections of concave (Fig. 10a) and convex platforms (Fig. 10b). This observation indicates that the alongshore variations of the principal harmonic (SW) were predominantly controlled by coherent wave interaction, which in turn drove the alongshore variations in significant wave height over the inner section of both concave and convex platforms. The resulting stationary patterns in significant wave height along the shoreline were characterised by a decrease of significant wave height toward the centreline of concave platforms (Fig. 11a), which became more pronounced with increasing curvature (maximum alongshore difference in $\widehat{H_s}$=0.05 at $|\mathcal{K}|$=1.2, increasing to 0.06 at $|\mathcal{K}|$=2.4, Fig. 10a). Over convex platforms, stationary patterns for normalised significant wave height were characterised by an increase of significant wave height toward the platform centreline at low degrees of curvature (Fig. 11b), resulting in an alongshore difference in $\widehat{H_s}$ ≈0.15 for $|\mathcal{K}|$<1.8 near the shoreline. A progressive amplification of the lobes on either side of the centreline was observed as curvature increased, resulting in a more homogenous alongshore distribution of significant wave height for high degrees of curvature ($\widehat{H_s}$ ≈0.06 for $|\mathcal{K}|$>2, Fig. 11b).

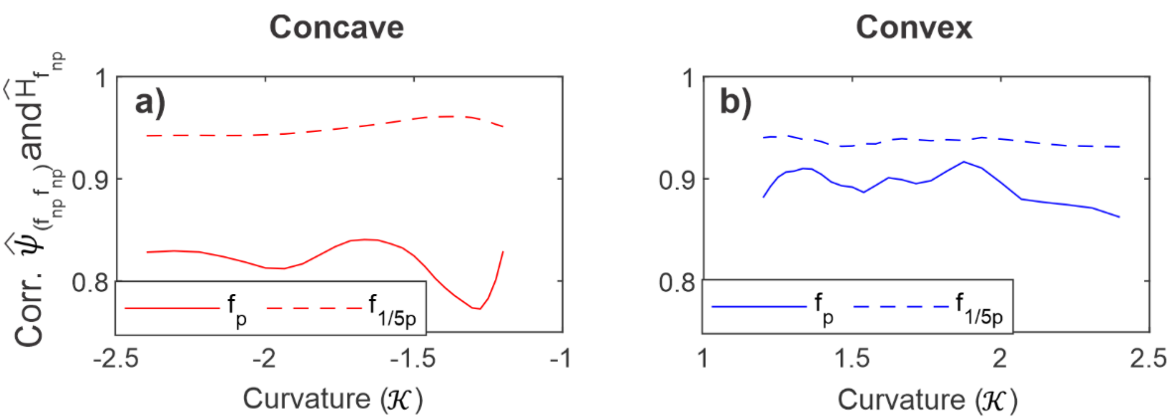

Figure 10: Correlation between interaction maps (Fig. 7) and wave height patterns (Fig. 8, 9) for the principal harmonic (f_p) and the fifth subharmonic ($f_{1/5p}$) of non-breaking waves over the inner platform of concave (a) and convex (b) edges.

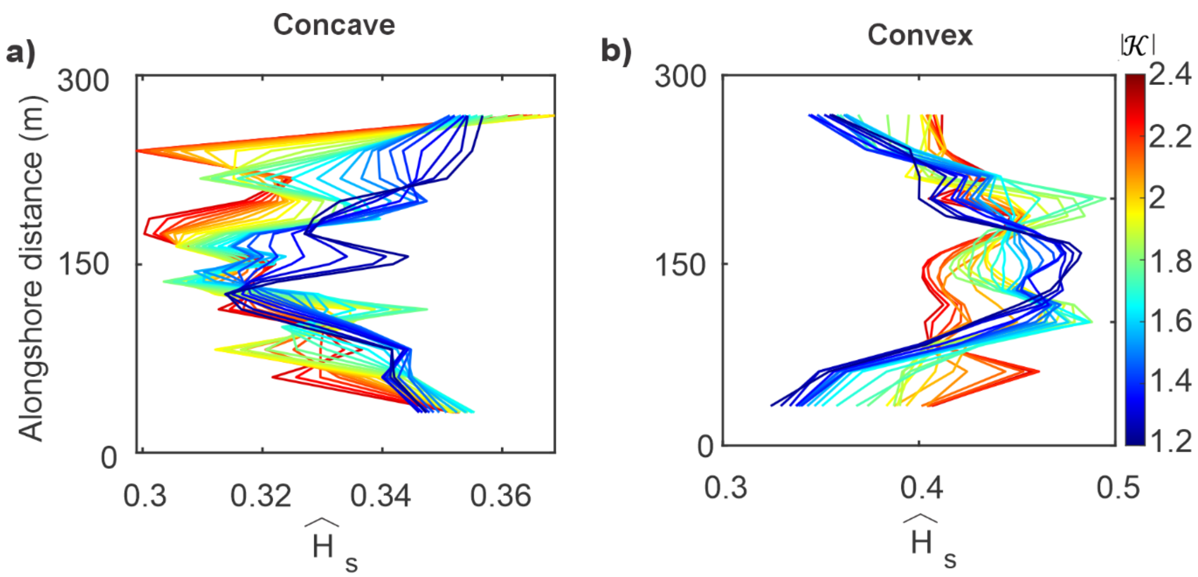

Figure 11: Alongshore variations in significant wave height patterns 20 m from the shoreline for non-breaking waves (transect L, Fig. 1) in relation to concave (a) and convex (d) edge curvatures

3.2.2 Broken waves

Coherent self-interaction patterns of the principal harmonic and fifth subharmonic of broken waves displayed alongshore variabilities over both concave and convex platforms (Fig. 12). Over the concave platforms, the coherent self-interaction zone of the principal harmonic was concentrated toward the centreline for low degrees of curvature ($|\mathcal{K}|$=1.2), spreading alongshore as the degree of curvature increased (Fig. 12a-d). Zones of coherent self-interactions for the fifth subharmonic were predominantly observed on the northern and southern extremities of the platforms and became more distinct as the edge curvature increased (Fig. 12e-h). Over the convex platforms, coherent self-interactions of the principal harmonic were the strongest on the northern and southern extremities of the platforms at $x \approx 190$ m. For the fifth subharmonic (Fig. 12m-p), areas of coherent self-interaction were concentrated along the platform centrelines for low degrees of curvature ($|\mathcal{K}|$=1.2 and 1.6), but spread either side of the platform centrelines for high degrees of curvature ($|\mathcal{K}|$=2.0 and 2.4). The differences in coherent self-interaction patterns between low and high degrees of curvature were characterised by a mild divergence over the inner section of convex platforms for curvatures greater than 1.8 (Fig. 7d).

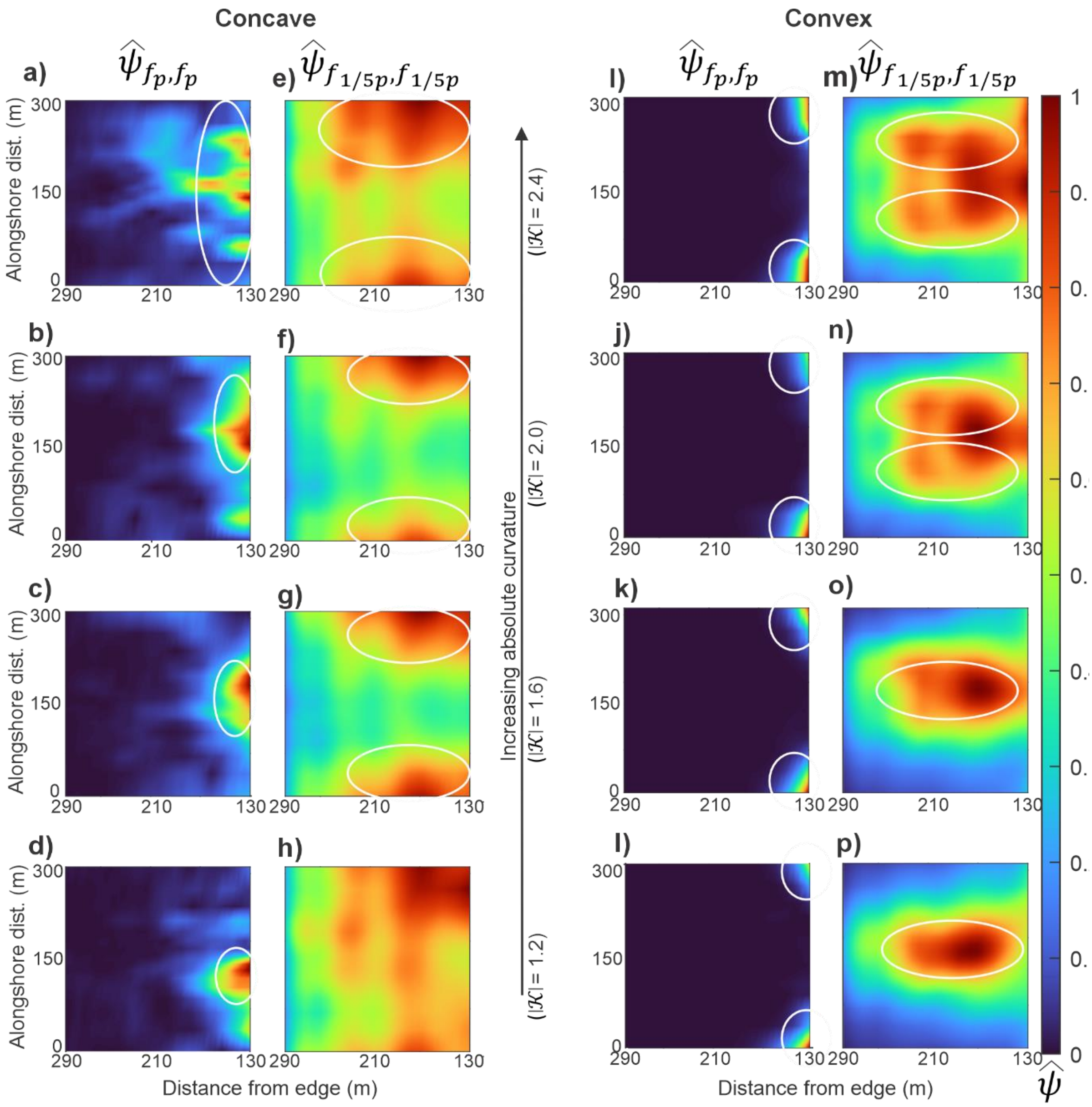

Figure 12: Coherent self-**i**nteraction maps defined from the bispectral modal state of self-interacting components for the principal harmonics (f_p) and the fifth subharmonic ($f_{1/5p}$) of broken waves over the inner platform (Fig. 1) at different concave (a-h) and convex (i-p) edge curvatures. The centreline is located at $y\ = 150$ m. Values of $\hat{\psi}$ of 1 indicate areas of strong coherent wave interactions. The white ellipses highlight the zones of strong coherent wave interactions.

For broken waves, the influence of IG_L on significant wave height distribution over the inner sections of concave and convex platforms was greater than for non-breaking waves (Fig. 13, Fig. 14). Over the inner section of the concave platforms (Fig. 13), the fifth subharmonic had greater wave height than the principal harmonic. Thus, the wave height patterns of the fifth subharmonic had a greater impact on the significant wave height patterns ($0.85 < R^2 < 0.91$ for $1.2< |\mathcal{K}|< 2.4$) than the principal harmonic ($0.74 < R^2 < 0.86$ for $1.2< |\mathcal{K}|< 2.4$) in this region. The wave height of the principal harmonic and fifth subharmonic decreased from the northern and southern extremities of the platforms to the platform centrelines. The combined effect of these patterns was a net alongshore decrease of significant wave height toward the platform centrelines. Over the inner section of convex platforms (Fig. 14), the principal harmonic displayed the greatest wave height (maximum $\widehat{H_{f_p}} \approx 0.5$) on the northern and southern sides of the platform between $x \approx$ 130-190 m. The wave height of the fifth subharmonic was relatively smaller, reaching a maximum at the platform centreline (maximum $\widehat{H_{f_p}} \approx$ 0.22-0.27), regardless of the curvature. As a result, the wave height distribution of the principal harmonic exerted a strong control on the significant wave height pattern over the inner platforms ($0.9 < R^2 < 0.95$) in comparison to the control exerted by the fifth subharmonic ($0.4 < R^2 < 0.58$). However, the wave height of the principal harmonic significantly decreased past $x \approx 190$ m, becoming comparable to the wave height of the fifth subharmonic. Thus, alongshore variations in significant wave height were controlled by alongshore patterns of both principal harmonic and fifth subharmonic for $x \geq 190$ m. For low degrees of edge curvature ($|\mathcal{K}|$=1.2), the maximum wave height of the fifth subharmonic was observed at the platforms' centreline and evolved with increasing curvature to form two maxima on either side of the centreline for large degrees of edge curvature ($|\mathcal{K}|$= 2.2 and 2.4). This evolution was clearly observed in the significant wave height pattern between $x =$ 190 and 300 m, underlining the influence of the fifth subharmonic (IG_L) on the alongshore variation of significant wave height at the shoreline.

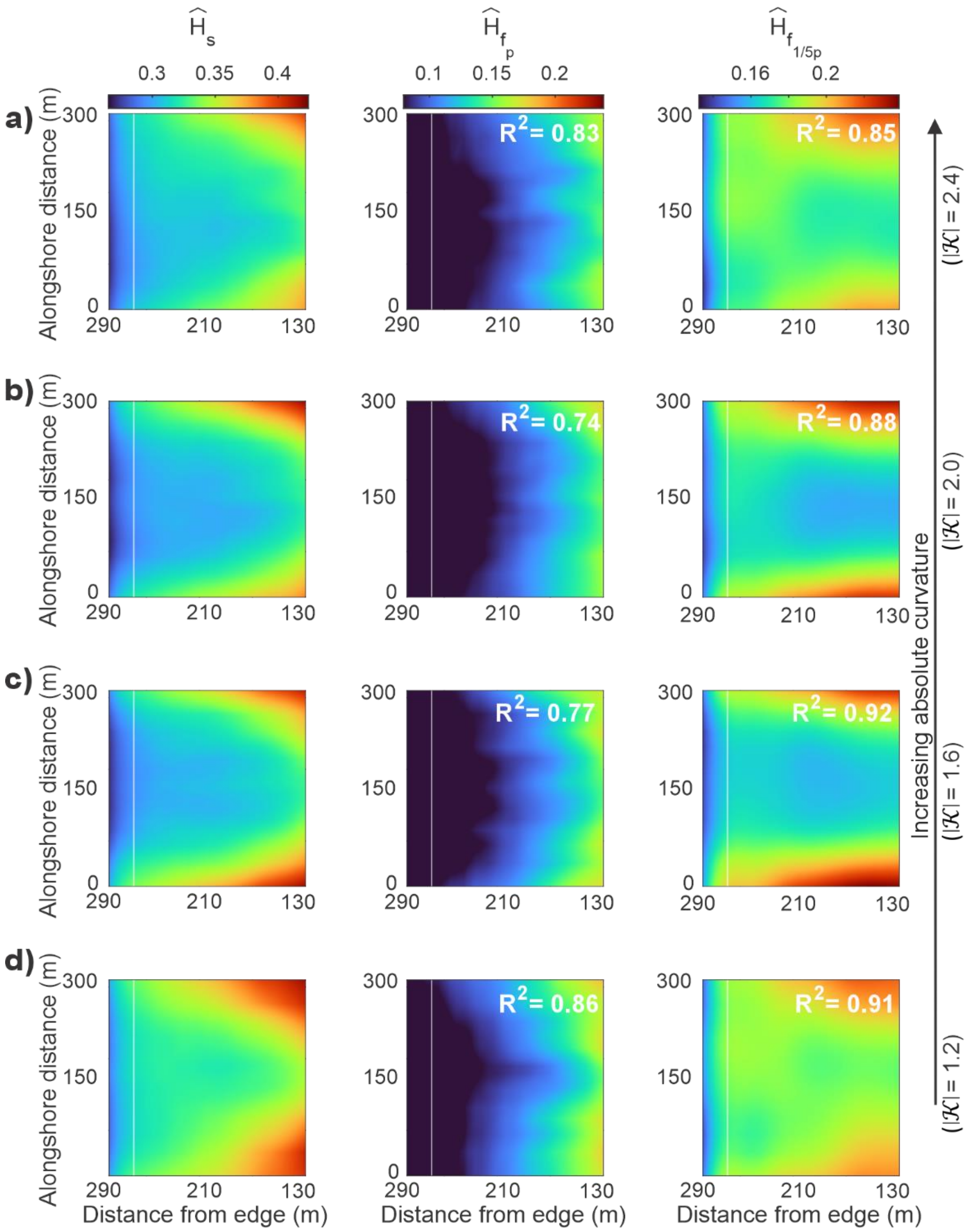

Figure 13: Wave height distribution for the entire frequency range ($\widehat{H_s}$), the principal harmonic ($\widehat{H_{fp}}$) and the fifth subharmonic ($\widehat{H_{f_{1/5p}}}$) of broken waves over the inner platform (Fig. 1) for various concave (a-d) edge curvatures. The white line represents the alongshore transect L, 20 m from the shoreline. The centreline is located at $y = 150$ m. The R^2 values indicate the correlation between wave height patterns of the principal harmonic and fifth subharmonic with the significant wave height pattern for the same degree of curvature.

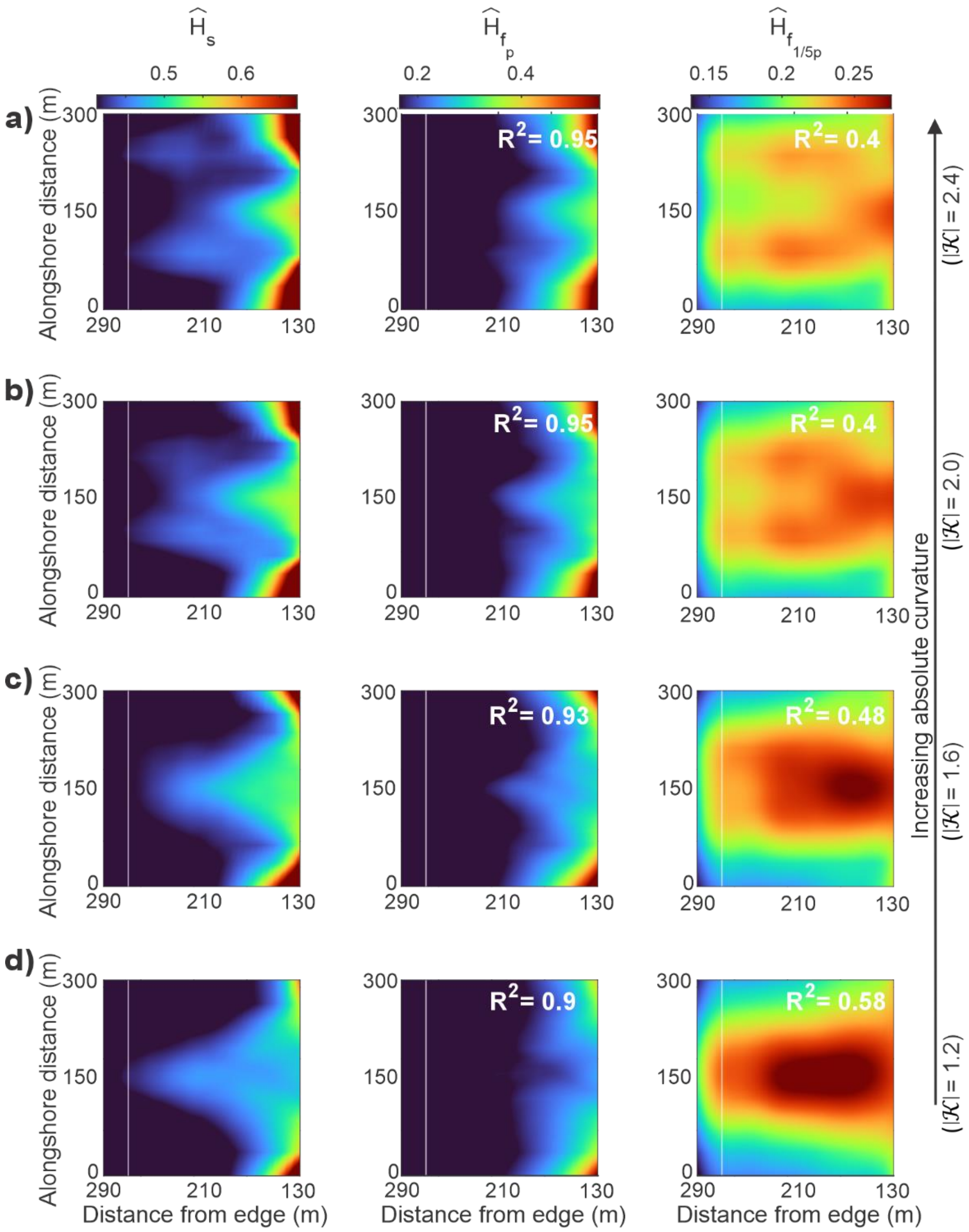

Figure 14: Wave height distribution for the entire frequency range ($\widehat{H_s}$), the principal harmonic ($\widehat{H_{f_p}}$) and the fifth subharmonic ($\widehat{H_{f_{1/5p}}}$) of broken waves over the inner platform (Fig. 1) for various convex (a-d) edge curvatures. The white line represents the alongshore transect L, 20 m from the shoreline. The centreline is located at y =150 m. The R^2 values indicate the correlation between wave height patterns of the principal harmonic and fifth subharmonic with the significant wave height pattern for the same degree of curvature.

Strong ($R^2 > 0.8$) and moderate to strong ($0.5 < R^2 < 0.7$) relationships were observed over the inner sections of concave (Fig. 15a) and convex platforms (Fig. 15b) between modal coherent self-interaction patterns and wave height patterns for the fifth subharmonics and principal harmonics, respectively. The implication is that coherent wave amplification influenced the longshore patterns of wave height for the principal harmonic and fifth subharmonic over the inner platform, although this process had a smaller impact on the principal harmonic. Thus, coherent wave amplification at IG frequencies was the principal process controlling alongshore variations of significant wave height along the shoreline. The resulting stationary patterns in significant wave height along the shoreline were marked by a decrease of significant wave height toward the centreline of concave platforms, which became more pronounced with increasing curvature (maximum alongshore difference in $\widehat{H_s}$=0.04 at $|\mathcal{K}|$=1.2, increasing to 0.02 at $|\mathcal{K}|$=2.4, Fig. 16a). For convex platforms, an increase of significant wave height toward the platform centreline was observed at low degrees of curvature, resulting in maximum alongshore variations of significant wave height $\widehat{H_s} \approx 0.08$ for $|\mathcal{K}|$<1.8. A progressive amplification of the lobes on either side of the centreline generated two wave height maxima for high degrees of curvature, for which maximum alongshore variations of significant wave height $\widehat{H_s} \approx 0.06$ for $|\mathcal{K}|$>2 (Fig. 16b).

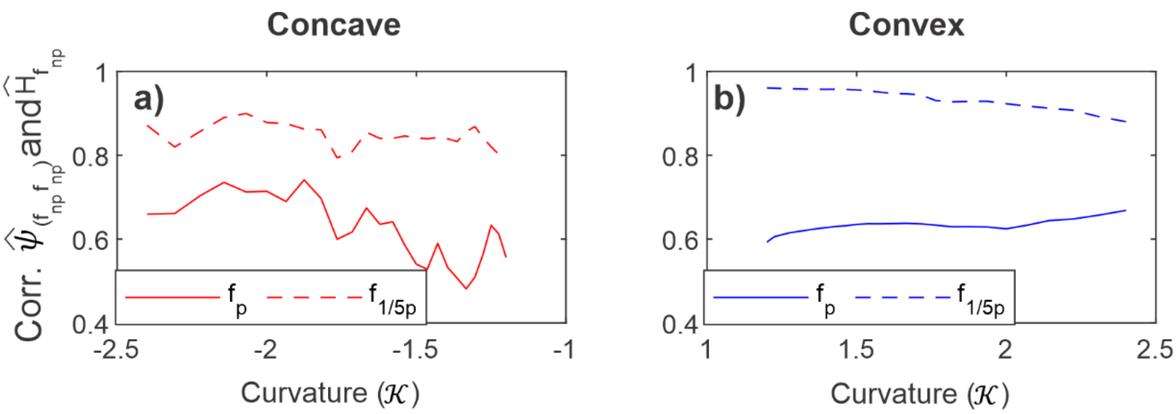

Figure 15: Correlation between interaction maps and wave height patterns for the principal harmonic (f_p) and the fifth subharmonic ($f_{1/5p}$) of broken waves over the inner platform of concave (a) and convex (b) edges.

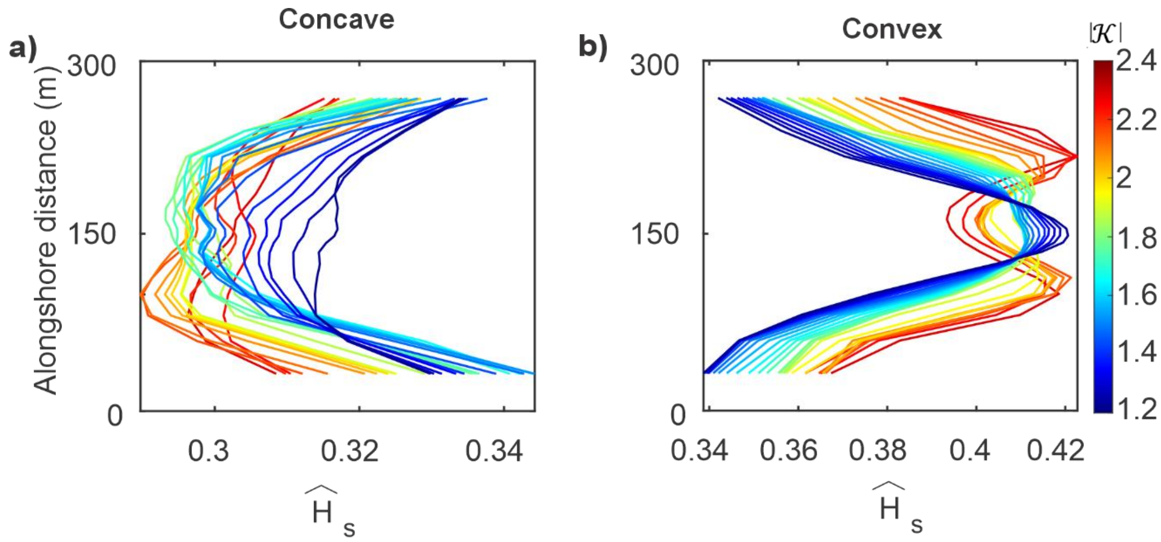

Figure 16: Alongshore variations in normalised significant wave height patterns 20 m from the shoreline (transect L) for broken waves in relation to concave (a) and convex (d) curvature.

4 Discussion

4.1 Impact of platform edge geometry on wave transformation across shore platforms

Modelling studies generally investigate the impact of refraction on wave energy distribution over a fixed curvature (e.g. Berkhoff et al., 1982; Li et al., 2020), whereas in this work, we varied the degree of edge curvature and analysed its effect on the transformation of harmonic components. Increasing concave edge curvature decreased the wave energy of harmonic components in WW, SW, IG_H and IG_L frequency bands (Fig. 2b-e, 4b-e), accounting for up to 25% reduction in $\widehat{H_S}$ (Fig. 3a, 5a). In contrast, increasing convex edge curvature amplified both the second and principal harmonics in the WW and SW frequency bands over the outer platforms, increasing $\widehat{H_S}$ by up to 55% and 18% for non-breaking and broken waves (Fig. 3b, 5b) while minimizing the amplification of the fifth subharmonic within the IG_L frequency band over the inner platforms (Fig. 2g-j, 4g-j). Thus, it is clear that morphological variability in platform edge curvature influences significant wave height on shore platforms, and this has potential implications for backwear and downwear erosion processes on rock coasts (e.g. Trenhaile, 1987, Matsumoto et al., 2016a,b).

Amplification of higher harmonics associated with wave refraction has previously been associated with wave focusing (Gouin et al., 2017), but the impact of edge curvature on amplification has not been considered. Our modelling results show that increasing convex edge curvature enhances wave focussing over the outer platform (Fig. 3, 5), promoting the generation of higher harmonic from non-linear triadic (sum) interactions (Janssen and Herbers, 2009; Jarry et al., 2011; Lawrence et al., 2022). Shore platform studies have linked the generation and dominance of high-frequency waves over the outer section of near-horizontal platforms to locally generated wind waves (e.g. Ogawa et al., 2011; 2016). Though this process cannot be ruled out, the nearshore wind speed required for locally produced WW energy is substantial (Hasselmann et al., 1973), and the generation of higher harmonics from non-linear triadic interaction caused by wave refraction appears to be a more plausible physical interpretation for high-frequency wave generation on the outer sections of shore platforms.

Research has demonstrated that wave amplification in the IG frequency band over near-horizontal platforms is influenced by the ratio of water depth at the cliff toe to the platform width, and relative submergence (Beetham and Kench, 2011; Ogawa et al., 2015). We show that edge curvature exerts an additional morphological control on IG amplification across convex platforms by affecting the balance between focusing intensity from refraction and defocusing effects from wave breaking controlled by convex edges (Fig. 4, 5). Although a decrease in convex edge curvature should theoretically result in a landward shift of the focal point over submerged flats (e.g. Mandlier and Kench, 2012), a seaward shift of the focal point was observed in this study for broken waves (Fig. 5d). This phenomenon can be attributed to the defocussing effects resulting from the enhancement of radiation stress and wave-generated current by wave breaking (Yoon et al., 2004; Choi et al., 2009). A critical curvature was found for which the intensity of wave focusing by wave refraction is not strong enough to overcome the defocusing effects of wave breaking, identified here as $|\mathcal{K}|$=1.8 (Fig. 5d). When the critical curvature is exceeded, wave rays intersect across the platform centreline, in which cases, IG amplification is minimised by wave ray divergence over the inner platform (Fig. 6d). In contrast, for convex edge curvatures lower than the critical curvature, wave rays do not intersect across the platform centreline, sustaining wave convergence across the entire platform. In this case, IG amplification is promoted over the inner platform, representing up to 15% of the increase in significant wave height at this position (Fig. 6d). Thus, the present research identifies convergence as a key mechanism acting on the growth of IG across shore platform, working in conjunction with other processes such as to breakpoint forcing (Poate et al., 2020) and energy transfer from higher frequencies and shoaling (Beetham and Kench, 2011).

In a conceptual model, Ogawa et al. (2011) described spatial zones on a shore platform that are dominated by different wave types and pointed out that the spatial characteristics change according to the tidal stage. Here, we show that shifts in dominant wave types across shore platforms are also controlled by convex edge curvature (certainly at high tide). High convex curvature amplifies harmonics within the WW and SW frequency bands over the outer platform and inhibits the amplification of IG over the inner platform (Fig. 4g). Low degrees of convex curvature have the opposite effect (Fig. 4j), resulting in the seaward shift of the zones dominated by WW and SW frequency bands. The influence of refraction patterns generated by convex edge geometries on the collective behaviour of harmonics affected the significant wave height patterns across convex platforms. Baldock et al. (2020) hypothesised that the significant wave height across convex platforms is defined by a specific balance between cross-shore energy loss from dissipation and energy gain from oblique refracted SW, resulting in a correlation between significant wave height anomalies and refraction patterns. The strong relationship ($\rho_s > 0.6$) observed between directional patterns and significant wave height anomalies of non-breaking waves (Fig. 3f) suggest that, for this wave state, energy is effectively gained across the platform from refracted SW. However, for broken waves, the correlation between directional patterns and significant wave height anomalies ($\Delta\widehat{H_s}$) decreased with curvature to become weak ($\rho_s < 0.4$) below the critical curvature threshold (Fig. 5f). These differences are attributed to the influence of IG growth on significant wave height over the inner platform due to the amplification of IG from post-breaking energy transfer from high to low frequency (Poate et al., 2020), and low sustained convergence across the platform (Fig. 5b, 6d). These results underline the importance of considering the refraction patterns of both SW and IG when investigating significant wave height patterns across convex submerged flats.

4.2 Impact of platform edge geometry on along shore wave transformation

Coherent wave amplification is identified here as a crucial process affecting SW and IG_L height distribution in the inner section of near-horizontal platforms. For non-breaking waves, the dominant frequencies within both SW and IG_L frequency bands presented strong correlations between patterns of coherent wave interaction and wave height distribution over concave and convex platforms (Fig. 10). However, this correlation decreased for the principal harmonic in the SW frequency bands in the presence of wave breaking (Fig. 15), perhaps due to the combination of defocussing (Yoon et al., 2004) and dissipation effects (Farrell et al., 2009) associated with wave breaking.

The present observations validate the hypothesis of Winter et al. (2017) on the formation of alongshore stationary IG patterns from wave refraction over convex platforms. However, our results suggest that such patterns are generated by coherent wave interaction following the generation of caustic rays in the IG_L frequency band (Fig. 7m-p, 12m-p) rather than alongshore standing waves, as Winter et al. (2017) suggested. In fact, the latter would require interacting IG to propagate alongshore in opposite directions. The directional analysis presented here precludes such a possibility ($\alpha \approx 0°$ near the shoreline, Fig. 3, 5). As the present paper demonstrates the coherent wave interaction plays crucial role in alongshore IG wave patterns, a coherent wave class should be added to the resonant, progressive-dissipative, standing and progressive-growing low-frequency wave classes previously identified over submerged flats (Gawehn et al., 2016).

The combined modes of SW and IG coherent wave amplification exerted a crucial control on the stationary patterns of significant wave heights over the inner platform. For non-breaking waves, significant wave height variations over the inner platform are predominantly controlled by coherent wave amplification of SW (Fig. 7, 8). In contrast, for breaking waves, the distribution of significant wave height over the inner platform became controlled by coherent wave amplification occurring within both SW and IG_L frequency components as IG_L became a prominent wave type in this region (Ogawa et al. 2011) (Fig. 13, 14). The present results support the conceptual model presented by Krier-Mariani et al. (2022), suggesting that patterns of wave ray intersection on either side of concave edge sections result in stationary SW and IG amplification patterns. The control exerted by the critical curvature on the alongshore distribution of SW and IG over convex platforms can be attributed to the generation of a terminal point (marking the transition from wave ray convergence to divergence) at the platform centreline for convex curvatures exceeding the critical curvature. In such cases, caustic rays are formed on either side of the centreline (Mandlier and Kench, 2012), promoting coherent wave interactions in these regions (Fig. 12a, 14a).

It follows that the control exerted by platform curvature on coherent wave amplification plays an essential role in the nodal state of significant wave height along the shoreline (Fig. 11, 16). For concave platforms, a node near the centreline and antinodes on the northern and southern extremities of the platform were observed. For convex edge curvature under the critical curvature threshold, an antinode was observed along the platform centreline where waves converged, while for curvature exceeding the critical curvature threshold, two antinodes were observed on either side of the platform centreline. While such patterns could wrongly be associated with edge waves, the present results support the observations of Dalrymple (1975), who first associated nodal and anti-nodal points in alongshore wave height patterns with coherent wave interaction.

It has previously been established that by controlling the nodal state of significant wave height along the shoreline of open coasts, coherent wave amplification could lead to the formation of rip currents (Dalrymple, 1975; Wei and Dalrymple, 2017). This mechanism is expected to impact circulation patterns over near-horizontal platforms equally. da Silva et al. (2023) identified alongshore pressure gradient as the dominant driver of circulation patterns in the lee of submerged flats, resulting in two or four-cell circulation systems. A two-cell system is typically characterised by an alongshore diverging flow from the lee of the submerged flat edge to the shoreline, while a four-cell system is characterised by an alongshore diverging flow at the lee of the submerged flat and a converging flow at the shoreline. Considering the present results, it can be hypothesised that stationary wave patterns and the subsequent alongshore pressure gradient generated by coherent wave amplification drive the formation of circulation cells over convex platforms. Theoretically, the formation of two antinodes over the inner platform would result in a four-cell circulation system (Fig. 14a,b, Fig. 16b), while an antinode across the entire platform would result in a two-cell circulation system (Fig. 14c,d, Fig.16b). These differences depend on whether or not the submerged flat geometry allows for the formation of a terminal point. Previous studies established that this condition was predominantly controlled by the distance between the seaward edge of submerged flats and the shoreline (da Silva et al., 2022, 2023; Ranasinghe et al., 2006, 2010), while we show that the degree of edge curvature is equally important (Fig. 11, 16).

5 Conclusions

This study employed an exploratory numerical modelling approach to investigate the impact of concave and convex platform edge geometries on the behaviour of wave harmonics and the subsequent wave height distribution patterns over near-horizontal shore platforms. Harmonic analyses show that refraction patterns controlled by concave and convex platform edge curvatures result in wave height variation for the principal and second higher harmonics over the outer platform, and for the subharmonics over the inner platform. Wave divergence across concave edge platforms decreased the height of harmonics within both SW and IG frequency bands, resulting in the attenuation of significant wave height for high degrees of curvature. Over the outer section of convex platforms, increasing curvature intensified wave focusing and amplified the principal and second harmonics within the SW frequency band. A critical curvature value of 1.8 demarcates the formation of a wave ray divergence zone over the inner platform, conditioned by the balance between wave focusing from wave refraction and wave defocusing from wave breaking. Below this threshold, wave convergence amplified IG over the inner platform, but over this threshold, wave divergence reduced the amplification of IG over the inner platform. Through these mechanisms, it is apparent that edge curvature can influence both the relative dominance of SW and IG frequencies, and the pattern of significant wave height transformation across near-horizontal platforms. Using a high-order spectral decomposition method, this study further demonstrated that coherent wave amplification influences stationary IG and SW patterns over the inner platform, affecting the alongshore distribution of significant wave height. We found that platform geometry controls the nodal state of the stationary patterns along the shoreline, possibly resulting in alongshore variation of wave erosive force and the generation of wave-generated currents shaping rock coasts.

Acknowledgements

. RKM is supported by a University of Otago PhD Scholarship and a New Zealand Coastal Society Student Research Scholarship. Mark Dickson and Wayne Stephenson are supported by a Royal Society Te Apārangi, Marsden Fund Grant Number UOO1828. We are grateful for the assistance and support provided by Callum Walley and the rest of the team from NeSi for allowing us to set up and run our models on their supercomputer facilities.

Open research

The numerical model input files and post processed data for the model simulations (Using FUNWAVE 3.6) over idealised shore platform geometries are available at *Public release planned after review*.

References

Baldock, T.E., Shabani, B., Callaghan, D.P., Hu, Z., Mumby, P.J., 2020. Two-dimensional modelling of wave dynamics and wave forces on fringing coral reefs. Coast. Eng. 155, 103594. https://doi.org/10.1016/j.coastaleng.2019.103594

Beetham, E.P., Kench, P.S., 2011. Field observations of infragravity waves and their behaviour on rock shore platforms. Earth Surf. Process. Landforms 36, 1872–1888. https://doi.org/10.1002/esp.2208

Berkhoff, J.C.W., Booy, N., Radder, A.C., 1982. Verification of numerical wave propagation models for simple harmonic linear water waves. Coast. Eng. 6, 255–279. https://doi.org/10.1016/0378-3839(82)90022-9

Blenkinsopp, C.E., Chaplin, J.R., 2008. The effect of relative crest submergence on wave breaking over submerged slopes. Coast. Eng. 55, 967–974. https://doi.org/10.1016/j.coastaleng.2008.03.004

Buckley, M.L., Lowe, R.J., Hansen, J.E., Van Dongeren, A.R., 2015. Dynamics of wave setup over a steeply sloping fringing reef. J. Phys. Oceanogr. 45, 3005–3023. https://doi.org/10.1175/JPO-D-15-0067.1

Buckley, M.L., Lowe, R.J., Hansen, J.E., Van Dongeren, A.R., Storlazzi, C.D., 2018. Mechanisms of wave-driven water level variability on reef-fringed coastlines. J. Geophys. Res. Ocean. 123, 3811–3831. https://doi.org/10.1029/2018JC013933

Chen, Q., Dalrymple, R.A., Kirby, J.T., Kennedy, A.B., Haller, M.C., 1999. Boussinesq modeling of a rip current system. J. Geophys. Res. Ocean. 104, 20617–20637. https://doi.org/10.1029/1999jc900154

Chen, Q., Kirby, J.T., Dalrymple, R.A., Shi, F., Thornton, E.B., 2003. Boussinesq modeling of longshore currents. J. Geophys. Res. 108, 1–18. https://doi.org/10.1029/2002JC001308

Choi, J., Lim, C.H., Lee, J.I., Yoon, S.B., 2009. Evolution of waves and currents over a submerged laboratory shoal. Coast. Eng. 56, 297–312. https://doi.org/10.1016/j.coastaleng.2008.09.002

Dalrymple, R.A., 1975. A mechanism for Rip Current Generation on an open Coast. J. Geophys. Res. 80, 3485–3487.

da Silva, R. F., Hansen, J. E., Lowe, R. J., Rijnsdorp, D. P., & Buckley, M. L., 2023. Dynamics of the wave-driven circulation in the lee of nearshore reefs. Journal of Geophysical Research: Oceans, 128, e2022JC019013. https://doi.org/10.1029/2022JC019013

da Silva, R. F., Hansen, J. E., Rijnsdorp, D. P., Lowe, R. J., & Buckley, M. L. 2022. The influence of submerged coastal structures on nearshore flows and wave runup. Coastal Engineering, 177, 104194. https://doi.org/10.1016/j.coastaleng.2022.104194

Emery, W.J., Thomson, R.E., 2014. Time-series Analysis Methods, Data Analysis Methods in Physical Oceanography. Elsevier, Amsterdam. https://doi.org/10.1016/b978-044450756-3/50006-x

Falk, L., 1979. On The Phase Integral Of Coherent Three-wave Interaction. Phys. Lett. 71, 61–62.

Farrell, E.J., Granja, H., Cappietti, L., Ellis, J.T., Li, B., Sherman, D.J., 2009. Wave transformation across a rock platform, Belinho, Portugal. J. Coast. Res. 44–48.

Gawehn, M., Van Dongeren, A., Van Rooijen, A., Storlazzi, C.D., Cheriton, O.M., Reniers, A., 2016. Identification and classification of very low frequency waves on a coral reef flat. J. Geophys. Res. Ocean. 121, 3010–3028. https://doi.org/10.1002/2016JC011834.Received

Gouin, M., Ducrozet, G., Ferrant, P., 2017. Propagation of 3D non-linear waves over an elliptical mound with a High-Order Spectral method. Eur. J. Mech. B/Fluids 63, 9–24. https://doi.org/10.1016/j.euromechflu.2017.01.002

Gottlieb, S., Shu, C.-W., Tadmor, E., 2001. Strong stability-preserving high-order time discretization methods. SIAM Review 43, 89–112.

Griffiths, L.S., Porter, R., 2012. Focusing of surface waves by variable bathymetry. Appl. Ocean Res. 34, 150–163. https://doi.org/10.1016/j.apor.2011.08.004

Harid, V., Gołkowski, M., Bell, T., Li, J.D., Inan, U.S., 2014. Finite difference modeling of coherent wave amplification in the Earth's radiation belts. Geophys. Res. Lett. 41, 8193–8200. https://doi.org/10.1002/2014GL061787

Hashimoto, N., Nagai, T., Asai, T., 1994. Extension of the Maximum Entropy Principle Method for Directional Wave Spectrum Estimation, in: Coastal Engineering Proceedings. pp. 232–246. https://doi.org/10.1061/9780784400890.019

Hasselmann, K., Barnett, T.P., Bouws, E., Carlson, H., Cartwright, D.E., Enke, K., Ewing, J.A., Gienapp, H., Hasselmann, D.E., Kruseman, P., Meerburg, A., Muller, P., Olbers, D.J., Richter, K., Sell, W., Walden, H., 1973. Measurements of wind-wave growth and swell decay during the Joint North Sea Wave Project (JONSWAP). UDO 551.466.31; ANE German Bight, Deutsches Hydrographisches Institut Hamburg.

Hasselmann, K., Munk, W.H., MacDonald, G., 1963. Bispectra of Ocean Waves, in: Rosenblatt, M. (Ed.), Symposium on Time Series Analysis. pp. 125–139.

Inouye, S., Pfau, T., Gupta, S., Chikkatur, A.P., Görlitz, A., Pritchard, D.E., Ketterle, W., 1999. Phase-coherent amplification of atomic matter waves. Nature 402, 641–644.

https://doi.org/10.1038/45194

Ito, Y., Tanimoto, K., 1972. A Method of Numerical Analysis of Wave Propagation-Application To Wave Diffraction and Refraction. Proc. 13Th. Coast. Engng. Conf., (Vancouver, Canada) 1, 503–522. https://doi.org/10.9753/icce.v13.25

Janssen, T.T., Herbers, T.H.C., 2009. Non-linear wave statistics in a focal zone. J. Phys. Oceanogr. 39, 1948–1964. https://doi.org/10.1175/2009JPO4124.1

Jarry, N., Rey, V., Gouaud, F., Lajoie, D., 2011. Gravity wave amplification and phase crest re-organization over a shoal. Nat. Hazards Earth Syst. Sci. 11, 789–796. https://doi.org/10.5194/nhess-11-789-2011

Kennedy, A.B., Kirby, J.T., Chen, Q., Dalrymple, R.A., 2001. Boussinesq-type equations with improved non-linear performance. Wave Motion 33, 225–243. https://doi.org/10.1016/S0165-2125(00)00071-8

Kim, Y.C., Powers, E.J., 1979. Digital Bispectral Analysis and Its Applications to Non-linear Wave Interactions. IEEE Trans. Plasma Sci. 7, 120–131. https://doi.org/10.1109/TPS.1979.4317207

Kozuma, M., Suzuki, Y., Torii, Y., Sugiura, T., Kuga, T., Hagley, E., Deng, L., 1999. Phase-Coherent Amplification of Matter Waves. Science (80-.). 286, 2309–2312.

Stephenson, W.J., Kirk, R.M., 2000a. Development of shore platforms on Kaikoura Peninsula , South Island , New Zealand Part One : The role of waves. Geomorphology 32, 21–41.

Krier-Mariani, R.L., Stephenson, W.J., Wakes, S.J., Dickson, M.E., 2023. The effects of planform morphology on two-dimensional wave transformation over near-horizontal shore platforms. Geomorphology 422, 108555. https://doi.org/10.1016/j.geomorph.2022.108555

Krier-Mariani, R.L., Stephenson, W.J., Wakes, S.J., Dickson, M.E., 2022. Perspectives on wave transformation over a near-horizontal shore platform: Comparison of a two-dimensional and transect approach. Geomorphology 405, 108200. https://doi.org/10.1016/j.geomorph.2022.108200

Lawrence, C., Trulsen, K., Gramstad, O., 2022. Extreme wave statistics of surface elevation and velocity field of gravity waves over a two-dimensional bathymetry. J. Fluid Mech. 939, 1–18. https://doi.org/10.1017/jfm.2022.227

Li, C.Y., Shih, R.S., Weng, W.K., 2020. Investigation of ocean-wave-focusing characteristics induced by a submerged crescent-shaped plate for long-crested waves. Water 12, 1–17. https://doi.org/10.3390/w12020509

Lumley, J.L. 1967. The Structure of Inhomogeneous Turbulent Flows. In: Yaglom, A.M. and Tartarsky, V.I., Eds., Atmospheric Turbulence and Radio Wave Propagation, 166-177.

Lynett, P., Liu, P.L.F., 2004. A two-layer approach to wave modelling. Proc. R. Soc. A Math. Phys. Eng. Sci. 460, 2637–2669. https://doi.org/10.1098/rspa.2004.1305

Mandlier, P.G., Kench, P.S., 2012. Analytical modelling of wave refraction and convergence on coral reef platforms: Implications for island formation and stability. Geomorphology 159–160, 84–92. https://doi.org/10.1016/j.geomorph.2012.03.007

Marshall, R.J.E., Stephenson, W.J., 2011. The morphodynamics of shore platforms in a micro-tidal setting: Interactions between waves and morphology. Mar. Geol. 288, 18–31. https://doi.org/10.1016/j.margeo.2011.06.007

Matsumoto, H., Dickson, M.E., Kench, P.S., 2016a. An exploratory numerical model of rocky shore profile evolution. Geomorphology 268, 98–109. https://doi.org/10.1016/j.geomorph.2016.05.017

Matsumoto, H., Dickson, M.E., Kench, P.S., 2016b. Modelling the Development of Varied Shore Profile Geometry on Rocky Coasts Modelling the Development of Varied Shore Profile Geometry on Rocky Coasts. J. Coast. Res. 75(sp1), 597–601. https://doi.org/10.2112/SI75-120.1

Mendonca, A., Neves, M. G. and Fortes, C. J., 2008. Numerical Study of Hydrodynamics around an artificial surf reef for São Pedro do Estoril, Portugal, SI 56 (Proceedings of the 10th International Coastal Symposium), 1010 – 1014. Lisbon, Portugal, ISSN 0749-0258.

Ogawa, H., Dickson, M.E., Kench, P.S., 2016. Generalised observations of wave characteristics on near-horizontal shore platforms: Synthesis of six case studies from the North Island, New Zealand. N. Z. Geog. 72, 107–121. https://doi.org/10.1111/nzg.12121

Ogawa, H., Dickson, M.E., Kench, P.S., 2015. Hydrodynamic constraints and storm wave characteristics on a sub-horizontal shore platform. Earth Surf. Process. Landforms 40, 65–77. https://doi.org/10.1002/esp.3619

Ogawa, H., Dickson, M.E., Kench, P.S., 2011. Wave transformation on a sub-horizontal shore platform , Tatapouri , North Island , New Zealand. Cont. Shelf Res. 31, 1409–1419. https://doi.org/10.1016/j.csr.2011.05.006

Pequignet, A.-C.N., Becker, J.M.B., Merrifield, M.A.M., 2014. Energy transfer between wind waves and low-frequency oscillations on a fringing reef, Ipan, Guam Anne-Christine. J. Geophys. Res. Ocean. 3868–3882. https://doi.org/10.1002/2014JC010179.Received

Poate, T., Masselink, G., Austin, M.J., Inch, K., Dickson, M., McCall, R., 2020. Infragravity wave generation on shore platforms: Bound long wave versus breakpoint forcing. Geomorphology 350, 1–15. https://doi.org/10.1016/j.geomorph.2019.106880

Priestley, M.B. 1981: Spectral Analysis and Time Series. Academic Press, London.

Ranasinghe, R., Larson, M., & Savioli, J., 2010. Shoreline response to a single shore-parallel submerged breakwater. Coastal Engineering, 57(11–12), 1006–1017. https://doi.org/10.1016/j.coastaleng.2010.06.002

Ranasinghe, R., Turner, I. L., & Symonds, G., 2006. Shoreline response to multi-functional artificial surfing reefs: A numerical and physical modelling study. Coastal Engineering, 53(7), 589–611. https://doi.org/10.1016/j.coastaleng.2005.12.004

Schmidt, O.T., 2020. Bispectral mode decomposition of non-linear flows. Non-linear Dyn. 102, 2479–2501. https://doi.org/10.1007/s11071-020-06037-z

Sheremet, A., Kaihatu, J.M., Su, S.F., Smith, E.R., Smith, J.M., 2011. Modeling of non-linear wave propagation over fringing reefs. Coast. Eng. 58, 1125–1137. https://doi.org/10.1016/j.coastaleng.2011.06.007

Shi, F., Kirby, J.T., Harris, J.C., Geiman, J.D., Grilli, S.T., 2012. A high-order adaptive time-stepping TVD solver for Boussinesq modeling of breaking waves and coastal inundation. Ocean Model. 43–44, 36–51. https://doi.org/10.1016/j.ocemod.2011.12.004

Shi, F., Kirby, J.T., Tehranirad, B., Harris, C.H., Choi, Y., Malej, M., 2016. FUNWAVE-TVD. Fully Non-linear Boussinesq Wave Model with TVD Solver. Documentation and User ’s Manual (Version 3.0). Research Report NO. CACR-11-03 CENTER, Center of Applied Coastal Research, University of Delware.

Stephenson, W.J., Kirk, R.M., 2000. Development of shore platforms on Kaikoura Peninsula , South Island , New Zealand Part One : The role of waves. Geomorphology 32, 21–41.

Su, S., Ma, G., Hsu, T., 2021. Numerical modeling of low-frequency waves on a reef island in the South China Sea during typhoon events. Coast. Eng. 169, 103979. https://doi.org/10.1016/j.coastaleng.2021.103979

Su, S. F., Ma, G., & Hsu, T. W., 2015. Boussinesq modeling of spatial variability of infragravity waves on fringing reefs. Ocean Engineering, 101, 78–92. https://doi.org/10.1016/j.oceaneng.2015.04.022

Sunamura, T., 1992. Geomorphology of Rock Coast. John Wiley & Sons, Chichester, 102, 139-183

Tamura, H., Kawaguchi, K., Fujiki, T., 2020. Phase-Coherent Amplification of Ocean Swells Over Submarine Canyons. J. Geophys. Res. Ocean. 125, 1–16. https://doi.org/10.1029/2019jc015301

Thomas, T.J., Dwarakish, G.S., 2015. Numerical Wave Modelling – A Review. Aquat. Procedia 4, 443–448. https://doi.org/10.1016/j.aqpro.2015.02.059

Thompson, C.F., Dickson, M.E., Young, A.P., 2022. Seismic signatures of individual wave impacts on a coastal cliff. Earth Surf. Process. Landforms 1–13. https://doi.org/10.1002/esp.5426

Thompson, C.F., Young, A.P., Dickson, M.E., 2019. Wave impacts on coastal cliffs: Do bigger waves drive greater ground motion? Earth Surf. Process. Landforms 44, 2849–2860. https://doi.org/10.1002/esp.4712

Thornton, E.B., Guza, R.T., 1983. Transformation of Wave Height Distribution. J. Geophys. Res. 88, 5925–5938.

Tonelli, M., Petti, M., 2009. Hybrid finite volume - finite difference scheme for 2DH improved Boussinesq equations. Coast. Eng. 56, 609–620. https://doi.org/10.1016/j.coastaleng.2009.01.001

Trenhaile, A.S., 2000. Modeling the development of wave-cut shore platforms. Mar. Geol. 166, 163–178.

Trenhaile, A.S., 1999. The width of shore platforms in Britain, Canada, and Japan. J. Coast. Res. 15, 355–364.

Trenhaile, A.S., 1987. The Geomorphology of Rock Coasts. Oxford University Press, Oxford, 25, 384.

Tsujimoto, H., 1987. Dynamic conditions for shore platform initiation, Science Report oftheInstituteofGeoscience.

Wei, Z., Dalrymple, R.A., 2017. SPH Modeling of Short-crested Waves, in: Coastal Engineering Proceedings.

Wei, G., Kirby, J.T., Sinha, A., 1999. Generation of waves in Boussinesq models using a source function method. Coast. Eng. 271–299.

Weiland, J., Wihelmsson, H., 1977. Coherent non-linear interaction of wave in plasmas, Pergamon, Oxford

Welch, P.D., 1967. The Use of Fast Fourier Transform for the Estimation of Power Spectra: A Method Based on Time Aver. aging Over Short, Modified Periodograms. IEEE Trans. Audio Electroacoust. AU-15, 70–73.

Winter, G.R.J., Lowe, G., Symonds, J.E.H., Van Dongeren, A.R., 2017. Standing infragravity waves over an alongshore irregular rocky bathymetry. J. Geophys. Res. Ocean. 122, 4868–4885. https://doi.org/10.1002/2016JC012264.Received

Yoon, S.B., Cho, Y.S., Lee, C., 2004. Effects of breaking-induced currents on refraction-diffraction of irregular waves over submerged shoal. Ocean Eng. 31, 633–652. https://doi.org/10.1016/j.oceaneng.2003.07.008

Young, T., 1802. On the Theory of Light and Colours. Philos. Trans. R. Soc. London 12–48.

Zhang, S. J., Zhu, L. S., Zou, K., 2019. A comparative study of numerical models for wave propagation and setup on steep coral reefs. China Ocean Eng., 33(4): 424–435, doi: 10.1007/s13344-019-0040-6

Appendix 1

Description of the fully nonlinear Boussinesq wave model FUNWAVE-TVD

The numerical phase resolving model FUNWAVE_TVD is based on the conservative form of the fully nonlinear Boussinesq equations formulated by Shi et al. (2012). Following Tonelli and Petti (2009) wave breaking forces the model to switch from Boussinesq equations, where dispersive and nonlinear effects are of a similar order of magnitude, to the nonlinear shallow water equation, where nonlinearity dominates. This model employs a Total Variation Diminishing (TVD) spatial discretisation scheme to solve the fully non-linear Boussinesq equation (combining finite-volume for nonlinear terms and finite-difference for dispersive terms) and incorporates a time-dependent reference level (Kennedy et al. 2001) moving with the instantaneous free surface to calculate the velocity potential. The combination of the shock-capturing TVD scheme and moving reference provides robust performance in simulating breaking waves and optimising nonlinear behaviour. Furthermore, the model uses an adaptative time stepping defined from a third-order Strong Stability-Preserving (SSP) Runge–Kutta scheme (Gottlieb et al., 2001) to increase model stability. The conservative form of the fully nonlinear Boussinesq equations in FUNWAVE_TVD employs a modification of the leading order pressure term in the momentum equation using a modified surface gradient term such as:

$$\eta_t + \nabla.\mathrm{M} = 0 \qquad \text{(A1.1)}$$

$$M_t + \nabla.\left[\frac{MM}{H_{tot}}\right] + \nabla\left[\frac{1}{2}g(\eta^2 + 2h\eta)\right] = H_{tot}\left\{\bar{u}_{2,t} + u_\alpha.\nabla\bar{u}_2 + \bar{u}_2.\nabla u_\alpha - V'_{1,t} - V''_1 - V_2 - V_3 - R\right\} + g\eta\nabla h \qquad \text{(A1.2)}$$

where ∇ denotes the horizontal partial derivative $((\partial/\partial x),(\partial/\partial y))$, η is the free surface elevation, h is the water depth, $H_{tot} = h + \eta$ is the total local water depth and g is the gravitational acceleration, the terms $\nabla\left[\frac{1}{2}g(\eta^2 + 2h\eta)\right]$ and $g\eta\nabla h$ are components of the surface gradient. The horizontal volume flux is expressed as:

$$M = H_{tot}\{u_\alpha + \bar{u}_2\} \qquad \text{(A1.3)}$$

where u_α is the horizontal velocity at the reference level $z_\alpha = \zeta h + \beta\eta$ (from Kennedy et al. (2001)) with ζ=-0.53 and β=0.47. While u_2 is the depth dependant correction at $O(\mu^2)$ (with μ representing the ratio of depth over wave length) that is expressed as:

$$u_2(z) = (z_\alpha - z)\nabla A + \frac{1}{2}(z_\alpha^2 - z^2)\nabla B \qquad \text{(A1.4)}$$

with $\nabla A = \nabla.(hu_\alpha)$ and $\nabla B = \nabla.u_\alpha$. The depth-averaged contribution to the horizontal velocity field is given by:

$$\bar{u}_2 = \frac{1}{H_{tot}}\int_{-h}^{\eta} u_2(z)dz = \left[\frac{z_\alpha^2}{2} - \frac{1}{6}(h^2| - h\eta + \eta^2)\right]\nabla B + \left[z_\alpha + \frac{1}{2}(h - \eta)\right]\nabla A \qquad \text{(A1.5)}$$

V_1 and V_2 represent the dispersive terms of the Boussinesq equation defined as:

$$V_1 = \left\{\frac{z_\alpha^2}{2}\nabla B + z_\alpha \nabla A\right\}_t - \nabla\left[\frac{\eta^2}{2}B_t + \eta A_t\right] \qquad \text{(A1.6)}$$

$$V_2 = \nabla\left\{(z_\alpha - \eta)(U_\alpha.\nabla)A + \frac{1}{2}(z_\alpha^2 - \eta^2)(\mathrm{U}_\alpha.\nabla)B + \frac{1}{2}[A + \eta B]^2\right\} \qquad \text{(A1.7)}$$

with V_3 representing the second order ($O(\mu^2)$) effect of the vertical velocity, which is expressed as:

$$V_3 = \omega_0 i^z \times \bar{u}_2 + \omega_2 i^z \times u_\alpha \qquad \text{(A1.8)}$$

Where with i^z the unit vector in the vertical direction and:

$$\omega_0 = (\nabla \times u_\alpha). i^z = v_{\alpha,x} - u_{\alpha,y} \tag{A1.9}$$

$$\omega_2 = (\nabla \times \bar{u}_2). i^z = z_{\alpha,x}(A_y + z_\alpha B_y) - z_{\alpha,y}(A_x + z_\alpha B_x) \tag{A1.10}$$

R in Eq. A3.2 represents the combination of diffusive (R_s) and dissipative (R_f) terms (Chen et al., 1999) induced by sub-grid lateral turbulent mixing and bottom friction, $R = R_s + R_f$, with R_f, expressed as:

$$R_f = \frac{C_d}{h + \eta} u_\alpha |u_\alpha| \tag{A1.11}$$

where C_d is the bottom friction coefficient.

Appendix 2

Description of the Bispectra Mode Decomposition

Advantages and limitations of orthogonal decomposition methods

Since its first application to fluid mechanics (Lumley, 1967), the Empirical Orthogonal Function (EOF) analysis has been used extensively to identify stationary patterns in random wavefields. However, the limitations of this approach are twofold. First, a single physical wave transformation process can be spread over more than one EOF mode; inversely, more than one physical process can contribute to one EOF mode. Additionally, the orthogonal nature of the EOF modes does not support the complex values necessary to define the physical properties of the wavefield from high-order spectral analysis. Therefore, the EOF analysis cannot establish causality between modal states and physical processes other than physical mechanisms previously accepted in the literature (e.g. standing waves) (Emery and Thomson, 2014).

Development and advantages of high-order spectral decomposition methods

Investigating the generation of stationary patterns from coherent wave amplification requires a decomposition method capable of holding information on both spectral and phase characteristics of the wavefield. Such information can be provided by high-order statistical analyses such as bispectrum, defined from the third moment of the data field (Hasselmann et al., 1963). The bispectrum presents attractive properties to identify coherent wave amplification. It is not only capable of detecting quadratic phase coupling for specific sets of frequencies but also represents a measure of skewness, which is expected to increase in areas of wave ray intersection (e.g. Janssen and Herbers, 2009). Despite these advantages, the bispectrum is only applicable to one-dimensional spatial domains. To overcome this limitation, Schmidt (2020) recently introduced the Bispectra Mode Decomposition (BMD), which consists of maximising the expansion coefficients of a spatial integral measure of the bispectrum. Thus, the BMD can be regarded as a decomposition method based on the same principle as the spectral EOF but applied to higher-order spectral analysis.

Description of the Bispectral Mode decomposition method

In the BMD approach, the time series of two-dimensional sea surface elevation observations defined in the time domain and cartesian coordinate system ($q(\xi, t) \in \mathbb{C}^{M \times N_t}$) are first redefined in the frequency domain using Welch's method (Welch, 1967) such as:

$$\hat{q}(\xi, f_k) = \sum_{j=0}^{N_{FFT}-1} q(\xi, t_{j+1}) e^{-i2\pi jk/} N_{FFT} \quad \text{with } k = 0, \ldots, N_{FFT} - 1 \tag{A2.1}$$

where $q(\xi, t_j) \in \mathbb{C}^M$ represents the two-dimensional sea surface observations in the spatial domain ξ defined by a number of points $M = N_x, N_y, N_z$ at a sample time t_j with j = 0, …, N_t. N_{FFT} represents the number of samples in one of the N_{blk} segments used to calculate the Fourier transform. Two-dimensional observations are, therefore, redefined in the space-frequency domain $\hat{q}(\xi, f_k) \in \mathbb{C}^{M \times N_{blk}}$.

The product of the Fourier coefficients used to define the bispectrum for frequencies k an l is obtained from the Hadamard product of the matrices $\hat{q}(\xi, f_k) \equiv \hat{q}_k$ and $\hat{q}(\xi, f_l) \equiv \hat{q}_l$ such as:

$$\hat{q}_{k \circ l} = \hat{q}_k \circ \hat{q}_l \tag{A2.2}$$

The spatial integral measure of the bispectrum is therefore expressed as:

$$b(f_k, f_l) = E\left[\int_\Omega \hat{q}_k^{\,*} \circ \hat{q}_l^{\,*} \circ \hat{q}_{k+l} \, d\xi\right] = E\left[\hat{q}_{k \circ l}^{\,H} \hat{q}_{k+l}\right] \tag{A2.3}$$

where $E[.]$ Is the expectation operator, $(.)^*$ and $(.)^H$ denote the complex conjugate and transpose, respectively. Assuming that the observed fluid is incompressible, the form of the triadic interaction in the Navier-Stokes is used in the BMD to establish a causal relationship between the product of the two interacting frequency components represented by the term $\hat{q}_{k \circ l}$ in Eq. A2.3, generating the third frequency component represented by the term $\hat{q}_{k+l}$. Therefore, the interacting and resulting frequency components are linked by a shared expansion coefficient, a_{ij}, in the modal decomposition and defined by the linear expansions:

$$\phi_{k\circ l}^{[i]}(\xi, f_k, f_l) = \sum_{j=1}^{N_{blk}} a_{ij}\,(f_{k+l})\hat{q}_{k\circ l}^{[j]} \quad \text{(A2.4)}$$

$$\phi_{k+l}^{[i]}(\xi, f_{k+l}) = \sum_{j=1}^{N_{blk}} a_{ij}\,(f_{k+l})\hat{q}_{k+l}^{[j]} \quad \text{(A2.5)}$$

The cross-frequency fields $\phi_{k\circ l}$ are maps of phase alignment between two frequency components, while bispectral modes ϕ_{k+l} are linear combinations of Fourier modes related to the amplitude of oscillations of the sea surface at frequency $k + l$. Consequently, the modal decomposition in the BMD is defined from the spectral properties of each segment obtained from the Welch method rather than from the raw two-dimensional time series of observations conventionally used in the EOF analysis. Eq. A2.4 and A2.4 can be, therefore, regarded as the product of expansion coefficients and data matrices such as:

$$\phi_{k\circ l}^{[i]} = \hat{Q}_{k\circ l}a_i \quad \text{(A2.6)}$$

$$\phi_{k+l}^{[i]} = \hat{Q}_{k+l}a_i \quad \text{(A2.7)}$$

Where $\hat{Q}_{k\circ l}$ and $\hat{Q}_{k+l} \in \mathbb{C}^{M\times N_{blk}}$ and $a_i = \left[a_{i1}(f_{k+l}), \dots, a_{iN_{blk}}(f_{k+l})\ \right]^T$represents the i-th vector of expansion coefficients for the (k, l) frequency doublets, with $(.)^T$ denoting the transpose. To optimally represent the sea surface characteristics in terms of integral bispectral density, the set of expansion coefficients a_1 maximising the value of $b(f_k, f_l)$ in Eq. A2.3 is defined from the numerical radius of the complex product matrix B representing the bispectral density matrix:

$$B = \hat{Q}_{k\circ l}{}^H\hat{Q}_{k+l} \quad \text{(A2.8)}$$

To seek the expansion coefficients corresponding to the largest eigenvalue λ_{max}. This method allows defining an optimal approximation of the eigenvalue characterising the integral bispectral density of the wavefield for each pair of frequency components, referred to as the mode bispectrum $\lambda_1(f_k, f_l)$. That is, the integral bispectral density is best represented by the first mode of the BMD, with other modes having a minimal impact. The peak magnitude of the optimal complex engine value $|\lambda_1(f_k, f_l)|$ for the set of frequencies f_k and f_l is analogue to the peak magnitude found in the bispectrum. Therefore, the BMD defines the modal states of the wavefield in regard to interactions between frequency components, which allows the extraction of spatial structures of phase coupling and resulting triadic interactions in two dimensions.